Theoretical and Experimental Analysis on Structural and Optical Properties of Some Benzimidazole Based Metal-Organic Complexes for Thermo-optical Applications

A Thesis submitted to Bharathidasan University
for the award of the degree of

DOCTOR OF PHILOSOPHY

in

PHYSICS

By

P. A. Praveen

[Reg. No.: 44317/Ph.D.K2/Physics /F.T. /Jan.2013/ dated 10.12.2012]

Research Supervisor

Dr. R. Ramesh Babu

DEPARTMENT OF PHYSICS
BHARATHIDASAN UNIVERSITY
TIRUCHIRAPPALLI-620 024
TAMILNADU, INDIA

JUNE 2018

Dr. R. Ramesh Babu

Assistant Professor

Department of Physics
Bharathidasan University
Tiruchirappalli - 620 024
Tamilnadu, India

Certificate

This is to certify that the thesis entitled **"Theoretical and Experimental Analysis on Structural and Optical Properties of Some Benzimidazole Based Metal-Organic Complexes for Thermo-optical Applications"** submitted to Bharathidasan University, Tiruchirappalli - 620 024 for the award of the degree of **DOCTOR OF PHILOSOPHY** in **PHYSICS**, is a bonafide record of the work originally carried out by **Mr. P. A. Praveen** under my supervision and guidance in the Crystal Growth and Thin Film Laboratory, Department of Physics, Bharathidasan University, Tiruchirappalli - 620 024 and has not been included in any other thesis submitted previously for the award of any degree.

(R. Ramesh Babu)

P. A. Praveen

Research Scholar

Department of Physics
Bharathidasan University
Tiruchirappalli - 620 024

June   , 2018

Declaration

I, **P. A. Praveen**, hereby declare that the work presented in this thesis entitled **"Theoretical and Experimental Analysis on Structural and Optical Properties of Some Benzimidazole Based Metal-Organic Complexes for Thermo-optical Applications"** has been independently carried out by me under the supervision of **Dr. R. Ramesh Babu**, Assistant Professor, Department of Physics, Bharathidasan University, Tiruchirappalli - 620 024. This thesis is composed of my original work and contains no material previously published or written by another person except where due reference has been made in the text.

(P. A. Praveen)

Acknowledgments

Creating a Ph. D. thesis is not an individual experience; rather it takes place in a social context and includes several persons, whom I am greatly indebted.

First of all, I owe a great dept of gratitude to my Mom for her full support and confidence on me. Even in the hardest situations, she supported me and encouraged me to do my higher studies. Without her I am nothing. Further, I wish to express my sincere thanks to my under graduate college teacher Dr. K. Ravichandran, who is the one, motivated and supported me to do Post Graduate as well as the Ph. D. Without his assistance, both mentally and financially, I can't be here. Eventhough, they don't expect a thanks, it my duty to express hearty thanks to my dear friends and brothers, Dr. D. Aravindhan, Dr. R. Jothimurugan, Dr. SP. Prabhakaran and Mr. T. Sriraman for their support over all possible ways. Especially, I must thank Jothimurugan and Aravinthan, for their association which strengthen me in personal, academics and administration.

I am privileged to express my enormous gratitude to Dr. R. Ramesh Babu, who has been here as my teacher as well as research supervisor for the past nine years since from my postgraduate thesis and has been unstinting in his support and constructive critique. I and my work have greatly benefited from his expert guidance and professional mentorship. Apart from academic, he is a kind hearted, care taker, reacted by understanding the practical situations and reality, has given me infinite freedom at all instances.

I express my sincere thanks to the my teachers, Prof. V. Parthasarathy, Prof. P. Kaliannan, Prof. M. Daniel, Prof. K. Ramamurthi, Prof. S. Dhanuskodi, Prof. S. Rajasekar, Prof. K. Thamilmaran, Dr. M. Senthilvelan, Dr. P. Muruganandam for their support and motivation. Further, I should add the support and help recieved from Head of the Department, Prof. K. Jeganathan and other departmental faculties Prof. S. Arumugam, Dr. T. C. Sabari Girisun and eminent Prof. M. Lakshmanan over the my course of study. I am grateful to all of them for inculcating the attitude of research on me.

I express my deep and sincere gratitude to my doctoral committee members Dr. M. Ashok, Department of Physics, National Institute of Technology, Tiruchirappalli and

PREFACE

Nonlinear optical (NLO) materials with larger hyperpolarizabilities have been investigated for applications in optical switching, signal processing, optical limiting, etc. In this regard, organic π conjugated materials have been widely investigated due to their better nonlinear optical susceptibilities than the inorganic NLO materials. In the recent past, benzimidazole (BMZ) - a heterocyclic aromatic compound, well known for its anti-microbial activities, gain much interest in materials science regime. Especially, it is identified as a potential second harmonic generating (SHG) material with 4 times better SHG efficiency than the standard potassium dihydrogen phosphate (KDP). But like many organic materials, BMZ also exhibit poor thermal and mechanical stabilities, and more optical scattering losses. To overcome these difficulties, incorporation of metal ion in the organic medium and synthesize them as metal organic complex is considered as the better alternative. So, the present work focuses on the incorporation of some first row transition metal ions with benzimidazole ligand and to investigate their structural and optical properties for thermo-optical applications.

In order to consider an organic material for NLO device fabrication, it should be tunable to accomodate different laser sources, robust to withstand prolonged/intense laser radiation and should have very less optical absorption and scattering losses. Previous works report that the incorporation of transition metal ions in BMZ medium enhances its optical, magnetic and antimicrobial activities. Further, depending upon their electronegativity, metal centers in the metal-organic system can create additional energy levels and electronic transitions, other than π-π transitions, which can enhance the nonlinear optical property of the materials. By fabricating these complexes

as thin films/ free standing films / nanoparticles offer additional advantages such as portability, compatibility with silicon photonics and planar waveguides and their low optical path lengths considerably reduces the optical scattering losses. So, the core objective of this investigation is to analyse the effect of incorporation of metal ions in the BMZ medium and to analyse the potentiality of the synthesized system towards NLO applications.

There are reports available on first row transition metals incorporated benzimidazole complexes, either as powders or as small crystals, for antibacterial and anticancer related applications. Few metals like Cd(II), Cu(II) and Co(II) complexes were investigated for solar cell, photoluminescence and magnetization related properties. Even though, all these reports indicates the contribution of charge transfer mechanism for the enhancement of properties, upto our knowledge barely no reports available on the nonlinear optical studies of metal-organic complexes of BMZ. So, the present study attempts to unravel the suitability of some first row transition metals based benzimidazole complexes towards nonlinear optical applications in a systematic manner.

There are two strategies, (i) Computational analaysis and (ii) Experimental evaluation, were primarily used to investigate the linear and nonlinear optical properties of BMZ and its metal complexes. Initially, semiempirical quantum chemistry progam MOPAC was used for the geometry optimization and molecular properties calculation. Parameters such as bond length, bond angle, dipole moment, energy gap, molecular energy and heat of formation were calculated and used for the interpretation of molecular polarizability and hyperpolarizability. From the computational analysis three potential candidates Co(II), Cu(II) and Mn(II) were opted for the experimental studies. These metal-BMZ complexes were either deposited as thin film or casted as free standing films depending upon the associated susbstituent in the metal ion. These samples were subjected to structrual and optical characterizations and evaluated for prototypes such as optical limiters and optical switches. Since, benzimidazole complexes have anticancer activity as well as good thermo-optical behaviour, they were also investigated for laser assisted anticancer activity. In particular, Cl substituted Co(II) and

Cu(II) - BMZ complexes were synthesized as nanoparticles by reprecipitation technique and phototoxicity effect was studied on human lung cancer (A549) and normal mouse embryonic fibroblast cell lines.

Based on the findings discussed above, the obtained results are compiled in the following format.

- **Chapter 1** briefly discusses the basics of nonlinear optics, its applications, materials for such applications, required improvements, brief literature survey on metal-organic complexes and objectives of the present work.

- **Chapter 2** provides the details about semiempirical simulation, their validation, obtained results on metal-BMZ complexes and their discussion.

- **Chapter 3** discusses the deposition/synthesis methods to fabricate the thin-films / free standing films / nanoparticles of benzimidazole metal complexes.

- **Chapter 4** provides details about the structural confirmation and surface properties of the fabricated samples.

- **Chapter 5** discusses the linear optical properties of the samples such as optical absorption, energy gap, dipole moment and dispersion properties.

- **Chapter 6** discusses the SHG efficiency and third order nonlinear optical properties of the samples.

- **Chapter 7** deals with the prototype demonstrations of the prepared samples as optical limiters, optical switch and the key element for photothermal theraphy and

- **Chapter 8** presents the summary of the thesis and the possible future directions.

List Of Publications

Articles:

1. **P. A. Praveen**, R. Ramesh Babu, P. Balaji, A. Murugadas, M.A. Akbarsha, *Laser Assisted Anticancer Activity of Benzimidazole Based Metal Organic Nanoparticles*, Journal of Photochemistry & Photobiology, B: Biology 180 (2018) pp. 218–224.

2. **P. A. Praveen**, R. Ramesh Babu, K. Ramamurthi, *Role of annealing on the structural and optical properties of nanostructured diaceto bis-benzimidazole Mn(II) complex thin films*, Spectrochimica Acta Part A: Molecular and Biomolecular Spectroscopy, 173 (2017) pp. 800–808.

3. **P. A. Praveen**, R. Ramesh Babu, K. Ramamurthi, *Theoretical and experimental investigations on linear and nonlinear optical response of metal complexes doped PMMA films*, Materials Research Express, 4 (2017) pp. 025024.

4. **P. A. Praveen**, R. Ramesh Babu, K. Jothivenkatachalam, K. Ramamurthi, *Spectral, morphological, linear and nonlinear optical properties of nanostructured benzimidazole metal complex thin films*, Spectrochimica Acta Part A: Molecular and Biomolecular Spectroscopy, 150 (2015) pp. 280–289.

5. **P. A. Praveen**, S. P. Prabhakaran, R. Ramesh Babu, K. Sethuraman, K. Ramamurthi, *Low power optical limiting studies on nanocrystalline benzimidazole thin films prepared by modified liquid phase growth technique*, Bulletin of Materials Science, 38(3) (2015) pp. 645–651.

Proceedings:

1. **P. A. Praveen**, R. Ramesh Babu, S. P. Prabhakaran, K. Ramamurthi, *Linear and nonlinear optical properties of Mn doped benzimidazole thin films*, AIP Conference Proceedings, 1591(1) (2014) pp. 991-993.

2. **P. A. Praveen**, R. Ramesh Babu, K. Ramamurthi, *Validation of PM6 and PM7 semiempirical methods on polarizability calculations*, AIP Conference Proceedings, 1665(1) (2015) pp. 609-618.

3. **P. A. Praveen**, R. Ramesh Babu, *Effect of substituents on polarizability and hyperpolarizability values of benzimidazole metal complexes*, AIP Conference Proceedings, 1731(1) (2016) pp. 090013.

4. **P. A. Praveen**, R. Ramesh Babu, *Theoretical and experimental evaluation of structural and optical properties of novel zinc-benzimidazole metal complex doped in polystyrene matrices*, AIP Conference Proceedings 1832 (2017) pp. 140038.

Book Chapters:

1. **P. A. Praveen**, R. Ramesh Babu *Semiempirical Modeling and Experimental Evaluation of Benzimidazole Based Metal-Organic Complexes for Nonlinear Optical Applications*, in Theoretical Materials Design: Optimization, Simulation and Experimental Realization, Springer (Accepted for Publication).

Table of Contents

List of Tables

List of Figures

Nomenclature

α Linear polarizability

β First-order hyperpolarizability

β_T Thermal expansion coefficient

γ Second-order hyperpolarizability

μ Molecular dipole moment

A549   Human lung cancer cell line

AFM   Atomic force microscopy

ALK   Anaplastic Lymphoma Kinase

ALP   Linear polarizability

ASP   As prepared

BA   Bond angle

BL   Bond length

BMZ   Benzimidazole

CA   Closed aperture

CIF   Crystallographic information file

Co-BMZ   dichloro bis benzimidazole Co(II)

Co-BMZ-NP   dichloro bis benzimidazole Co(II) nanoparticles

Co-BMZ-OAc   diaceto bis benzimidazole Co(II)

COSMO   Conductor like screening model

Cu-BMZ   dichloro bis benzimidazole Cu(II)

Cu-BMZ-NP   dichloro bis benzimidazole Cu(II) nanoparticles

Cu-BMZ-OAc   diaceto bis benzimidazole Cu(II)

CW   Continuous wave

d(H)   Hydrodynamic size

DFG   Difference frequency generation

DFT   Density Functional Theory

DLS   Dynamic light scattering

DMSO   Dimethyl sulfoxide

E   Molecular energy

EDX   Energy dispersive X-ray

EPR   Electron paramagnetic resonance

ESA   Excited state absorption

ETA   Global hardness

FOM   Figure of merit

FTIR   Fourier transform infrared

GMT   Goodgame type

GNORM   Gradient normalization

HOF   Heat of formation

HOMO   Highest occupied molecular orbital

INT   Intensity of vibrational frequency

ISC   Intersystem crossing

KDP   Pottasium dihydrogen phosphate

LPG   Liquid phase growth

LUMO   Lowest unoccupied molecular orbital

MBMZ   Benzimidazole Metal complex

Mn-BMZ   diaceto bis benzimidazole Mn(II)

NIH/3T3   Mouse embryonic fibroblast cell line

NLO   Nonlinear optics

OA   Open aperture

OL   Optical limiters

P-V   Peak to valley

PC   Principal component

PCA   Principal component analysis

PCA1 First principal component

PCA2 Second principal component

PDT   Photo dynamic theraphy

PM6   Parametrization method 6

PM7   Parametrization method 7

PMMA Poly(methyl methacrylate)

R_kU Kurtosis

R_q Root mean square roughness

R_sk Skewness

ROS   Reactive oxygen species

RPM   Revolutions per minute

RSA   Reverse saturable absorption

S_0 Ground state

S_1 First electronic excited state

SA   Saturable absorption

SCF   Self-consistent field

SFG   Sum frequency generation

SHG   Second harmonic generation

T_1 First triplet state

TDHF Time dependent Hartree Fock

TEM   Transmission electron microscopy

TOC   Thermo-optic coefficient

TPA   Two photon absorption

UFF   Universal force field

V-P   Valley to peak

XRD   X-ray diffraction

Z   Sample position

Introduction to Nonlinear Optical Materials

1.1   Introduction

The era of nonlinear optics (NLO) has began with the observation of second harmonic generation (SHG) in Quartz crystal using a ruby laser as the source by Franken et al in 1961 [1]. Thereafter much research was devoted to this field to develop both theory, to explain different nonlinear optical phenomena, and experiments to develop potential materials to utilize the observed nonlinear optical effects. Presently, NLO devices are expected to integrate as well as to compensate the current electronic devices to produce more advanced and sophisticated gadgets in the near future. Already, efforts were taken to develop photonic systems such as high-speed optical modulators, ultra-fast optical switches and high density optical data storage media using the nonlinear optical phenomena [2–5]. Development of potential applications requires better NLO materials, because, which decide the type of nonlinear effect, efficiency and the durability of the device. In the past, much research was devoted in the development of NLO single crystals. Since 1990, the study of nonlinear effects in microstructured ma-

terials has become a very active research domain [6]. Structuring the matter at the scale of the wavelength of the light enables the engineering of its dispersion properties such as phase and group velocity [3]. So, the fabrication of nanostructured thin films and particles offers a great opportunity to develop potential devices. While considering the experimental aspects, strong foundation on basic nonlinear optics and materials science is essential to observe, collect and interpret experimental data. So, the present chapter provides a brief discussion on the theory of nonlinear optics with a special emphasis on second and third order nonlinear optical effects. Followed by the brief survey on NLO materials and the potentiality of the benzimidazole and its metal complexes towards NLO applications.

1.2   Theory of Nonlinear Optics

Nonlinear optics is the area, that describes the change in molecular optical properties in the presence of an intense light field [7]. The light-matter interaction can be regarded as the scattering of photons by the electrons in the molecule. Each photon
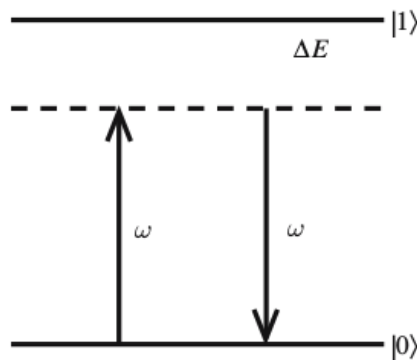
Fig. 1.1: Elastic scattering of incident photons of frequency ω

carries a linear momentum $p = E/c$ (where E is the Electric field and c is the velocity of light in vacuum), which is partially transferred to the molecule upon interaction. This process is known as elastic scattering and the scattered photons will have identical

frequency as that of the incident one. At the instant of interaction, the photon can be regarded as absorbed and the molecule as being in a virtual excited state (an intermediate energy state between the stationary states of the system). However, the time-scale τ for this interaction, or the lifetime of the virtual state, is short enough to not violate the time-energy uncertainty relation,

$$\tau \Delta E \sim \frac{\hbar}{2} \tag{1.1}$$

where ΔE denotes the energy difference between the nearest electronically excited state $|1\rangle$ and the virtual state. The de-excitation of the system from the virtual state back to the ground state $|0\rangle$ is associated with the emission of the scattered photon, a process referred as linear optics (see Fig. 1.1). In the case of high intensity of the incident radiation, the intensity enhances the probability for simultaneous multi-photon interactions in the molecule, i.e. two or more photons are annihilated and absorbed by the molecule in a single quantum mechanical process, known as nonlinear optics. In such cases, the frequency of the scattered photon need not to be equal to that of the absorbed photons. For example (see Fig. 1.2), if two quanta with frequency ω interacts with the molecule may be annihilated to create a third photon of frequency 2ω. This process is known as second-harmonic generation, which can be used to accomplish frequency conversion of light. Similarly, a large number of multi-photon interactions can be envisaged in the same manner. A high intense field, usually a laser, is required to observe nonlinear light matter interaction and this field can be approximated as a electro-magnetic plane wave in classical terms. The coupling between the two (light and matter) can be thus described as a classical electric-dipole coupling [8]. In the presence of an external electric field all charged particles in the molecule tends to oscillate and these oscillations give rise to an induced dipole moment. The degree to which the external field $E(t)$ manages to set the charges in motion is expressed
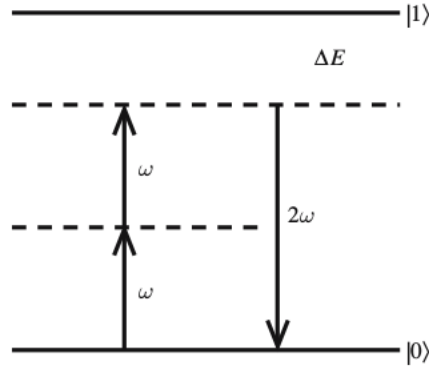
Fig. 1.2: Second-harmonic generation involving two incident photons of frequency ω and a sum frequency generated photon of frequency 2ω

in terms of the linear electric polarizability α. In general, the response of the charges depends on the frequency of the electric field, and the polarizability is therefore frequency dependent. So, the time-dependent polarization can be expressed as,

$$\mu(t) = \mu^0 + \alpha E(t) \tag{1.2}$$

where μ^0 is the permanent electric dipole moment of the molecule. A generalization of eqn. 1.2 which lets the polarization be expressed as a Taylor series in the electric field strength as

$$\mu(t) = \mu^0 + \alpha E(t) + \frac{1}{2}\beta E^2(t) + \frac{1}{6}\gamma E^3(t) + \dots \tag{1.3}$$

The electric field of an electromagnetic wave can be expressed as,

$$E(t) = E_0 \cos(\omega t) \tag{1.4}$$

Substituting eqn. 1.4 in eqn. 1.3 results,

$$\mu = \mu_0 + \alpha E_0 \cos(\omega t) + \frac{1}{2}\beta E_0^2 + \frac{1}{2}\beta E_0^2 \cos(2\omega t) + \frac{3}{4}\gamma E_0^3 \cos(\omega t) + \frac{1}{4}\gamma E_0^3 \cos(3\omega t) \tag{1.5}$$

This equation introduces the first-order hyperpolarizability (nonlinear polarizability) β, the second-order hyperpolarizability γ, and so forth. Just as the linear polarizability, the nonlinear coupling constants are also depends on the frequency of the applied field [9]. Table 1.1 lists some of the common nonlinear optical process with respect to applied field. Eqn. 1.4 provides the fundamental origin of nonlinearities at microscopic level and the expansion of coefficients in the equation provides the nonlinear optical performance of the material [10]. Hence, the theoretical modeling of nonlinear optical properties is concerned with the determination of these quantities for a given structure of the system.

Table 1.1: Common nonlinear optical process

Process	Frequencies
Second Order Process	
Static	$0; 0, 0$
Electro-optic Pockels effect	$-\omega; \omega, 0$
SHG	$-2\omega; \omega, \omega$
Third Order Process	
Static	$0; 0, 0, 0$
Electro-optic Kerr effect	$-\omega; \omega, 0, 0$
Intensity dependent refractive index	$-\omega; \omega, -\omega, \omega$
Electric field induced SHG	$-2\omega; \omega, -\omega, 0$
Third harmonic generation	$-3\omega; \omega, -\omega, \omega$

1.3   Applications of Nonlinear Optics

1.3.1   Second Order NLO Effects

Major applications of second order NLO effects can be broadly classified into three types: Pockels effect, sum frequency generation and parametric generation [11]. The Pockels or linear electro-optic effect is the modification of the refractive index of an optical medium when exposed to a static (or varying) electric field. The birefringence produced in the medium is directly proportional to the electric field. The applications

of the effect are the modulation of the amplitude, phase and path of a light beam, usually to enable it to carry binary information. Sum frequency generation (SFG) is a process in which two signals at frequencies ω_1 and ω_2 are summed to give a signal at frequency ω_3 ($\omega_1 + \omega_2 \rightarrow \omega_3$). The opposite effect also exists called difference frequency generation (DFG): the output signal at frequency ω_3 is the difference of the frequencies of the two input signals ($\omega_1 - \omega_2 \rightarrow \omega_3$, assuming ($\omega_1 > \omega_2$). A special case of sum frequency generation, and also the most common, is SHG: two input signals of the same frequency ($\omega_1 = \omega_2 = \omega$) result in an output signals of double the frequency ($\omega + \omega \rightarrow 2\omega$). SHG is easier to obtain than SFG, as for SFG the two input beams have to be phase matched, which is more difficult to realize experimentally. SHG has been mostly used for the conversion of infrared radiation into visible light or visible into ultraviolet light. The efficiency of this process is highly dependent on β (eqn. 1.5) and the frequency of the laser ω for given material. Finally, in Parametric generation (reverse phenomenon of SFG) a signal of frequency ω_1 is split into two signals of frequencies ω_2 and ω_3 ($\omega_1 \rightarrow \omega_2 + \omega_3$). This process is widely used for the generation of infrared laser beams from visible or near-infrared beams.

1.3.2   Third Order NLO Effects

The third order NLO effects are related to the cubic coefficient γ at given wavelength. γ is a complex number with real and imaginary parts as,

$$\gamma = \sqrt{\gamma_{real}^2 + \gamma_{img}^2} \tag{1.6}$$

The real part is responsible for the modifications of the refractive properties of the molecule while the modifications of the absorptive properties are related to the imaginary part [12]. The refractive part includes instantaneous electronic effects such as the quadratic electro-optic effect (Kerr effect) or frequency tripling and the imagi-

nary part is responsible for absorptive phenomena such as multi photon absorption, saturable absorption, etc. As these phenomena have different response times, time-resolved measurements have to be undertaken to determine which mechanisms are involved in the third-order NLO response of a given molecule or material. Many third order processes exist, some constituting valuable tools for nonlinear spectroscopy, while others have a greater technological importance. The frequency tripling of a light beam by the direct process of third harmonic generation is however not practically exploited, a cascade of two consecutive second order mixing process being preferred for the generation of short wavelength laser beams ($\omega + \omega \rightarrow 2\omega$ and $2\omega + \omega \rightarrow 3\omega$). One reason for this is that phase matching is virtually impossible to achieve for third harmonic generation [13]. Of greater technological importance are all-optical processes such as Kerr effect, two photon absorption and excited state absorption [14–17]. The Kerr effect is based on the same principle as that of Pockel effect and is its third order equivalent. In Kerr effect (or quadratic electro-optic effect), the modification of the refractive index of the medium varies as a function of the square of the applied electric field, instead of varying linearly with the electric field as in the Pockels effect. Two photon absorption (TPA) corresponds to the simultaneous absorption of two photons by a compound. In the degenerate case, the two photons absorbed are of the same energy, whereas in the non-degenerate case their energies are different. In principle, the direct process of two photon absorption is suitable for optical limiting. But in practice, the power limiting properties of the existing materials, even with the largest two-photon absorption coefficients, are still insufficient for the efficient protection of sensors from laser pulses. Saturable absorption (SA) and reverse saturable absorption (RSA), are similar to 2PA but corresponding to excited state absorption (ESA) of the system [18]. The difference between ESA and 2PA is temporal; i.e., the photons are absorbed one after another in SA and RSA, whereas it is simultaneous in 2PA. Due

to this stepwise nature, a real excited state of the molecule is involved from which the second photon is then absorbed and thus the process is called as ESA. If a substantial proportion of molecules are in this excited state, the transmission properties of the medium are no longer the same. The excited state has different absorptive properties from the ground state [19]. For RSA, a photo-darkening effect is observed. The transmission of the medium is decreased as the compound in this excited state has greater absorptivity than in the ground state at a given wavelength. In contrast, if the excited state has a lower absorptivity than the ground state, the transmission of the sample will be increased as ground state molecules are depleted and an absorption bleaching (SA) will be observed. In other words, if the absorption cross section of the medium in the excited state is lower than in the ground state, the transmission of the system increases once the medium is excited. It should be noted that when $\gamma_{img} > 0$, the compound acts as a two-photon absorber, whereas when $\gamma_{img} < 0$, the compound has SA properties. Like 2PA, materials with ESA has also find potential application in optical limiters.

1.4   Nonlinear Optical Materials

Suitable materials are required to achieve better nonlinear optical effects. A primary consideration in selecting materials for NLO applications is the nonlinear optical susceptibility to be adequately large. Some other requirements for a material to be considered for NLO applications are [20]:

   (i) The material should highly transmitting in/all the wavelength(s) of interest

  (ii) Should posses high resistant to laser damage

 (iii) Should have fast temporal response and

 (iv) Should be physically and chemically stable

In the case of second-order NLO materials a noncentrosymmetry structure is strictly required to translate the molecular hyperpolarizabilities (β) into material susceptibility $\chi^{(2)}$.

1.4.1   Second Order NLO Materials

It is well established that only crystals which lack of center of inversion symmetry can have a non vanishing second-order nonlinear optical susceptibility [21]. This requirement limits the choice of crystals fall within certain symmetry classes. An additional restriction to achieve second order nonlinear optical process with good efficiency is that the standard phase matching condition should be satisfied. Because of frequency dependence of the refractive indices (dispersion with respect to wavelength), birefringent materials can be used to satisfy the phase matching condition, by allowing the birefringence to compensate for dispersion. However not all the crystals with large second-order nonlinearities possess enough birefringence to be used and thus phase matching by means of birefringence imposes further restrictions on the choice of crystals to use for second-order NLO. Table 1.2 lists some of the classical second order NLO materials with the aforementioned properties. An alternative approach, known as quasiphase matching, entails periodically inverting the sense of the nonlinear coefficient in order to compensate the accumulated phase mismatch. Without phase matching the amplitude of the generated wave cannot experience large growth, but with quasiphase matching the generated wave experiences monotonic growth with an amplitude almost as large as that of the true phase matching. Materials like lithium niobate, potassium titanyl phosphate, rubidium titanyl arsenate, lithium tantalate, barium titanate and potassium niobate have been studied extensively in quasiphase matching [22–24]. Many asymmetric organic molecules have large values of the first order molecular hyperpolarizability β. Electron delocalization along

Table 1.2: Properties of some second-order NLO materials

Material	Transmission range (μm)	Nonlinear coefficient (pmV^{-1}) at 10.6 μm
Silver gallium selenide	0.78 - 18	d_{36}=33
β-barium borate	0.21 - 2.1	d_{22}=2.3, d_{24}=d_{15}=~0.1
Lithium iodate	0.31 - 5.0	d_{31}=-7.11, d_{33}=-7.02, d_{14}=0.31
Lithium niobate	0.21 - 2.1	d_{31}=-5.95, d_{33}=-34.4
Potassium dihydrogen phosphate	0.18 - 1.5	d_{36}=0.63
KTiOPO$_4$	0.35 - 4.5	d_{31}=6.5, d_{32}=5.0, d_{33}=13.7, d_{24}=6.6, d_{15}=6.1

with a conjugated backbone is shown in Fig. 1.3. In this example the nitrogen with the single bond donates an electron, and either of the triple-bonded nitrogen atoms at the other end of the molecule accepts an electron. The second order effects results from this electronic asymmetry. In the bulk noncrystalline organic materials, however, the active species are oriented randomly yielding no net effect over a length scale greater than molecular dimensions. To scale the large molecular nonlinear effect up to a useful level, some type of ordering is necessary. There are several methods in use to build up long ordered lengths. One is to use organic materials in crystalline form. Another method is to fabricate layered film structures through Langmuir-Blodgett or with some other techniques [25]. Here the single-molecule nonlinear layer alternates with a layer of spacer molecules so that the nonlinear molecules are all oriented in the same direction. Another and the most widespread technique involves in processing organic NLO materials is incorporating the NLO species into a polymer either directly or in close proximity followed by poling [26].
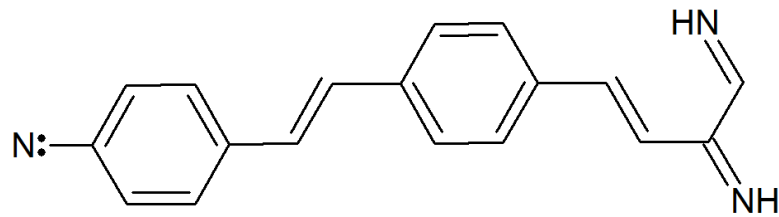
Fig. 1.3: Donor-acceptor organic molecule with conjugated bonds

1.4.2 Third Order NLO Materials

Materials with third order nonlinearities play a crucial role in NLO applications. Table 1.3 provides some important third order nonlinear optical materials and their nonlinear coefficients. Obviously, this list is by no means complete. The intension is to provide a survey of typical values of the third order susceptibility for a variety of materials. Materials such as insulating crystals and optical glasses typically possess nonlinear optical coefficients $\chi^{(3)}$ of the order of 10^{-13} to 10^{-14} esu [27]. Electronic polarization is believed to make the largest contribution to the nonlinear response of these materials. This process have a very fast response time of the order of 10^{-15} to 10^{-14} sec [28]. Semiconductors often possess a large third order susceptibility typically in the range of 10^{-13} to 10^{-10} esu. The susceptibility value of the semiconductors is usually strongly wavelength dependent, depending on the relative value of the photon energy of the incident light beam and the bandgap energy. For photon energies smaller than the bandgap energy, there is no fundamental difference between a semiconductor and an insulating solid [29]. Some of the largest optical nonlinearities have been reportedly measured in organic materials. Polydiacetylene and its derivatives can have nonresonant nonlinear optical susceptibilities $\chi^{(3)}$ of the order of 10^{-10} esu with femtosecond response times [30]. Delocalized π-electrons, which are free to travel along the conjugated structure or backbone of molecules and polymers, are the key factor to achieve high optical nonlinearities in organic materials. But the problem persists with the organic molecules are their low thermal and chemical stability. Generally, the molecules tend to decompose or disintegrate with continuous illumination of high power lasers. Many organic molecules posses melting point within 200 °C which limits the operation of materials with elevated temperatures, especially considering the materials for thermal assisted third order effect. One way to overcome this limitation is incorporating metal ions in the organic medium thus forms the metal

organic complexes [31–33]. Metal ions in the organic medium often improves the physical and chemical stability of the parent ligand. Further metal ions will produce additional electronic transitions which could further enhance the susceptibility of the nonlinear medium. Coordinated complexes such as phthalocynanine and porphyrin show promising optical nonlinearities [5] and further research is required to identify a potential material.

Table 1.3: Third order nonlinear optical coefficients of various materials

Material	$\chi^{(3)}$ esu	n_2 (cm^2W^{-1})
Crystals		
Al_2O_3	2.2×10^{-14}	2.9×10^{-16}
CdS	7.0×10^{-12}	5.1×10^{-14}
Diamond	1.8×10^{-13}	1.3×10^{-15}
GaAs	1.0×10^{-10}	3.3×10^{-13}
Ge	4.0×10^{-11}	9.9×10^{-14}
LiF	4.4×10^{-15}	9.0×10^{-17}
Si	2.0×10^{-10}	2.7×10^{-14}
TiO_2	1.5×10^{-12}	9.4×10^{-15}
ZnSe	4.4×10^{-12}	3.0×10^{-14}
Glasses		
Fused silica	1.8×10^{-14}	3.2×10^{-16}
AS_2S_3	2.9×10^{-11}	2.0×10^{-13}
Pb-Bi gallate	1.6×10^{-12}	1.3×10^{-14}
Nanoparticles		
CdSSe in glass	1.0×10^{-12}	1.8×10^{-14}
Au in glass	1.5×10^{-8}	2.6×10^{-10}
Polymers		
Polydiacetylene	6.0×10^{-10}	3×10^{-12}
Polythiophene	-4.0×10^{-8}	-2.0×10^{-10}
9-Butoxycarbonylmethylurethane	–	1.9×10^{-10}
4-Butoxycarbonylmethylurethane	-9.2×10^{-12}	-1.5×10^{-13}
Liquids		
Acetone	1.1×10^{-13}	2.4×10^{-15}
Benzene	6.8×10^{-14}	1.2×10^{-15}
Carbon disulfide	2.2×10^{-12}	3.2×10^{-14}
CCl_4	8.0×10^{-14}	1.5×10^{-15}
Di-iodomethane	1.1×10^{-12}	1.5×10^{-14}
Ethanol	3.6×10^{-14}	7.7×10^{-16}
Methanol	3.1×10^{-14}	6.9×10^{-16}
Nitrobenzene	4.1×10^{-12}	6.7×10^{-14}
Water	1.8×10^{-14}	4.1×10^{-16}

1.5   Benzimidazole for NLO Applications

Benzimidazole (BMZ) is a heterocyclic aromatic compound, well known for its antibacterial and antifungal activities [34]. It is a bicyclic compound formed by the fusion of benzene and imidazole. Figure 1.4 shows the structure of BMZ molecule and Table 1.4 provides the physical and chemical properties of BMZ. Historically, the first BMZ was prepared in 1872 by Hoebrecker by the reduction of 2-nitro-4-methylacetanilide [35]. Several years later Ladenburg obtained the same compound by refluxing 3,4- diamino-toluene with acetic acid [34]. It gained much attention by the discovery of 5,6-dimethyl benzimidazole moiety as a part of the chemical structure in vitamin B_{12} [36].
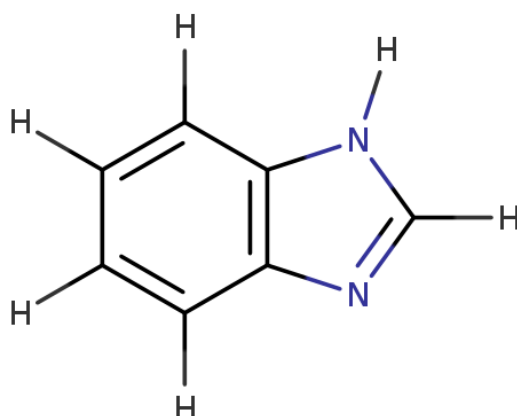
Fig. 1.4: Structure of BMZ molecule

Biologically BMZ is considered as a significant molecule with properties like anti-inflammatory, diuretic, antimicrobial, antiviral, antitumor, antiprotozoal, antiulcer and antioxidant [37–40]. Only in the recent past it is noticed that BMZ as a potential candidate in materials physics regime and in the past two decades enormous studies were reported for the applications such as optical, magnetic, solar cell and gas and dye sensing [41–44]. In particular BMZ has been identified as a potential SHG material with 4.5 times SHG efficiency of standard pottasium dihydrogen phosphate (KDP) crystal [45, 46]. Also several reports available on the coordination behaviour of BMZ with transition

Table 1.4: Physical and chemical properties of BMZ

Chemical formula	$C_7H_6N_2$
Molar Mass	118.14 g mol^{-1}
Acidity (pKa)	12.8 for BMZ and 5.6 for conjugated acid
Appearance	White powder or crystals
Stability	Stable, Combustible, Incompatible with strong oxidising agents
Toxicity	May irritate eyes, skin and respiratory tract
solubility	Insoluble in water. Soluble in alcohols
Melting point	170 to 172 °C
Boiling point	360 °C
Density	1.2 g/cm^3
Index of refraction	1.697
Molar refractivity	36.6 cm^3
Polarizability	14.5 10^{-24}
Surface tension	60.2 dyne/cm

metal ions evidently show the ability to tune its properties [47–49]. Previous works report the incorporation of metal ions in BMZ medium enhances its optical, magnetic and antimicrobial properties [50]. However, for nonlinear optical applications only a very few reports are available on benzimidazole and its derivatives. So systematic investigations are required to unravel the potentiality of BMZ and its metal complexes for second and third order related nonlinear optical applications.

1.6   Outline of Thesis

Based on the facts discussed above, we have performed our investigations on BMZ, in particular on BMZ metal coordination complexes to explore their linear and nonlinear optical properties. The findings are categorized and discussed in the following manner:

- **Computational analysis:** Semiempirical quantum chemical calculations were used to analyse the polarizability and hyperpolarizability of BMZ and its metal complexes. Further, the role of different metal ions and substituents were inves-

tigated towards the polarizabilty of the molecule. Based on the computational results, materials have been chosen for experimental analysis.

- **Materials processing:** The metal complexes were either synthesized as thin films or nanoparticles. Complexes with acetate substituents are highly insoluble in any of the commercial solvents, so they were embedded into polymeric matrices in order to fabricate them as free standing films.

- **Structural analysis:** Spectral analysis were performed to confirm the synthesized of compounds with computational aid. In some cases electron paramagnetic resonance (EPR) and energy dispersive X-ray (EDX) analyses are also used for structural confirmation.

- **Surface properties:** The prepared samples were annealed upto 200 °C and the effect of annealing on the surface morphology of the annealed samples were analysed using atomic force microscopy (AFM) and micro-Raman analysis.

- **Linear optical properties:** The linear optical properties were studied using transmittance spectrum in UV-Vis-IR region. From which, the different optical properties such as linear refractive index, optical dielectric constant and the dispersion parameters were calculated.

- **Nonlinear optical properties:** The SHG efficiency of the samples were studied using Nd:YAG laser of wavelength 1064 nm. The third order nonlinear optical properties were measured using a CW laser of wavelength 650 nm.

- **Applications:** Most of the samples were demonstrated with optical limiting ability. Manganese incorporated thin films show optical switching property. Whereas, cobalt and copper based BMZ nanoparticles were demonstrated to have thermo-optic assisted anticancer activities.

1.7 Conclusion

From the brief review on theory of nonlinear optics and the materials for second and third order nonlinear optics one can derive the following conclusions: (i) Organic materials posses better nonlinear optical susceptibilities than that of their inorganic counterparts (ii) This limits only by the physical and chemical stability of the organic materials (iii) Further, combined investigations on materials design, synthesize and characterization are required to develop a potential material for the nonlinear optical applications. In this scenario, metal organic materials are new class of materials, possess both the advantage of organic and inorganic materials. So, systematic analysis on the design and characterization of these kind of materials may yield fruitful results. In this direction, the thesis discusses the computational design, synthesis/ thin film deposition and characterization of benzimidazole and its metal complex thin films for nonlinear optical applications.

2

Computational Analysis

2.1   Introduction

Quantum mechanical calculations provide a conceptual way to solve the electronic structures of atoms as well as complex molecules. Many computational methods with different accuracies, like ab initio methods, DFT, semiempirical methods and molecular dynamics formulations are available to solve those equations. Among them semiempirical methods are simple and powerful tool to explore the electronic structures with the acceptable accuracy level and it increases the computational efficiency by several times than the ab initio methods. However, approximations and parametrizations of semiempirical methods limit their accuracy. Modern semiempirical methods such as PM6 and PM7 can be used to find out electronic structure of all the elements in the periodic table and they provide exact substitution of empirical parameters for calculations [51]. So, in the recent past, calculations based on PM6 and PM7 are constantly employed to model the linear and nonlinear optical properties of molecular as well as solid state systems [52, 53]. This chapter discusses the polarizability calculations

based on PM6 method to investigate the potentiality of metal complexes over the parent benzimidazole (BMZ) ligand. Further, the variation in polarizability and hyper-polarizability calculations is analysed by substituting the different first row transition metal ions with the BMZ ligand. The benzimidazole metal complexes are usually synthesized with substituents like halides and acetates and their role on the optical polarizability is discussed in this chapter. The chapter has been broadly classified into four sections. Section 2.2 describes the methodology we adopted for polarizability calculations, section 2.3 describes the polarizability calculations of first row metal ions with benzimidazole ligands, section 2.4 portraits the role of different substituents in polarizability and hyperpolarizability of benzimidazole metal complexes and finally section 2.5 elaborates the principal component analysis (PCA) to correlate the obtained results.

2.2 Methodology

There are many reports available on benzimidazole transition metal complexes including mono-, bi-, and tri-dentate benzimidazoles. Some consist of 2-substituted benzimidazole and others consist of benzimidazole based mixed ligands [48, 54]. Complexes with the very simple stoichiometry (M-BMZ$_2$-X$_2$) (M is a transition metal and X is Cl, Br or I) have been widely studied and a number of coordination compounds with manganese (II), cobalt (II), nickel (II), copper (II), zinc (II), cadmium (II), mercury (II), chromium (II) and cobalt (III) are reported earlier [55, 56]. These polyfunctional molecules bear nitrogen atom as the basic site for coordination with metal ion. Two strategies have been used to analyse the role of metal ions and substituent effects. Firstly, the role of different metal ions has been analysed by substituting the different first row transition metals in a Goodgame and Cotton type coordination complex [57], with the molecular formula M-BMZ$_2$. Then, the role of substituents has been

analysed by keeping a transition metal ion unaltered and different substituents were substituted in the molecular structure. In BMZ, bonding occurs through the nitrogen atom in a monodentate form, regardless of the metal ion or the heteroatom (N, S, O) present in the molecule, or in a bidentate mode, giving place to a variety of metal-ligand coordination modes [58, 59]. In the present work, our intention is to synthesize M-BMZ$_2$-X$_2$ type coordination complexes and to study their linear and nonlinear optical properties. For semiempirical analysis, PM6 Hamiltonian is used for all the calculations. To verify the accuracy of PM6 and PM7 methods, benchmarking calculations were performed and given in **Appendix-A**. Calculation process is shown in a flowchart in Fig. 2.1. Molecular input files are derived either from the Crystallographic Information Files (.CIF) or drawn using ChemDraw package. The drawn molecules were pre-optimized using universal force field (UFF) algorithm embedded in Avogadro package. Then, they were converted into MOPAC input files (.mop) by using the same package. For geometry optimization, Gradient Normalization (GNORM) value has been chosen as 0.25 for all the molecules. The optimized molecules were subjected to vibrational analysis (FORCE calculation) to identify the presence of any negative frequencies. If negative frequencies are obtained, the molecular input values were changed and it was re-optimized until a global minimum was obtained. The generated auxiliary (.aux) files during the geometry optimization was used to calculate the HOMO, LUMO and energy gap (E$_g$) values. The polarizability, first and second order hyperpolarizability of the molecules were calculated using the optimized geometries at time-dependent Hartree Fock (TDHF) level. Even though, TDHF method is considered as a reliable method in predicting the nonlinear optical properties of molecules, it may not exactly reproduce the experimental results. Since our intention is to understand the role of metal ions and substituent dependent changes in linear and nonlinear optical properties of the benzimidazole metal complexes, this level of theory is adopted as

enough to derive the structure dependent properties. Polarizability and hyperpolariz-
ability calculations were carried out using the POLAR option in the MOPAC package.
Further, the highest occupied molecular orbital (HOMO), lowest unoccupied molecu-
lar orbital (LUMO) were calculated and they were used to estimate energy gap (E_g) of
the molecules. GABEDIT and Molden programs were used to visualize the geometries,
plot the frontier orbitals and to calculate the energy gap [60, 61].
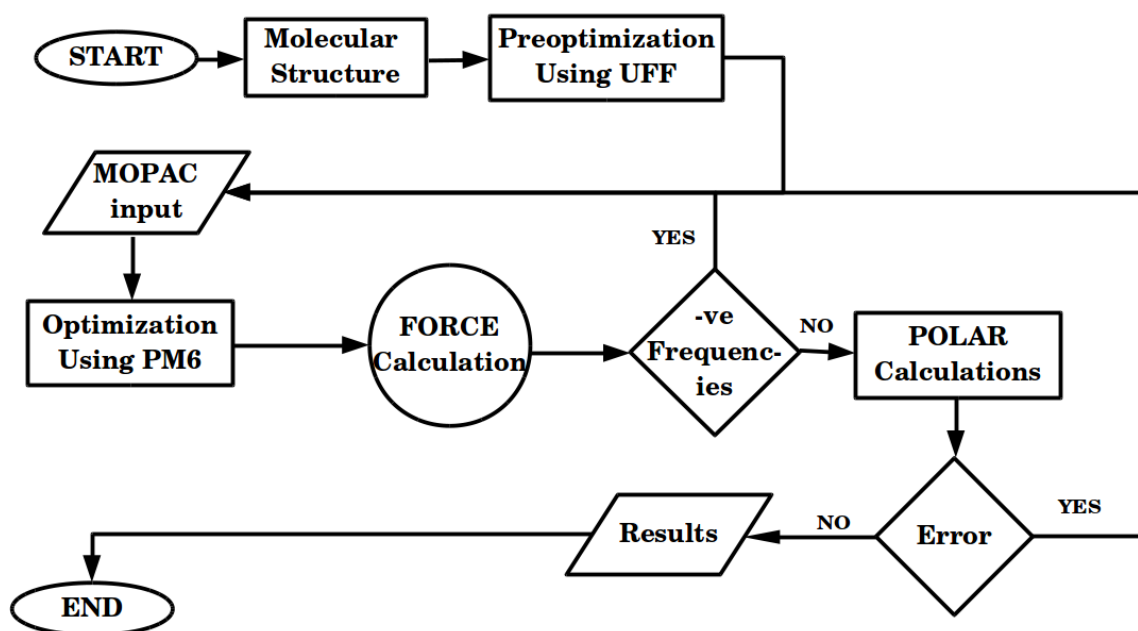
Fig. 2.1: Flowchart of geometry optimization process

2.3   Role of Metal Ions

Goodgame and Cotton type [57] structures are the simplest possible BMZ coordina-
tion complexes and their molecular structure is shown in Fig. 2.2 (a). Figure 2.2 (b)
shows the same structure with substituents. The calculated band gap (E_g) values of
all the complexes with and without substituents are given in Fig. 2.3. Ti and Ni com-
plexes shows highest band gap values about 0.32 eV, followed by V, Fe, Sc and Cr. Co,
Mn and Cu complexes are the one with lowest band gap values about 0.21 eV. This

can be interpreted that the Co, Mn and Cu complexes can be easily polarizable with an applied external frequency, than the other first row transition metal ions. Fig. 2.4 shows the heat of formation (HOF) of all the Goodgame and Cotton type molecular structures, lower the HOF values more stable the structure. It can be seen that Ti and Fe complexes required highest energy to form the complex while the HOF values of Cu, Co and Mn (Cu>Co>Mn) suggests the ease of synthesis and stability of the structures.

A = First row transition metals
X = Substituents
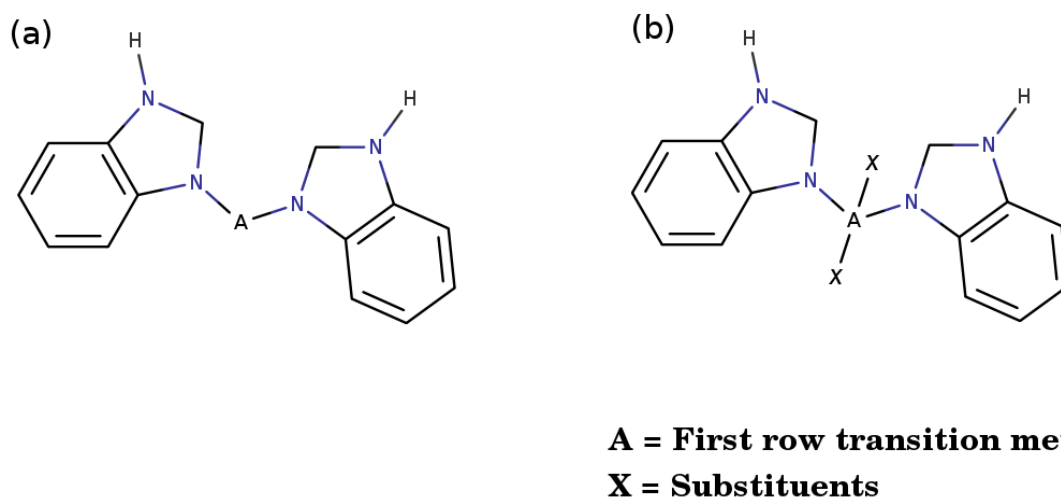
Fig. 2.2: Goodgame and Cotton type BMZ metal complexes (a) without substituents and (b) with substituents

Calculated α values and their variation with respect to the applied frequency are depicted in Fig 2.5. Complexes with (Ti and Ni) high E_g values show the lowest polarizability values. It is obvious that higher the band gap value, it is harder to perturb the system with an external frequency and vice versa. Due to this Co, Cr and Cu metal complexes shows higher polarizability values, suggesting the softness of its electronic cloud towards external perturbations like electromagnetic radiation. The polarizability values of all the molecules directly proportional to the strength of the applied field (Fig. 2.6). Since all the molecules considered in the present study are noncentrosymmetric, it is expected that all should exhibit a non-zero first order hyperpolarizability

21
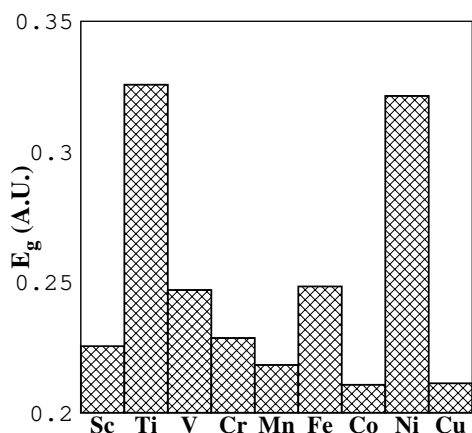
Fig. 2.3: Calculated band gap values of Goodgame and Cotton type BMZ metal complexes
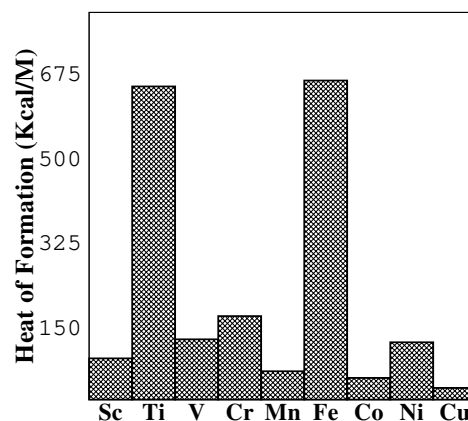
Fig. 2.4: Calculated HOF values of Goodgame and Cotton type BMZ metal complexes
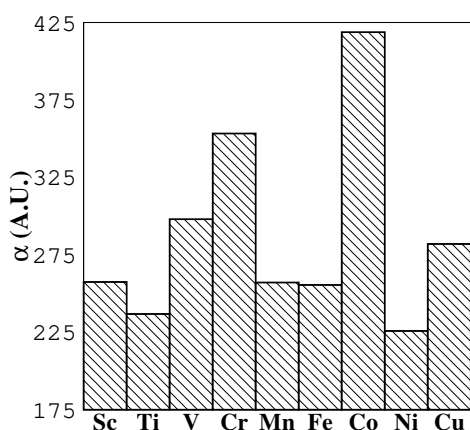
Fig. 2.5: Calculated α values of Goodgame and Cotton type BMZ metal complexes
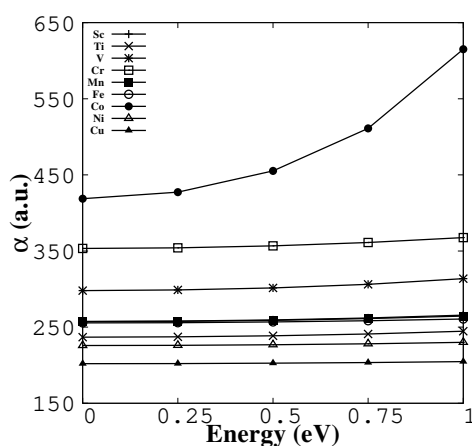
Fig. 2.6: Variation in α values with respect to applied frequency

(β) values. The obtained values are plotted and shown in Fig. 2.7. The variation in first order hyperpolarizability value is due to the free electron distribution in the molecules and which in turn directly proportional the filled level of d-shells [62]. This can be evident from the high β values of V, Cr and Mn metal complexes. For different applied frequencies, the first order hyperpolarizability values increase similar to the α values (Fig. 2.8).

The second order hyperpolarizability (γ) shows monotonic increase with increasing field strength as shown in Fig. 2.9. The behaviour of the molecules resembles the

polarizability variations except the case of Cr of metal complexes. Although Cr complexes show significantly higher E_g values, due to the unfilled d-shell it shows higher γ values. The variation in γ values with respect to applied frequency is shown in Fig. 2.10.
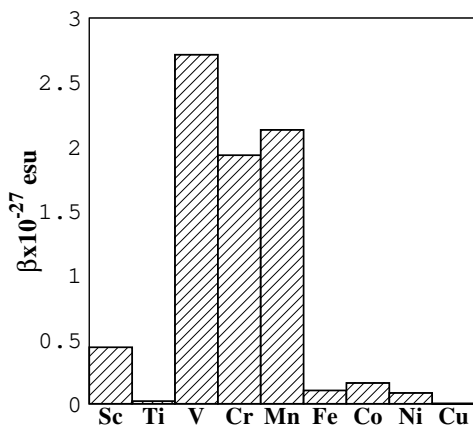
Fig. 2.7: Calculated β values of Goodgame and Cotton type BMZ metal complexes
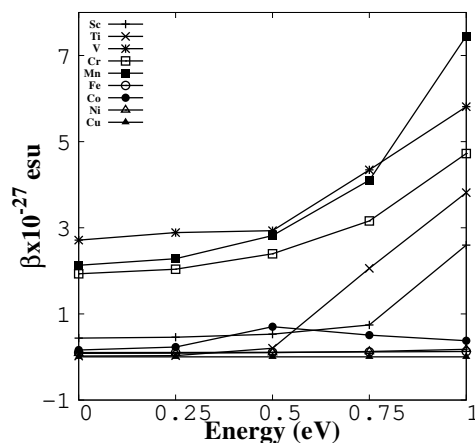
Fig. 2.8: Variation in β values with respect to applied frequency
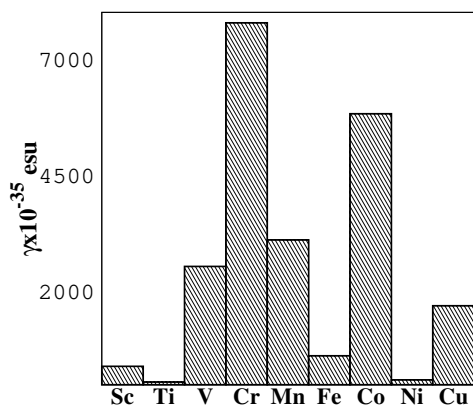
Fig. 2.9: Calculated γ values of Goodgame and Cotton type BMZ metal complexes
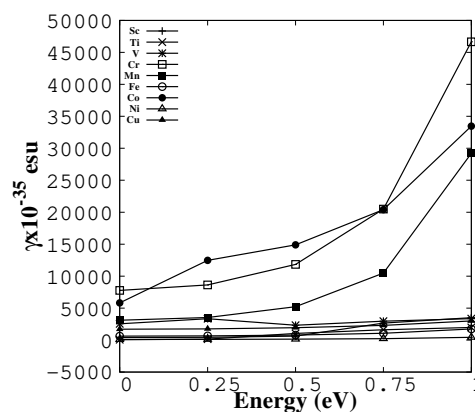
Fig. 2.10: Variation in γ values with respect to applied frequency

2.4   Principal Component Analysis (PCA)

Even though, we can derive conclusion about the nonlinear optical properties of benzimidazole metal complexes from HOF and polarizability analysis, the structure-property relationship is more complex. It depends on variety of molecular parameters such as bond length, bond angle, energy gap, global hardness, molecular energy, heat of formation, dipole moment, intensity of vibrational frequency etc. These all are interrelated and contribute to the overall susceptibility values by different manner. In order to explore that we have used principal component analysis, a stastical method, to evaluate the role of different molecular parameters on different molecular structures. For the study, two structures of bis benzimidazole with and without substituents have been considered. The extracted molecular parameters from the semiempirical calculations are analysed by PCA and the obtained first and second principal components from PCA is then linearly correlated to the hyperpolarizabilty values of different molecular structures.

2.4.1   Optimized geometry

Table 2.1 shows the optimized geometrical parameters of metalated BMZ (MBMZ) complexes with and without chloride ion substituents (Goodgame Type - GMT). Considering dihedral angles, without Cl substituent, the angles increases from 134.3 °to 179.2 °, i.e., molecules show an increment trend from Ti to Mn. Whereas, for Fe, it decreases to 156.9°, then increases for Co. But once again it decreases for Ni and then increases for Cu. In case of Cl substituted complexes a down trend is observed for V and Cr, Co and Ni. This variation can be interpreted as due to the variation of electronic distribution caused by the incorporation of metal ions and the substitution of Cl ions. Further, the results indicates that the planarity of the molecules decreases with increase in the atomic number of the metal ions. Considering bond lengths, it

24

decreases with increase in the atomic number of metal ions. But it shows an incre-
ment trend for Co and Ni complexes and decreases slightly from the trend for Cu
complexes. On the other hand, Cl substituted complexes show decrement upto Cr
and then increases for Mn and Co complexes. The variation in the bond lengths can
be attributed to the conjugation effect, which tends to produce a maximum overlap
of lone pairs with the p_z orbitals [63, 64].

Table 2.1: Calculated bond lengths (Nitrogen (N) - Metal (M)) and bond angles (N-M-N) of first row
transition metals incorporated and Cl substituted MBMZ complexes

Molecule	(N-M) (Å)		(N-M-N)(°)	
	GMT	Cl-MBMZ	GMT	Cl-MBMZ
Ti-BMZ	2.03	2.05	134.3	106.9
V-BMZ	1.92	1.90	138.0	104.0
Cr-BMZ	1.89	1.80	157.3	95.5
Mn-BMZ	1.79	1.83	179.2	149.3
Fe-BMZ	1.72	1.82	156.9	153.9
Co-BMZ	1.75	1.88	179.1	151.0
Ni-BMZ	1.89	1.83	177.0	112.8
Cu-BMZ	1.76	1.82	179.4	177.2

2.4.2   Electronic properties

Figure 2.11 shows the calculated HOMO and LUMO orbitals of benzimidazole metal
complexes with and without susbtituents. In the case of complexes without susbtituents,
the HOMO is distributed over one ring in Figure 2.11((i)-h), whereas in Figure 2.11((i)-
d) it is located at the spot of metal ion. In other compounds, distribution over one
ring trend is observed with more distribution range. In Figure 2.11((ii)- (a) to (e) is also
shows the similar phenomenon discussed above. In the case of Figure 2.11((ii)-f) and
((ii)-g), HOMO is distributed over the entire molecule. Considering LUMO, one ring
distribution is observed for Figure 2.11(i)-(a) to (e) and other complexes such as in Fig-
ures 2.11(i)-(f) to (h) shows the complete LUMO distribution over the molecule. This
indicates that the active sites are often distributed to the one of the imidazolate ring

and charge transfer between the molecule taken place through the metal ion. A similar phenomena is observed in the case of Cl substituted MBMZ complexes too.
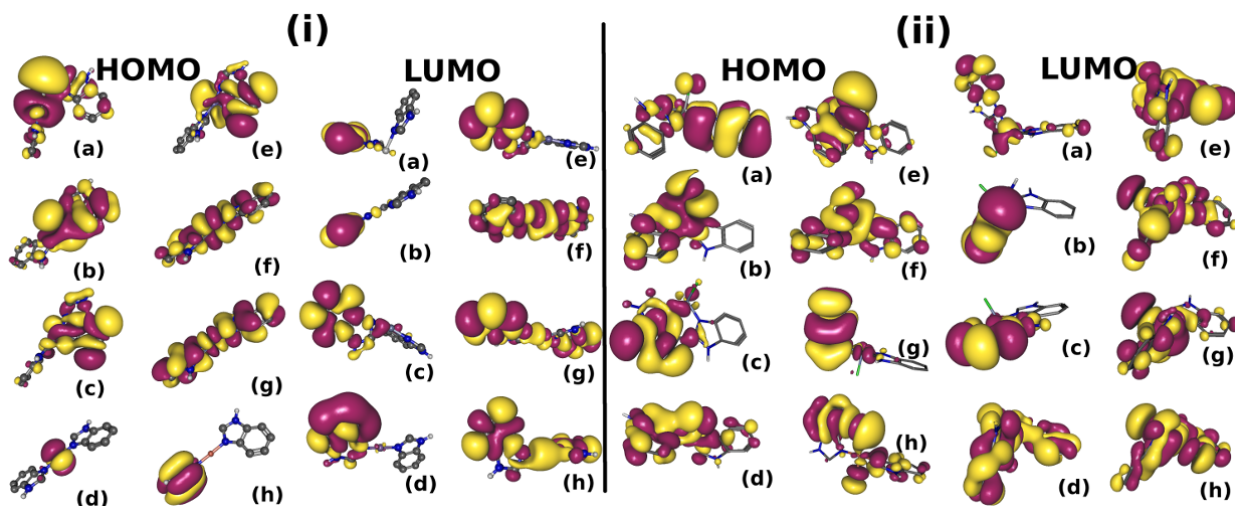
Fig. 2.11: HOMO and LUMO orbitals of benzimidazole metal complexes (i) without and (ii) with Cl substituents: (a) Ti-BMZ (b) V-BMZ (c) Cr-BMZ (d) Mn-BMZ (e) Fe-BMZ (f) Co-BMZ (g) Ni-BMZ (h) Cu-BMZ

Further, from HOMO, LUMO and energy gap (E_g=LUMO-HOMO) the global hardness factor η was calculated using the relation $\eta = E_g/2$ [65]. This factor can be taken as a estimation of chemical hardness of a molecule and can be used to describe the reactive behaviour of the molecular system. From Table 2.2, the energy gap values of the metal complexes without substituents show decreasing trend in the case of Cr and Co molecules and, Co complexes show the lowest energy gap value of this series. In the case of Cl substituted complexes, V, Cr, Fe and Co show the decrement trend and Co complex shows the lowest energy gap value. The reactivity (η) order of benzimidazole metal complexes without substituents can be given as $Mn < Cr < Ni < V < Ti < Cu < Fe < Co$ and for the complexes with substituents it can be given as $Co < Cr < V < Ni < Cu < Fe < Mn < Ti$. It can be seen that the reactivity values decrease for the Cl substituted metal complexes, indicates that these complexes are more stabilized than the complexes without substitution.

Table 2.2: Calculated HOMO, LUMO, Band gap (E_g) and global hardness (η) of first row transition metals incorporated and Cl substituted MBMZ complexes

Molecule	HOMO (eV)		LUMO (eV)		E_g (eV)		η (eV)	
	GMT	Cl-MBMZ	GMT	Cl-MBMZ	GMT	Cl-MBMZ	GMT	Cl-MBMZ
Ti-BMZ	-0.2942	-0.3619	-0.0887	-0.0791	0.2055	0.2828	0.1914	0.1414
V-BMZ	-0.3048	-0.2863	-0.0688	-0.0588	0.2336	0.2275	0.1868	0.1137
Cr-BMZ	-0.2839	-0.3074	-0.0837	-0.0847	0.2002	0.2227	0.1838	0.1113
Mn-BMZ	-0.2817	-0.3173	-0.0767	-0.0508	0.2054	0.2665	0.1792	0.1332
Fe-BMZ	-0.3134	-0.3128	-0.0944	-0.0636	0.2197	0.2492	0.2039	0.1246
Co-BMZ	-0.2953	-0.2416	-0.1373	-0.1285	0.1581	0.1131	0.2163	0.0565
Ni-BMZ	-0.3161	-0.3388	-0.0564	-0.1032	0.2597	0.2356	0.1862	0.1178
Cu-BMZ	-0.3500	-0.3398	-0.0400	-0.0976	0.3142	0.2422	0.1950	0.1211

2.4.3   N-M stretching intensities

Stretching intensity of the imidazole nitrogen and metal ion (N-M) was calculated for MBMZ molecules, with and without substituents, from the vibrational analysis and is given in Table 2.3. It can be seen that there is a variation in ν upto 50 cm^{-1} in both the cases depending on the type of metal ion and substituent. Further, there is a sharp variation in intensities ranging from 1000 to 12000 (Km/mol). Strong infrared intensities in the case of Ti, V and Co can be attributed to the back-donation of electrons from N1 of the imidazolate ring. But the saturation of d-levels in metal ions greatly affects the back-donation, and in the case of Cl substituents sharing of electron density play a significant role in the vibrational intensities. Drastic shift observed in the case of Cr and Ni without susbtituents and V, Mn and Co with substituents can be attributed to the Fermi resonance due to the deformation of imidazolate ring [66, 67]. But a high unharmonic coupling due to the molecular deformation is necessary to explain such a drastic variation in frequency. Further studies are required to confirm the same.

Table 2.3: N-M stretching intensities of first row transition metals incorporated and Cl substituted MBMZ complexes

Molecule	GMT		Cl-MBMZ	
	ν (cm^{-1})	Intensity (Km/mol)	ν (cm^{-1})	Intensity (Km/mol)
Ti-BMZ	399	11871	397	11947
V-BMZ	398	11492	357	16036
Cr-BMZ	354	2906	405	1872
Mn-BMZ	406	1286	334	9160
Fe-BMZ	390	1148	417	2601
Co-BMZ	375	8136	358	7847
Ni-BMZ	429	5089	424	3298
Cu-BMZ	384	3844	400	1544

2.4.4 Energy and point group

Table 2.4 shows molecular energy (E), heat of formation (HOF), molecular dipole moment (μ) and point groups of benzimidazole metal complexes with and without susbtituents. Excluding Co complex (in both the cases), for all other complexes, the molecular energy increases with increase in atomic number. Degenerated d-shells could be the reason for such a variation in the case of Co complex. HOF values of the complexes without susbtituent shows an increment trend with respect to atomic numbers for the case of Ti, V and Cr, but decreases for Mn, Fe and Co complexes. Further increment in atomic number increases the HOF value. In the case of Cl substituted complexes decrement is observed for Cr complex alone and for all other MBMZ complexes an increment trend has been observed. Further analysis is required to explain this phenomena. The point groups are generated based on the molecular deformation due to metal ions and susbtituents. But from our results, it can be seen that there is no strict connection between the molecular point group and molecular energy/HOF values.

Table 2.4: Calculated molecular energy (E), heat of formation (HOF), molecular dipole moment (μ) and point groups of first row transition metals incorporated and Cl substituted MBMZ complexes

Molecule	E (eV)		HOF (kcal/mol)		μ (debye)		Point group	
	GMT	Cl-MBMZ	GMT	Cl-MBMZ	GMT	Cl-MBMZ	GMT	Cl-MBMZ
Ti-BMZ	-2509	-3022	495.15	394.56	3.95	3.48	C_1	C_1
V-BMZ	-2546	-3057	526.58	454.04	3.57	3.42	C_1	C_1
Cr-BMZ	-2627	-3143	586.13	414.60	7.30	7.59	C_1	C_s
Mn-BMZ	-2638	-3149	545.09	471.81	0.39	3.49	C_2	C_1
Fe-BMZ	-2870	-3381	534.87	475.60	6.41	1.87	C_1	C_1
Co-BMZ	-2612	-3121	529.66	509.92	1.31	5.93	C_2h	C_1
Ni-BMZ	-2927	-3437	568.83	544.27	0.20	4.91	C_2	C_1
Cu-BMZ	-3097	-3607	592.87	547.60	0.94	5.10	C_1	C_1

2.4.5   Polarizability and Hyperpolarizability

Table 2.5 shows the calculated static polarizability and hyperpolarizability values of MBMZ complexes, with and without susbtituents. Considering linear polarizabilty, molecules without substituents have the values between 2 and 8.72 ($\times 10^2$) atomic units, Cr complex shows the highest polarizability. Cl substitution have a positive contribution on linear polarizabilty and it increases to many folds in the case of V, Cr and Fe. Complexes without substituents shows β values between 1.36 and 8.74 ($\times 10^3$ a.u.) and V and Co have the higher values about 8.74 $\times 10^3$ a.u. In the β calculations too, Cl susbtituents improves the first order hyperpolarizabilty values by many times and Co and Ni shows β values higher than 100 $\times 10^3$ a.u. The γ values of benzimidazole metal complexes are between 1.17 and 8.18 $\times 10^5$ a.u. and Cr and Fe shows the high γ values. Again substituents have a positive impact on the second order hyperpolarizabilty and V complexes shows the highest γ value.

2.5   Correlation between molecular descriptors

From the results discussed above, it is not possible to derive a conclusion on the effect of different parameters on nonlinear optical properties. When the dimension of

Table 2.5: Calculated static polarizability and hyperpolarizability values of first row transition metals incorporated and Cl substituted MBMZ complexes

	$\alpha \times (10^2)$ (a.u.)		$\beta \times (10^3)$ (a.u.)		$\gamma \times (10^5)$ (a.u.)	
Molecule	GMT	Cl-MBMZ	GMT	Cl-MBMZ	GMT	Cl-MBMZ
Ti-BMZ	2.09	18.45	2.51	30.14	6.37	11.28
V-BMZ	3.96	60.94	8.74	57.83	4.09	74.57
Cr-BMZ	8.72	29.05	1.36	2.60	8.08	5.72
Mn-BMZ	2.00	8.57	1.46	13.42	5.39	97.47
Fe-BMZ	3.40	27.45	6.23	65.21	8.18	78.18
Co-BMZ	2.83	3.66	8.30	149.95	1.17	48.06
Ni-BMZ	2.10	5.73	4.78	102.51	3.53	13.05
Cu-BMZ	2.62	2.74	4.99	9.20	3.21	14.93

a data set is large, one way to analyse those results is by applying dimension reduction methods such as Principal component analysis (PCA) [68]. PCA is one of the potential methods used in classification problems to reduce high-dimensionality of the data sets and the details of the analysis is described elsewhere. In the present study, simulated semiempirical parameters were exported to a text file and the statistical analysis were performed and plotted using R package (http://www.r-project.org). There are two main outputs from the PCA analysis: loadings and scores matrices. In which, loadings plot is used to identify the important variables, whereas, scores is used to describe the spatial distribution of samples on new axes called as principal components (PC). PC are considered as the dependent variable for regression and analysis of variance. Interpretation of PC is based on the fact that the most strongly correlated components are the one, farthest from the zero point either in positive or negative direction.

2.5.1   Scores and Loadings

Figure 2.12 shows the projection of the original variables in the same space (loading plot) and Figure 2.13 shows the projection of the simulated molecular descriptors defined by two principal components (score plot) [69]. From Figure 2.12, it can be seen

that bond length (BL), intensity of vibrational frequency (INT) and linear polarizability (ALP) show the negative values in the PC2 corresponding to an negative phenomenon. On the other hand bond angle (BA) and heat of formation (HOF) shows the negative phenomenon in the PC1. The very low score of band gap indicates that it has smaller contribution in trend determination.
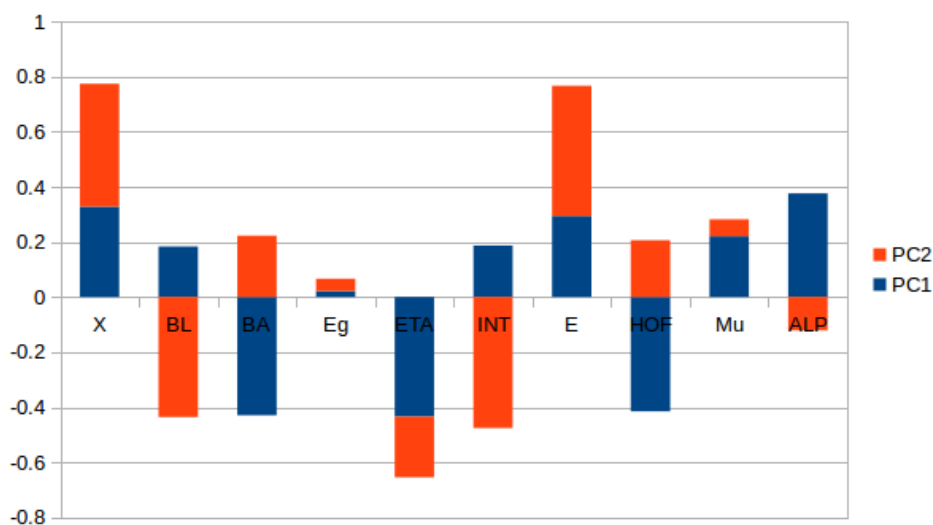
Fig. 2.12: Loading plot of PCA1 and PCA2
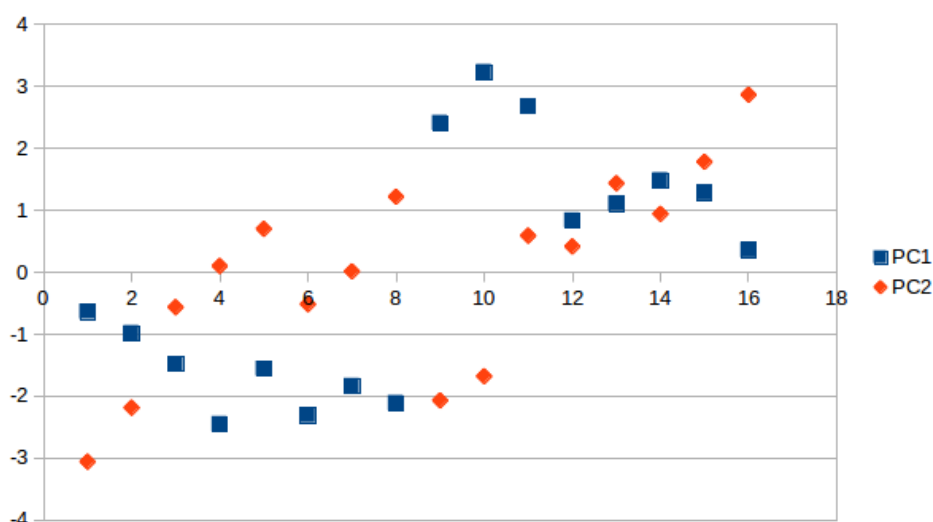
Fig. 2.13: Scoring plot of PCA1 and PCA2

31

2.5.2 Biplots

One way to visualize and interpret loadings and scores together is by using biplots. In which two variables, which are close and far from the origin, are correlated with respect to the variation in the molecular components [70]. Figure 2.14 shows the correlation biplot of PC1 and PC2. The center of the plot implies the average sample (not zero) and the points with low values are relative to other samples and the points with higher values are more independent.
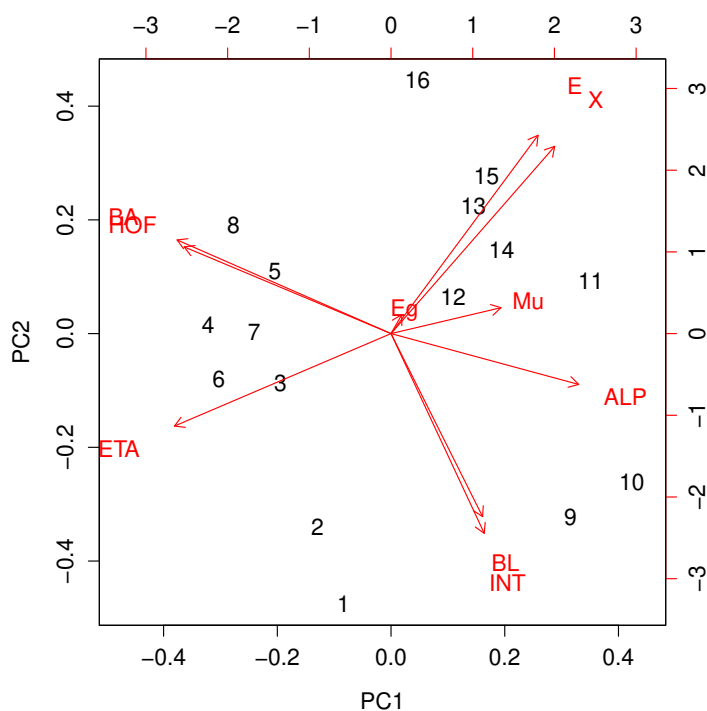
Fig. 2.14: Correlation biplot of PC1 and PC2

2.5.3 Scree test

Scree test is based on the fact that the relevant information is larger than the random noise [68]. It is often used to validate the PCA calculations. The test graph is plotted as the function of number of components and when only noise is modeled, the eigen

values are decline gradually. In practice, due to the large eigen values, it is difficult to visualize the things and in such a case logarithmic values are plotted. In the present case, both the graphs are shown in Figures 2.15 and 2.16 and the gradual decrement ensures the validation of study.
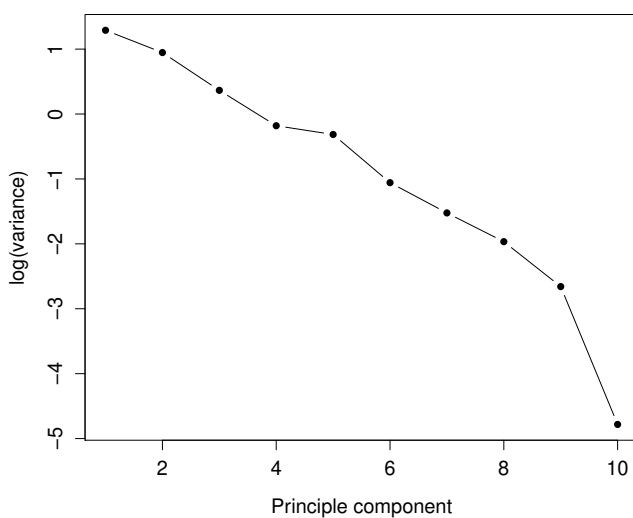
Fig. 2.15: Scree plot of PC1 and PC2
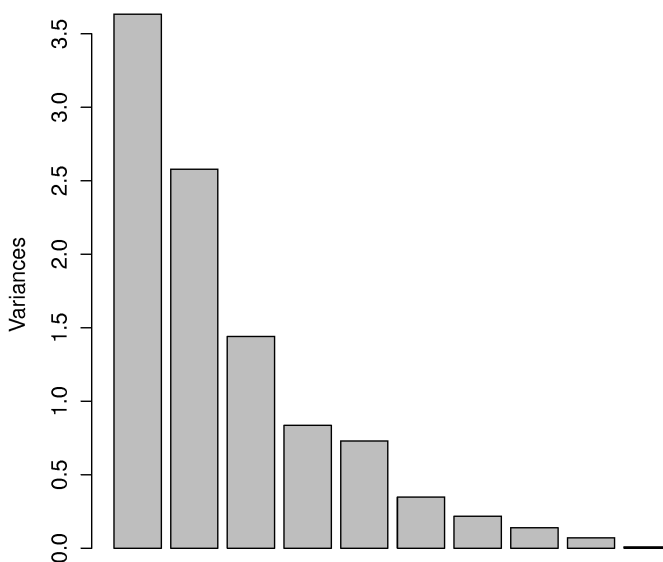
Fig. 2.16: Logarithmic Scree plot of PC1 and PC2

2.5.4   Analysis

2.5.4.1   First Principal Component - PCA1

The first principal component (PCA1) can be interpreted as a quantitative variable, that provides the overall predictive ability of the different sets of molecular descriptors for all the selected properties, the loadings of all the original variables (molecular properties) being positive in this component. The first principal component increases with increasing molecular energy (E) and linear polarizability (ALP) and decreases with bond angle (BA), global hardness value (ETA) and heat of formation (HOF) scores. This suggests that these five criteria vary together. If BA, ETA and HOF decreases correspondingly E and ALP increases. In other words, the first principal component can be used to distinguish between sets of molecular descriptors that, in general, perform well with all the considered properties (to the right in the score plot of Figure 2.12) and those with low overall prediction power (to the left in the score plot). Therefore, it can be concluded that the best models are mixed models, based on descriptors.

2.5.4.2   Second Principal Component - PCA2

The second principal component increases with decrease in BL and INT values and with increase in molecular energy. This indicates the increase in molecular energy with respect to bond length and correspondingly to the vibrational intensity. The analysis can be completed by interpreting the scatter plot of scores. In which each dot represents a member of a cluster and the lower and higher PCA1 values shows that the particular member has high influence (positive and negative, respect to the high and low values) on molecular properties. An reverse effect is expected from PCA2, i.e., positive for lower and negative for higher values.

2.5.4.3 PCAs Vs Hyperpolarizability

In order to correlate the principal components 1 and 2, the three dimensional data as two dimensional plots (Figures 2.17 and 2.18) were drawn. In which, the variation of hyperpolarizabilities with respect to principal components is shown and the hyperpolarizabilities are designated in a colour scale ranging from dark blue (zero) to pale yellow (160). Here the idea is to discuss the influence of principal components on nonlinear optical properties rather than to discuss which one provides better hyperpolarizabilities. Because, the influence of principal components can be interpreted in either way, i.e., they may contribute either positively or negatively. So, whether the hyperpolarizabilities are high or low, more the principal component value, higher its influence on the particular property in a specific complex. From Figure 2.17 excluding nonsub-
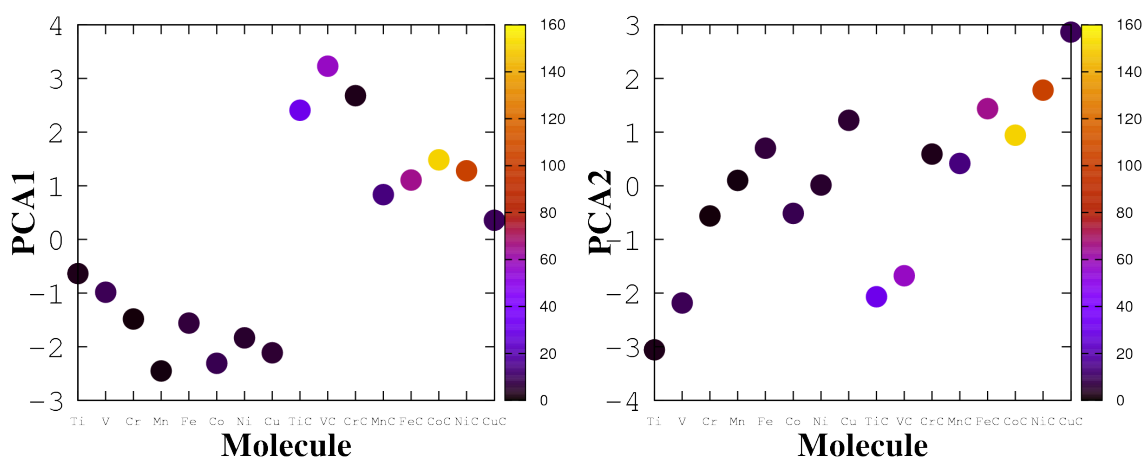
Fig. 2.17: Linear regression of first hyperpolarizabilty with (a) PCA1 and (b) PCA2 for MBMZ complexes with and without substituents

stituted Ti and V, in all other cases PCA2 dominates over PCA1. Certainly, there is an equal effect observed in the case of Cl substituted Co, but the trend is mainly dominates by PCA2. In second hyperpolarizabilty studies combined effect of PCA1 and PCA2 have been observed (Figure 2.18) for Cl substituted Mn, Fe and Co. But for Cl substituted Ti, V and Cr, PCA1 dominates and for Ni and Cu, PCA2 dominates. Overall, dominant effect of PCA2 have been observed for MBMZ complexes.
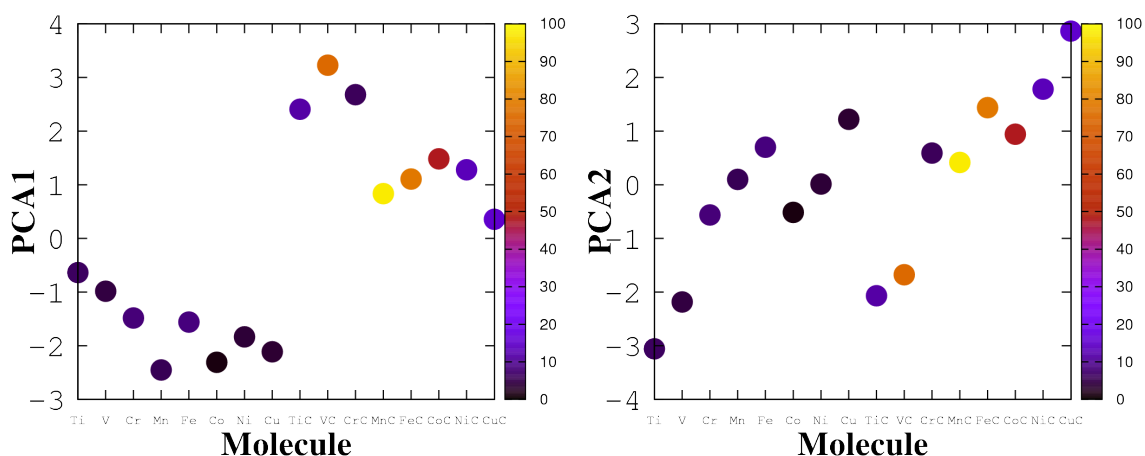
Fig. 2.18: Linear regression of second hyperpolarizabilty with (a) PCA1 and (b) PCA2 for MBMZ complexes with and without substituents

2.6 Effect of substituents

BMZ complexes can be synthesized with different halides (Cl, Br, I) or acetate (OAc) substituents depending on the precursor metal salt [71]. The substituents may play a role in structure stabilization as well as on linear and nonlinear optical properties of the system. Two benzimidazole based metal complexes, bis-benzimidazole Zn(II)-2R (Zn-R) and bis-benzimidazole Cd(II)-2R (Cd-R) (Where, R=Cl, Br, I, OAc) were chosen for the semiempirical calculations. The choice of metal ions is based on the fact that the d shell of Zn and Cd ions are completely filled, and therefore, it is expected that the major contribution of polarizability and hyperpolarizability arises due to the effect of substituent atoms [72–74].

The electronic distribution over the molecules can be visualized by plotting the isosurfaces of frontier molecular orbitals and are shown in Fig. 2.19. From the Fig. 2.19 (a-d), for HOMO, it can be seen that the major electronic cloud is distributed through metal-chloride (M-Cl) region in the case of Zn-Cl. The distribution of HOMO cloud increases with decrease in electronegativity of the substituents and a highest electronic distribution is observed in the case of Zn-I complex. But in the case of Zn-OAc
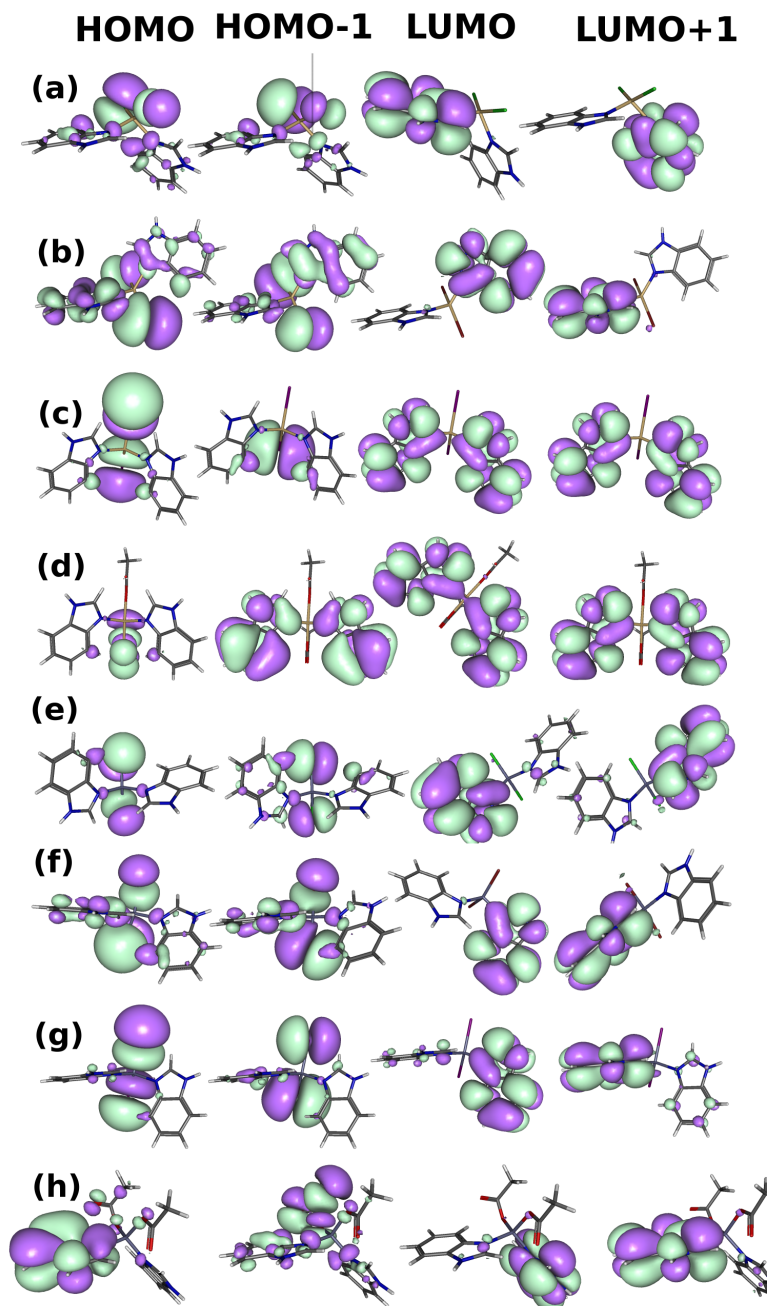
Fig. 2.19: Frontier Molecular Orbitals of (a-d) Zn-R and (e-h) Cd-R (R=Cl, Br, I, OAc)

complex, there is no electron contribution from acetate ions and the HOMO region is distributed over the metal ion. Similar scenario is also observed in the case of Cd complexes. Whereas for LUMO the electronic cloud is largely condensed over the ligand for all the metal complexes and it shows the possibility of intersystem charge trans-

fer in these molecules. The calculated frontier molecular orbitals of all the metal complexes and their energy gap values are given in Table 2.6. For both Cd and Zn metal complexes, decrease in electronegativity of the halogen substituents (Cl > Br > I), decreases the HOMO values and increases the LUMO values which results the decrease in energy gap (E_g) values. For Zn-OAc and Cd-OAc complexes the HOMO and LUMO values are almost equal to Zn-I, Cd-I complex values, respectively.

Table 2.6: Energy gap values of Zn-R and Cd-R complexes (a.u.)

Metal Complex	E_g
Zn-Cl	0.31
Zn-Br	0.30
Zn-I	0.27
Zn-OAc	0.28
Cd-Cl	0.31
Cd-Br	0.29
Cd-I	0.27
Cd-OAc	0.28

The calculated polarizability (α) and first and second order hyperpolarizability (β, γ) values of the metal complexes are given in Table 2.7. The decrease in electronegativity of the substituents increases the polarizability values of all the complexes. In other words, polarizability increases with decrease in energy band gap. This is obvious that the decreasing E_g favours more electronic cloud to get polarized and which in turn increases the polarizability values. Only a small difference was observed in polarizability values of Zn and Cd complexes. The reason for observed phenomena is due to the major electronic contribution arises from the substituent atoms. Of all the complexes Metal-I complex shows better polarizability followed by Metal-OAc complexes. The first and second order hyperpolarizability results of Zn-R and Cd-R complexes are similar to their polarizability results and Zn-I and Cd-I complexes exhibit highest β and γ values whereas Cl complexes exhibit the lowest values. Surprisingly, for Metal-OAc complexes, lowest β values are observed in contradiction to the α and γ values. It is a

well known fact that the first order hyperpolarizability of the molecules are symmetry dependent and since symmetry restrictions are not imposed in the present work and it might be the reason for the observed variation in β values of M-OAc complexes. From the results it can be seen that the γ values varying with respect to the electronegativity of the substituents. The variation in hyperpolarizability of the molecules is due to the change in electric quadrupoles induced in the complexes with respect to the electronegativity of the substituents [75, 76]. Anisotropic distribution of electrons in substituents causes less electron density in the z-direction of the molecule and more electron density in the other two directions of metal complex. Due to this, the applied electric field 'feels' more positive charge on the Z-X bond direction than the other two directions. This type of interaction is called δ-hole interactions and this anisotropic electrostatic distribution around a covalently bonded substituents can induce an electric quadrupole which is purely electronic in origin. The magnitude of electric quadrupoles are directly proportional to the electronegativity of the substituents and thus the variations observed in the calculated results.

Table 2.7: α, β and γ values of Zn-R and Cd-R Complexes

Complex	α (a.u.)	$\beta \times 10^{-30} (esu)$	$\gamma \times 10^{-30} (esu)$
Zn-Cl	227.41	2.348	1.822
Zn-Br	241.06	3.546	1.838
Zn-I	274.27	6.328	2.352
Zn-OAc	260.64	1.700	1.963
Cd-Cl	218.84	2.381	1.573
Cd-Br	239.58	4.298	2.382
Cd-I	270.30	8.735	3.147
Cd-OAc	258.60	1.233	1.654

2.7   Conclusion

The polarizability and hyperpolarizability values of benzimidazole metal complexes with and without substituents have been analysed using PM6 algorithm and TDHF formalism. From the ground state molecular properties such as energy gap value and heat of formation, ability of the molecule towards polarization by an external field and its stability was studied. Different molecular descriptors were calculated using the semiempirical quantum chemical calculations. They were correlated by means of principle component analysis and the first principal component shows strong correlation between molecular energy (E) and linear polarizability (ALP) and decreases with bond angle (BA), global hardness value (ETA) and heat of formation (HOF) values. Whereas, the second principal component dominated by only three parameters, in which BL and INT decreases whereas, molecular energy increases. These components provide a strong base to evaluate the nonlinear optical properties of the first row transition metal complexes. From the results of hyperpolarizability calculations, Co, Cu and Mn ions shows better values. Since they also have better HOF values, they were chosen as candidates for the experimental analysis. In terms of HOF, Cl and OAc substituents shows a negative value, indicating that the complexes with those substituents are easy to synthesize. Experimentaly it is hard to synthesize materials without substituents and hence, Cl and OAc based metal salts were used for the experimental analysis.

Synthesis of Nanostructures

3.1   Introduction

Most often, thin films are considered as suitable candidates for many device related applications due to their portability, compatibility with silicon photonics and planar waveguides. For linear and nonlinear optical applications, thin films are preferred form due to their low optical path lengths, which considerably reduces the scattering losses, and offer accurate measurement of NLO effects. Their planar waveguide structure is suitable for on-chip photonic circuits [77]. In the present study, we adopted a simple in situ chemical deposition method (modified liquid phase growth (LPG) technique) to deposit the thin films of benzimidazole and its metal complexes. The experimental parameters have been adjusted to obtain a uniform thin solid layer on the microscopic glass plates. Due to strong reactive nature of metal acetates with benzimidazole, it is not possible to deposit all the metal complexes as thin films. Alternatively, they have been synthesized as powders and embedded into a transparent polymer matrix to obtain free standing films. The working principle of liquid phase growth apparatus

and the necessary modifications made to deposit BMZ and its metal complexes are discussed in the following sections. Further, doping and deposition of free standing polymer films are also discussed in detail.

3.2   Modified Liquid Phase Growth Apparatus

Liquid Phase Growth apparatus is a simple and an efficient technique to grow single crystalline organic semiconducting thin films [78]. Fig 3.1 shows the schematic of liquid phase growth apparatus. Initially, a supersaturated solution with some extra solute is prepared and transfered to the vial. The substrate is fitted to a metal plate, which acts as a radiator, and it is wrapped with a sleeve of aluminum foil to prevent the undissolved material to interact with the substrate. The radiator is then inserted into the vial with a seal cap is attached on the top to prevent any form of evaporation or addition of atmospheric moisture to the solution. When the solution is heated through the bottom of the vial, convection flow starts and the solute molecules tend to transfered towards the substrate. Although the presence of the undissolved powder material seems superfluous, its presence is useful by automatically keeping the solution saturated even after the deposition of certain amount of solute as layers on the substrate. Thus it ensures the uniform deposition of thin films. The growth apparatus is equipped with a radiator made up of iron steel so that it can release heat from the liquid to the atmosphere to cool the substrate locally and to keep its temperature lower than that of the surrounding liquid. This makes the films grow directly on the substrate. In the present work, we made some modifications in the LPG experimental setup in order to suit the method for BMZ and its metal complex thin films deposition. The schematic of the modified setup is shown in Fig 3.2. In the modified LPG technique, to obtain a temperature gradient for growth, instead of fitting the substrate with metal plate here it was half immersed into the solution and the tem-
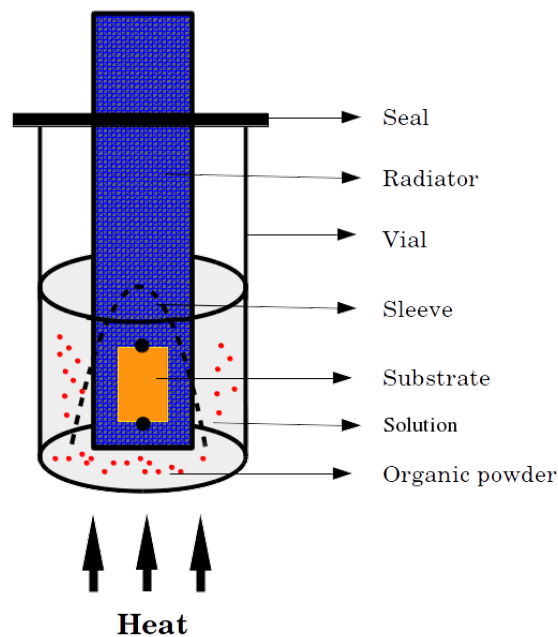
Fig. 3.1: Liquid phase growth apparatus to deposit single crystalline thin films

perature was applied only to the solution region. This offers more deposition area and reduces the effort of fitting glass substrates into the metal plate. Since, the solute is added into the solution with low molar concentration, a thin aluminum sheet placed around the substrate was removed in the present case, to control the number of molecules striking the substrate in LPG. Further, the apparatus is equipped with a refluxing tube to control the rate of evaporation of volatile solvents like ethanol. In order to optimize the thin film deposition, the modified LPG technique offers the control of various parameters such as temperature, rate of evaporation of solvent and pH of the solution etc. For instance, thickness of the depositing thin film can be easily varied by adjusting the concentration of the solution and/or temperature of the water/oil bath. In the present work, microscopic glass plates (7.5 × 2.5 × 0.1 mm) were used as substrates and they were cleaned by the procedure as described elsewhere [79]. Initially substrates were immersed into the 25% aquaregia solution in water for 30 mins to etch the surface slightly. Then they were washed with soap solution to re-
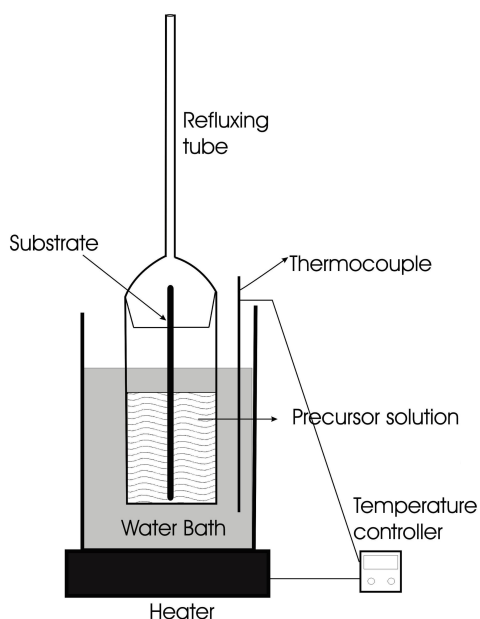
Fig. 3.2: Modified liquid phase growth apparatus used in the present sudy

move the acidic and grease like residuals. Finally, the substrates were ultrasonically treated using acetone and water for 10 mins. The well cleaned substrates were dried at 50 °C in a hot air oven, and then used for the deposition process.

3.3   Deposition of Thin Films

3.3.1   BMZ Thin Films

In order to optimize the growth parameters as well as for comparison purpose we initially deposited the thin films of BMZ. Analytical grade chemicals and reagents were used for the deposition and the precursor BMZ solution was prepared using ethanol as solvent with 0.1 M concentration. The solution temperature was varied from room temperature (RT - 29 °C) to 70 °C and thin films of BMZ were deposited for three different temperatures (50, 60 and 70 °C). No films were formed at temperature less than 50 °C and the solvent evaporation was very high for the temperatures more than 70 °C, hence the temperature range was fixed in between 50 and 70 °C. Thin films of BMZ
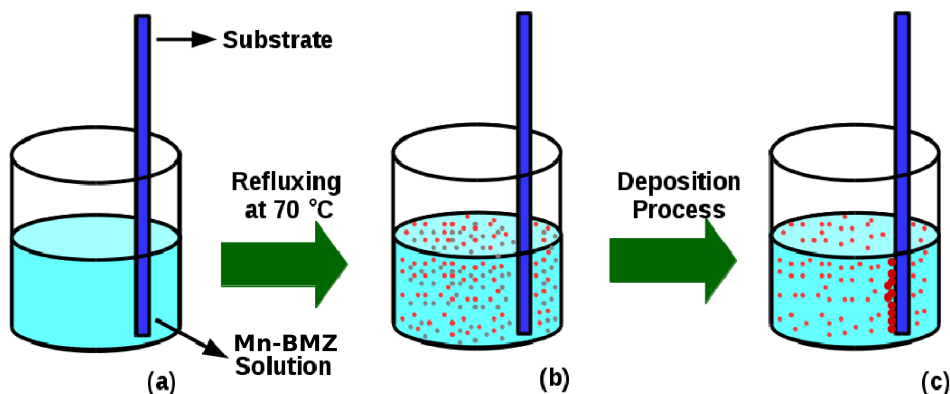
Fig. 3.3: (a) As prepared solution (b) Refluxing at 70 °C induces Mn-BMZ molecules (c) Induced molecules gain energy thermally and physisorped on the surface of substrate

were deposited by the immersion of two fused substrates into the corresponding solution for an hour. Then the substrates with films were removed from the solution, dried in a hot air oven for 2 mins and cleaned with hot water to remove the presence of any organic residuals.

3.3.2   Deposition of Co and Cu Complex Films

For the preparation of dichloro bis benzimidazole Co(II) (Co-BMZ) and dichloro bis benzimidazole Cu(II) (Cu-BMZ) metal complex films , respective metal chlorides ($CoCl_2.6H_2O$ and $CuCl_2.2H_2O$) and ligand (BMZ) were taken in 1:2 ratio. Mixture of methanol and dimethylformamide (3:1 ratio) was used to deposit Cu-BMZ films whereas ethanol solvent was used to deposit Co-BMZ films. For thin film deposition, two glass substrates were fused together by using a sellotape and dipped into the precursor solution then refluxed for 7 hours at 70 °C. The deposition process can be understood from the Fig. 3.3. Supply of thermal energy increases the reaction rate between ligand and the metal acetate. Since, the rate of reaction is proportional to the temperature, concentration and pH, increase in any one of which or all would increases the number of metal complex (MBMZ) molecules induced at a time. Often, if more number of molecules

present in the solution they tend to precipitate at the bottom of the solution container. But at optimum temperature, concentration and pH, only a limited number of M-BMZ molecules induced in the solution and the molecules tend to nucleate on the surface of the substrates due to the lower surface energy of the substrate [80, 81]. During the deposition process, the Cu-BMZ solution turns from pale green to dark green and Co-BMZ solution turns to dark blue from pale whitish blue. Then, the substrates with deposited films were removed from the solution and dried in a hot air oven at 50 °C for 2 mins. The as deposited samples (ASP) were annealed at 100 °C, 150 °C and 200 °C (hereafter the samples are termed as 100, 150 and 200) in the open air atmosphere for two hours, to study the effect of annealing temperature on the surface morphology of the films. With the current experimental setup, maximum reachable deposition temperature is 100 °C and with that, it is not possible for us to deposit the thin films of dichloro bis benzimidazole Mn(II) complex, since their HOF values are larger (See Chapter 2).

3.3.3   Deposition of Mn Complex Films

For the deposition of diaceto bis benzimidazole Mn(II) (Mn-BMZ) complex thin films, the ligand BMZ and manganese acetate tetrahydrate was taken in 2:1 ratio and dissolved separately using ethanol as the solvent. A few drops of acetic acid was added to the metal solution and then the BMZ solution was added dropwise with stirring to the metal solution at room temperature. This solution was transferred to a refluxing container kept at water bath. The solution was refluxed for five hours at 70 °C with two glass substrates fused together by a sellotape, whereupon the complex was deposited as thin film on the substrates. The thickness of the thin films can be altered by adjusting either the concentration or pH of the solution. In the present work, the concentration was fixed by chosing 0.1 M of BMZ (0.236 g) and 0.05 M of $(CH_3COO)_2$

Mn.4H$_2$O (0.245 g) in 40 ml of ethanol. The pH of the solution can be varied by varying the amount of acetic acid added to the metal solution. If the solution is too acidic no film formation was observed and if it is little acidic rapid precipitation was evidenced. After many trails with different values 0.2 ml of acetic acid (pH=8.06) was adopted as an optimized amount to deposit Mn-BMZ thin films. The formation of Mn-BMZ molecules can be evidenced from the change in colour of the solution, from pale brown to dark brown and after 5 hours, the solution turns into turbid. Then the substrates with brown colour thin films were removed from the solution, cleaned with double distilled water and dried in a hot air oven at 50 °C for 10 minutes. Films of as prepared samples (ASP) were annealed at 100, 150 and 200 °C (here after termed as 100, 150, 200) to study the effect of temperature on the properties of deposited films. Since, the cobalt acetate and copper acetate reacts rapidly with BMZ and forms the precipitate, it is not possible to deposit those complexes as thin films using modified LPG. So that the precipitates were embedded into a polymer matrix to study its properties, which is discussed elaborately in the following section.

3.4 Preparation of Free-standing Polymer Films

3.4.1 Synthesis of diaceto bis benzimidazole cobalt(II) and diaceto bis benzimidazole copper(II) complexes

The metal salts, cobalt acetate tetrahydrate (Co (CH$_3$COO)$_2$ (H$_2$O)$_4$) and cupric acetate (Co (CH$_3$COO)$_2$) were taken in 1:2 ratio with respect to the benzimidazole ligand. Both the ligand and metal complexes were dissolved separately in ethanol and stirred well. Then the ligand solution was added dropwise into the metal solution and stirred well. Upon the continuous addition of ligand solution, cobalt solution was turned to violet from pink colour and the copper solution was turned to red from dark green colour.

After few minutes of stirring, violet coloured precipitate was obtained in the case of cobalt complex and red precipitate was obtained in the case of copper complex. The synthesized materials were filtered, washed with DD water and dried in a hot air oven. To ensure the purity of the synthesized complexes column chromatography was used. The obtained product was subjected to vibrational spectrum analysis to confirm the presence of functional groups (see Appendix B).

3.4.2 Deposition of Co-BMZ-OAc and Cu-BMZ-Oac embedded PMMA films

To deposit the Co-BMZ-Oac and Cu-BMZ-OAc embedded PMMA thin films, 1 M of PMMA was dissolved in chloroform and different weight percentage (1, 3 and 5) of Co-BMZ-OAc and Cu-BMZ-OAc was added into the solution. Then the solution was transferred to a Teflon container and sonicated for 15 mins. The obtained clear polymeric solution was casted on clean petri dishes and dried well. After few days, free standing films of the Co-BMZ-OAc and Cu-BMZ-OAc embedded PMMA was scratched out from the glass plates. For comparison pristine PMMA films were also deposited in the similar way. Due to the non-homogeneous dispersion of metal complexes in polymeric solution, we confined the concentration level within 5 wt%. The thickness of the deposited polymeric films are around 1 micron.

3.4.3 Estimation of Thickness

Thickness of the deposited thin films was measured by simple air wedge technique. In this method, film deposited on a glass substrate was placed on a microscopic glass plate in order to form a wedge [82]. When the films illuminated with a CW laser of power 2 mW, and alternate dark and bright fringes were observed using a microscope. By calculating the number of fringes per unit length one can calculate the thickness

(t) of the sample using the relation,

$$t = \frac{l\lambda}{2\Delta X} \qquad (3.1)$$

Where, l is the length of the sample illuminated, λ is the wavelength of source and ΔX is the number of fringes per unit length. The calculated thickness values of the films are listed in Table 3.1. For BMZ films, the variation in thickness with respect to solu-

Sample	Preparation / Annealing Temperature (°C)	Thickness (nm)
BMZ	50	108.3
	60	144.4
	70	162.5
Co-BMZ	ASP	432.1
	100	420.3
	150	416.9
	200	409.5
Cu-BMZ	ASP	496.2
	100	487.4
	150	483.1
	200	476.8
Mn-BMZ	ASP	416.3
	100	411.0
	150	406.5
	200	392.9

Table 3.1: Estimated thickness of BMZ and its metal complex thin films

tion temperature is due to the deposition process. During the deposition of BMZ thin films, there is no possibility of chemical reaction and physisorption, which is the reason for the deposition of material as thin films [83]. Physisorption of molecules are due to weak van der Waals forces and often this forces are not enough to induce a nucleation. Therefore, supply of thermal energy is necessary to induce interactions between the molecules and substrate [80]. In the present work, at temperatures lower than 50 °C

no films were obtained due to the insufficient energy supplied to the molecules to nucleate on the substrate. When the solution temperature is about 50 °C the molecules gain sufficient energy to nucleate and can form grains on the substrate. In principle, energy gained by the molecules are directly proportional to the deposition rate and thickness of the films, i.e., with increasing temperature more number of molecules tend to adsorb on the surface of the substrate and this can be evident from the thickness of the films deposited at 60 and 70 °C. In the case of metal complex films, since the concentration, temperature and pH are fixed, the thickness of the films is directly related to the rate of formation of the metal complex molecule and the rate of adsorption of the molecular clusters on the glass substrate. But the variation in the thickness of the annealed samples was observed due to the surface diffusion and surface evaporation during the annealing process. For polymer matrices, free standing films was kept in between two glass slides and the similar principle was used to measure its thickness. Irrespective of metal complex concentration all the films are approximately 1 micron thick.

3.5   Nanoparticles Synthesis

Benzimidazole and its derivatives, especially metal complexes find potential applications in the biological studies. In the recent past they were widely investigated for anticancer related studies. In order to treat the complexes with biological substances we have synthesized them as nanoparticles. Initially, the material was synthesized as powder and then by using reprecipitation technique they were fabricated as nanoparticles.

3.5.1   Material Synthesis

All the raw materials used for the synthesis of Co-BMZ and Cu-BMZ complexes were reagent grade and purchased from Merck chemicals. For the synthesis, respective metal chlorides ($CoCl_2.6H_2O$ and $CuCl_2.2H_2O$) and ligand (BMZ) were taken in 1:2 ratio and dissolved in ethanol separately. The BMZ solution was transferred to a glass container and heated at 70 °C for an hour. Then the metal solution (either cobalt or copper chloride solution) was added dropwise into the BMZ solution. This solution was refluxed for 24 hours and transferred to another beaker kept at room temperature. Then, the beaker was covered with aluminum foil and kept undisturbed for a week. Thereupon, either blue or green precipitate was obtained depending upon the metal solution utilized. The purity of the final product was ensured by means of column chromatography and the molecular structure of the complexes were confirmed by FTIR analysis (same as thin film spectrum - See Fig. 4.1 and 4.2). Further, these powdered samples were used for the preparation of nanoparticles.

3.5.2   Synthesis of Nanoparticles of Co-BMZ and Cu-BMZ

For the preparation of nanoparticles, a reprecipitation method was employed and the details can be found elsewhere [84]. The idea is by rapidly mixing the solution of the target material to a solvent, where the solubility of the material is very poor or non-soluble and at the same time the solvent should dissolve well with the poor solvent. This situation leads to rapid precipitation of the target material. In the present work, water was chosen as the poor solvent and was kept above 70 °C for better results. The product (either Co-BMZ or Cu-BMZ) was dissolved in methanol and the solution was filtered many times to obtain a clear solution without any undissolved powder/particles. Then the solution was loaded in a syringe with needle of diameter less than 1 micron. This solution was rapidly sprayed on to the water. The obtained colloidal suspension

is stable for several weeks and was used for the further characterization studies.

3.6 Conclusion

Modified liquid phase growth apparatus was used to deposit the benzimidazole and its metal complex thin films. The role of different deposition temperature on the thickness of benzimidazole thin films have been discussed. Further, physisorption process in the deposition of metal complex films also have been discussed. Some metal acetate complexes of benzimidazole precipitate immediately are embedded into a PMMA matrix and caste as a polymeric free standing films. The thickness of all the samples was estimated using a air wedge technique. For biological studies two of the complexes, Co and Cu based dichloride bis benzimidazole, were synthesized by using repreciptation technique.

Chapter
4

Structural and Surface Analysis

4.1 Introduction

In this work, nanostructures of benzimidazole are formed as: (i) thin films, (ii) free standing films and (iii) nanoparticles. In the case of thin films, dichloro bis benzimidazole cobalt (II) (Co-BMZ), dichloro bis benzimidazole copper (II) (Cu-BMZ) and diacetobis benzimidazole manganese (II) (Mn-BMZ) systems were fabricated. These films were annealed at different temperatures in order to study the effect of annealing on structural and surface morphology properties of the samples. In order to benchmark the values, pristine BMZ films were also deposited with same thickness. In the case of free standing films, diaceto bis benzimidazole cobalt (II) (Co-BMZ-OAc) and diaceto bis copper (II) (Cu-BMZ-OAc) powders were embedded into PMMA matrices in different weight percentages. The dichloro bis benzimidazole cobalt (II) (Co-BMZ-NP) and dichloro bis benzimidazole copper (II) (Cu-BMZ-NP) nanoparticles were synthesized by reprecipitation method.

In order to confirm the structural and surface properties of the synthesized nanos-

tructures, they were subjected to various characterization studies. The crystalanity of the samples were analysed by powder X-ray diffraction (PXRD) studies using XPERT-PRO X-ray diffractometer. It is found that all samples are amorphous other than pristine BMZ. The structure of Mn-BMZ is not known and it is amorphous in nature. In order to derive its structure, it is subjected to compositional analysis using Bruker energy-dispersive X-ray spectrum (EDS) (operating voltage 5 kV) and the electron paramagnetic resonance (EPR) analysis at room temperature (RT) using JEOL JES-FA200 EPR spectrometer (X band frequency, microwave power is 1 mW and the modulation amplitude is about 160.00). Further, all the samples were subjected to FT-IR spectrum analysis using Perkin Elmer Spectrum RX I system. Renishaw inVia Reflex Raman spectrometer was employed to record the Raman spectra of the samples. An Ar ion laser of wavelength 514.5 nm and spot size 5 μm was used as the source and all the spectra were recorded in backscattering geometry. Surface topography of the thin films were studied using SEIKO SPA400 - SPI4000 AFM unit in dynamic scanning mode with a scan speed of 0.5 Hz and the radius of about 10 nm. Apart from the structural confirmation of Co-BMZ-OAc and Cu-BMZ-OAc by FT-IR analysis, the combined effect of the metal organic complexes (MBMZ) in polymeric system was studied using computational simulation. For that, semiempircal solid state calculations were used. Further, the samples were subjected to thermo-optic analysis to derive their thermo-optic coefficient. Dynamic light scattering (DLS) and zeta potential of the nanoparticles were measured using Malvern Zetasizer Nano ZS ZEN 3600 instrument. All the measurements were carried using 1 ml of the colloidal solution in a clean, light scattering cell at 25°C. Transmission electron microscopy (TEM) analysis was performed using a Philips CM20 instrument with an accelerating voltage of about 200 kV. The forthcoming sections describe the obtained results from these characterization techniques in detail.

4.2   Benzimidazole Thin Films

The IR absorption of BMZ powders, collected from BMZ films deposited at 60 °C, is shown in Figure 4.1. Broad absorption appeared between 2300 and 3400 cm^{-1} is due to the presence of aromatic C-H and N-H bands. The sharp absorption peaks appeared at 1465 and 1409 cm^{-1} can be attributed to C=C stretching vibrations and the peaks appeared between the region 1150 and 745 cm^{-1} are due to the inplane and out of plane vibrations of C-H band. Peaks appeared at 1764 cm^{-1} and 627 cm^{-1} are due to N-H inplane and N-H out of plane vibrations, respectively. The strong absorption at 1241 cm^{-1} and 420 cm^{-1} is due to C-C stretching and C-C-C out of plane bending, respectively. Further, there is no peak shifts appeared or no other organic group impurity peaks related to ethanol or OH are observed. This ensures the purity of the deposited films. Also, there is no significant changes observed in the FTIR spectrum of the films deposited at different solution temperatures (50, 60 and 70 °C).
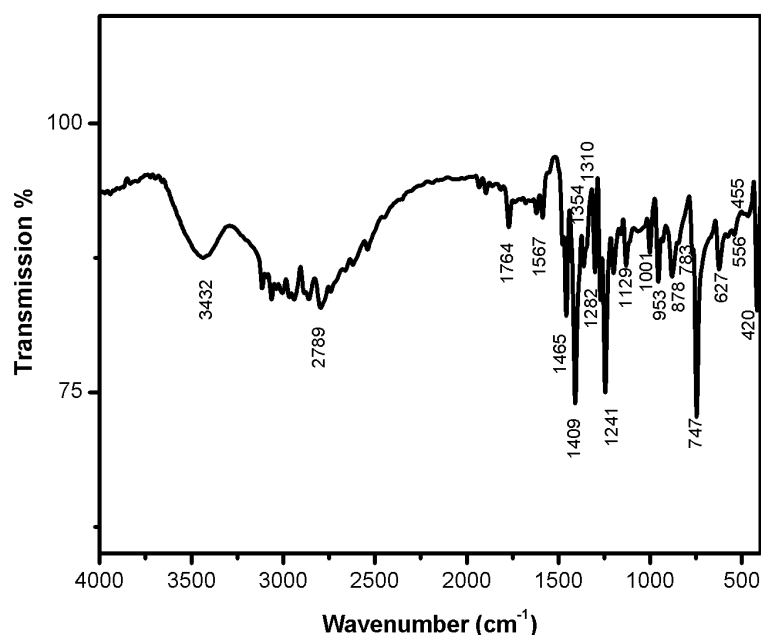
Fig. 4.1: FTIR spectrum of BMZ film prepared at 60 °C

Figure 4.2 shows the surface topography of the films prepared at different solu-

55
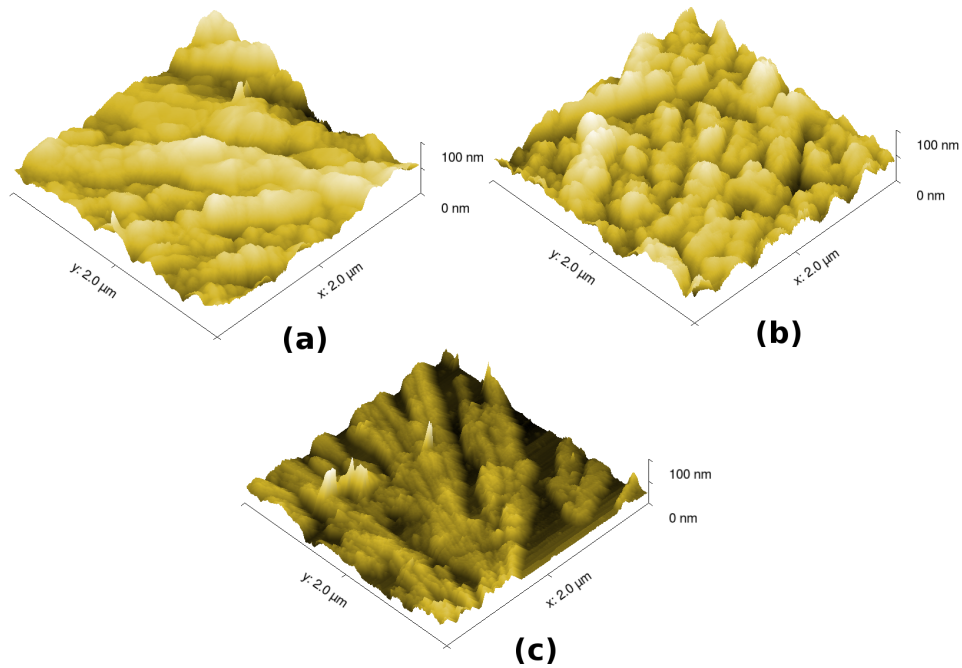
Fig. 4.2: AFM surface topography of BMZ films, prepared at (a) 50 °C (b) 60 °C and (c) 70 °C

tion temperatures. The surface topography of the films varies with different solution temperatures. The size of the grains (Figure 4.2) decreases for the films deposited at 60 °C and bulk adsorption of particles have been observed for the films deposited at 70 °C when compared to the films deposited at 50 °C. This in turn confirms the role of solution temperatures in film deposition. Calculated root mean square (RMS) roughness, skewness and kurtosis values of the BMZ films are given in Table 4.1. The values of skewness are negative and kurtosis is less than 3, and hence it is concluded that all the films posses predominant valley and have a flat surface [85]. From Table 4.1, it is evident that the flatness and skewness increases for the films deposited at 60 °C, means that, the films deposited at 60 °C are more planar and homogeneous than the films deposited at 50 °C and 70 °C.

The XRD patterns of BMZ films deposited at different solution temperatures is shown in the Figure 4.3. XRD patterns reveal that BMZ films prepared at different solution temperature contain only a single peak corresponding to (110) plane [86, 87].

BMZ films preparation temperature (°C)	RMS (R_q) (nm)	Skewness (R_sk) (arb.)	Kurtosis (R_ku) (arb.)
50	22.8	-0.50	2.93
60	20.9	-0.26	2.17
70	28.3	-0.42	2.75

Table 4.1: RMS, Skewness and Kurtosis values of BMZ estimated from AFM surface topography

This is due to the molecules tend to arrange only in (110) plane and confirms the single crystalline nature of the films. The crystallite size of the BMZ films was calculated using the well known Debye-Scherrer's relation:

$$D = \frac{0.9\lambda}{\beta cos\theta}$$ (4.1)

where, D is the crystallite size, λ is the wavelength of the x-ray source and β is the line broadening at half the maximum intensity. The calculated crystallite size with respect to solution temperatures is shown in Figure 4.4. The results are similar to the trend observed in AFM images. The variation in crystallite size confirms the contribution of solution temperature to the grain growth mechanism in thin films [88, 89]. With increasing temperature more number of nucleation sites can be possible and this in turn reduce the crystallite size. But at 70 °C evaporation of ethanol leads to rapid adsorption results an increase in crystallite size.

Even though no significant variations are observed in FTIR and XRD analyses of the deposited BMZ thin films, variation in thickness has been observed (See chapter 3, section 3.4.3) and it plays significant role in linear and nonlinear optical properties of the films. The variation in thickness with respect to solution temperature is due to the deposition process. During the deposition of BMZ thin films, there is no possibility of chemical reaction and physisorption process, thus provides the deposition of material as thin films [83]. Physisorption of molecules is due to weak van der Waals force
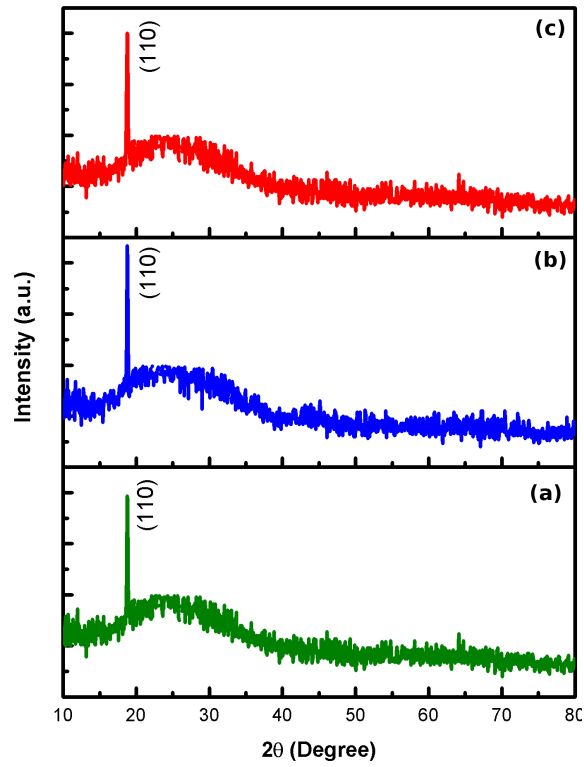
Fig. 4.3: X-ray diffraction patterns of BMZ thin films prepared at (a) 50 °C (b) 60 °C and (c) 70 °C
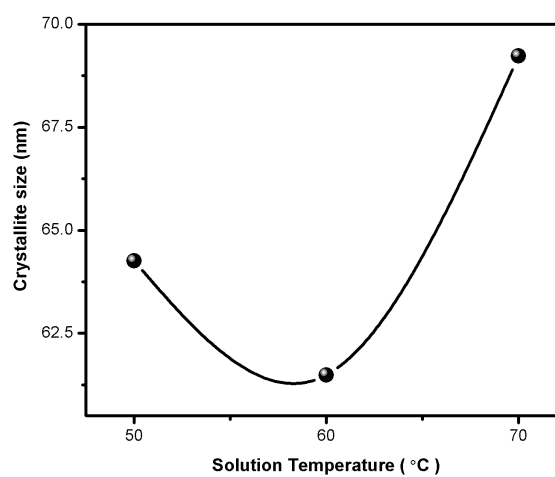
Fig. 4.4: Crystallite size of BMZ thin films

and often this force is not enough to induce a nucleation. Therefore, supply of thermal energy is necessary to induce interactions between the molecules and substrate [80]. In the present work, at temperatures lower than 50 °C no films were obtained due to the insufficient energy supplied to the molecules to nucleate on the substrate. When the solution temperature is about 50 °C the molecules gain sufficient energy to nucleate and can form grains on the substrate. In principle, energy gained by the molecules are directly proportional to the deposition rate and thickness of the films, i.e., with increasing temperature more number of molecules tend to adsorb on the surface of the substrate and this can be evident from the thickness of the films deposited at 60 ° C and 70 °C.

4.3   Dichloro bis benzimidazole Co(II) and Cu(II) Thin Films

4.3.1   Structural analysis

In the present work, functional groups of the deposited films were investigated using Fourier Transform Infrared and Raman spectral studies and compared with the previous reports [90–94]. Generally, metalated bis-BMZ (M-BMZ) molecules show a slight shift in the FTIR spectrum compared to that of benzimidazole's spectrum. This shift corresponds to the electronegativity of the incorporated metal. In the present case, the shift in the M-BMZ peak positions in FTIR spectra (Fig. 4.5(a) and 4.5(b)) indicates the formation Co-BMZ and Cu-BMZ metal complexes. The peak at 422 cm^{-1} and 427 cm^{-1} in Co-BMZ and Cu-BMZ spectrum, respectively confirms the presence of metal-ligand vibrations. Major changes observed in the ring modes of Co-BMZ and Cu-BMZ molecules compared to that of BMZ can be attributed to the metal-nitrogen interactions. Presence of N-H vibrations at 1110 and 635 cm^{-1} in Co-BMZ, and 1113 and 650
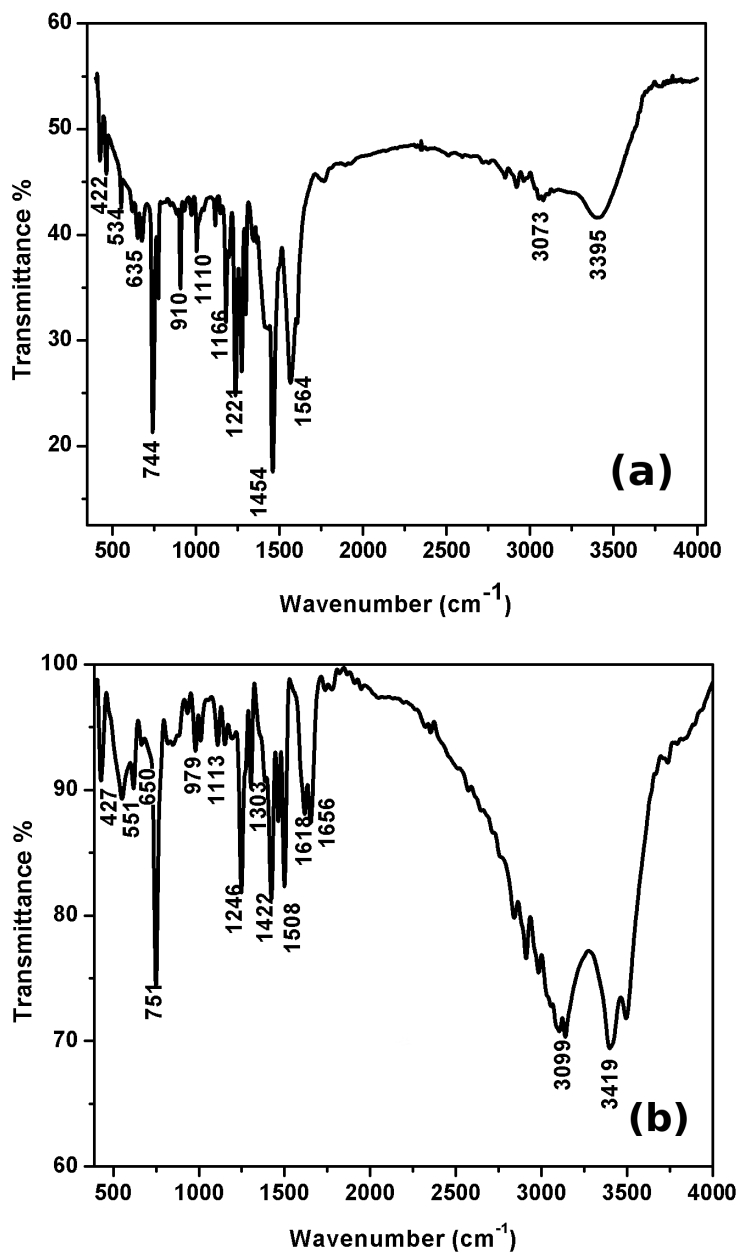
Fig. 4.5: FTIR spectra of (a) Co-BMZ and (b) Cu-BMZ complex thin films

cm^{-1} in Cu-BMZ indicates that the N-H bond at N1 position remains unaffected and the metal is coordinated through the molecule by means of N2 atom. Strong absorption peak observed in the region 3600 - 2400 cm^{-1} of both the spectra is similar to that the BMZ spectrum which is due to the strong intermolecular hydrogen bonding of BMZ in solid state. We limited the FTIR studies only for as prepared (ASP) samples, because of the difficulties in removing the annealed films by scratching. Fig. 4.6(a) and 4.6(b) show the Raman spectra of Co-BMZ and Cu-BMZ films, respectively. In Raman analysis, stretching vibrations are observed at 773 and 777 cm^{-1} corresponding to the metal-ligand co-ordination effect. A broad signal appeared in both the spectra in the region between 1000 and 1200 cm^{-1} is due to the stretching vibrations of C=N, in which the N is coordinated to the metal, thus supporting the tetrahedral coordination of metal with BMZ molecules. Further, the recorded spectra confirms the coordination of the metal ions with benzimidazole ligand, through N2 atom. All the annealed films were subjected to Raman analysis and they exhibit a significant change when compared to ASP spectrum. Variation in the intensity of the Raman spectrum of annealed films can be attributed to the thermal degradation of the metal complexes. In the case of Co-BMZ films, decrease in peak intensity observed at 773, 1271 and 1359 cm^{-1} can be ascribed to the breaking of hydrogen bonds between the molecules at higher temperature [95]. Whereas in the case of Cu-BMZ films, decrease in peak intensity of the spectra can be attributed to the thermal decomposition of the complex, i.e., bis structure is distorted to form a mono structure of BMZ metal complex, similar to the case of quinoline [96].

4.3.2   Surface analysis

Effect of temperature on the surface topography of the films was analysed by AFM studies. Figs. 4.7 and 4.8 show the surface topography of the Co-BMZ and Cu-BMZ thin
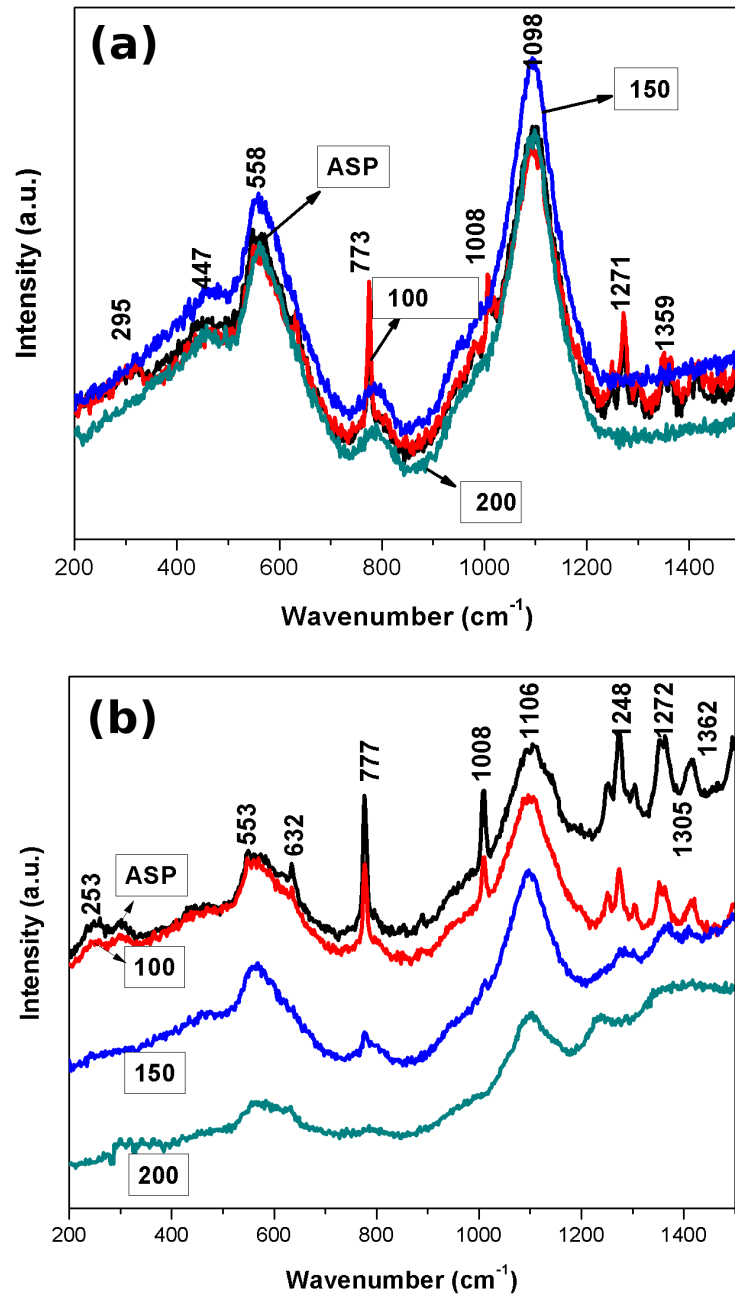
Fig. 4.6: Raman spectra of (a) Co-BMZ and (b) Cu-BMZ thin films, prepared at RT, 100 °C, 150 °C and 200 ° C

films respectively. The skewness, kurtosis and root mean square roughness (RMS) values were calculated for all the samples and are given in Table 4.2. These parameters are widely used to identify the changes in surface morphology and used to evaluate

the defect sites and growth mechanism of thin film surfaces. Bright grain spots appeared on the images are due to repulsive forces [97] between the tip and surface caused by higher electron density at the particular point of the surface. Fig. 4.7(a) shows the morphology of the as prepared Co-BMZ sample with an average grain size of 21 nm. Fig. 4.7(b) and 4.7(c) reveals that the surface smoothness increases due to annealing at 100 °C and 150 °C and correspondingly their grain size decreases to 3.54 and 2.64 nm, respectively from 21.41 nm of ASP samples. Even though annealing at 150 °C gives better smoothness, the low skewness obtained can be interpreted due to the slight distortion of films at this temperature. The agglomeration of grains at 200 °C leads to the formation of bulk patches. In the case of Cu-BMZ films, the grain size increases with annealing temperature and the surface smoothness of the films decreases. Films annealed at 150 °C shows more peaks on the surface with an average grain size of about 7.5 nm. Cu-BMZ film annealed at 200 °C also shows the massive agglomeration of grains with bulk patches. It is a well known fact that the diffusion coefficient exponentially increases with the temperature. Thus the observed increase in surface homogeneity of the films with increasing temperature can be interpreted to surface diffusion [98]. However, breaking of molecular bonds at higher temperatures leads to the surface distortion of the films [99].

Table 4.2: Grain size, RMS, Skewness and Kurtosis values of the Co-BMZ and Cu-BMZ films

Sample	Grain size (nm^2)		RMS value (R_q) (nm)		Skewness (R_sk)		Kurtosis (R_ku)	
	Co-BMZ	Cu-BMZ	Co-BMZ	Cu-BMZ	Co-BMZ	Cu-BMZ	Co-BMZ	Cu-BMZ
ASP	21.41	4.04	11.86	2.18	0.60	0.01	-0.23	-0.49
100	3.54	5.74	0.57	2.65	0.40	1.35	4.04	2.79
150	2.64	7.50	0.63	3.63	0.01	1.45	0.15	3.25
200	13.82	44.10	7.48	22.10	0.46	0.71	0.17	0.16
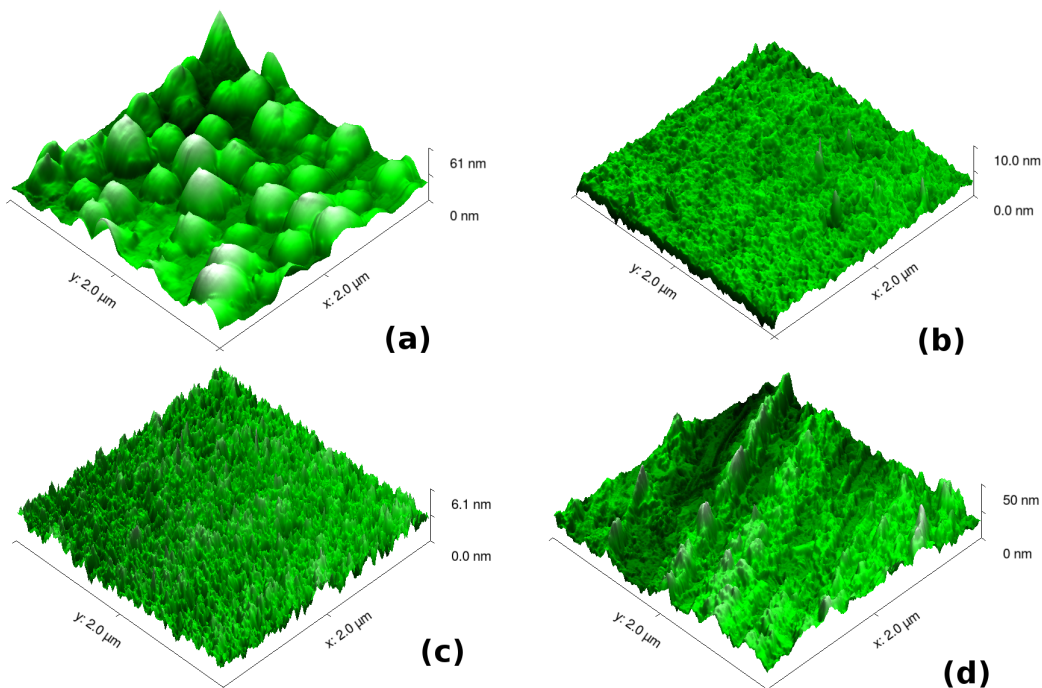
Fig. 4.7: Surface topography of Co-BMZ thin films: (a) As prepared, annealed at (b) 100 °C (c) 150 °C and (d) 200 °C
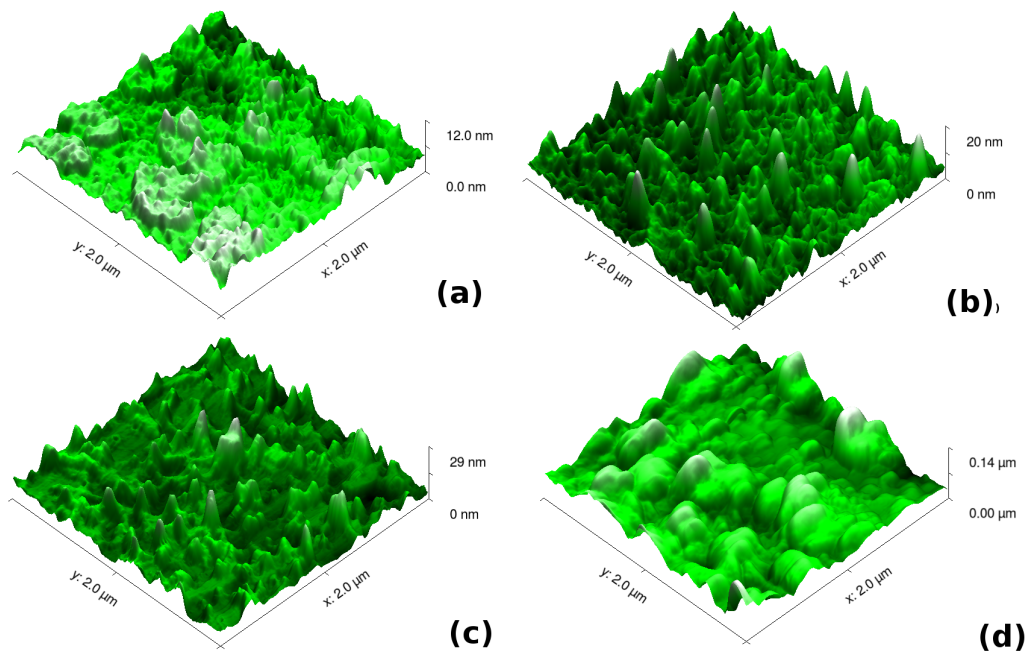
Fig. 4.8: Surface topography of Cu-BMZ thin films: (a) As prepared, annealed at (b) 100°C (c) 150°C and (d) 200°C

4.4   Diaceto bis benzimidazole Mn(II) Thin Films

4.4.1   Structural analysis

The FTIR spectrum of Mn-BMZ powder, scratched from the thin film, is shown in Fig. 4.9. Previous reports suggest that the vibrational spectrum of BMZ metal (M-BMZ) complexes almost resembles the benzimidazole spectrum except some specific metal-ligand absorption effects in the lower wavenumber region [92, 100–102]. A slight blue shift can be observed in the vibrational pattern of metal complexes with respect to BMZ spectrum. The amount of shift depends on the electrovalency of the incorporated metal ion. The upward shift observed in the Mn-BMZ spectrum can be attributed to the formation of metal complex. Further the presence of vibrational peak at far infrared region (~ 350 cm^{-1}) can be inferred as the evidence for metal-ligand (ν(M-L)) coordination. The presence of N-H vibrations in the region of 2700 cm^{-1} indicates that the N1 position of imidazolate ion remain unaffected and also confirms the formation of metal complex is through the N2 atom. Presence of absorption bands in the region 1500 cm^{-1} can be attributed to the influence of acetate ions [102]. Absorption bands in the region 3000 cm^{-1} are due to the solid state absorption of the samples (i.e., weak hydrogen bond formation between benzene rings) and the bands in the region of 3600 - 3800 cm^{-1} are attributed to the presence of water molecules in the complex [103]. Since it is hard to scratch the heat treated films, FTIR spectra of those were not recorded. The compositional analysis by energy-dispersive X-ray spectroscopy of the samples further confirms the incorporation of Mn ions in the BMZ medium (Fig. 4.10 (a)). The empirical formula derived from the EDS spectrum suggests that bis form of BMZ with the metal ion.

The powder EPR spectrum of Mn-BMZ complex (Fig. 4.10 (b)) recorded at room temperature exhibits hyperfine groups corresponding to monomeric manganese com-
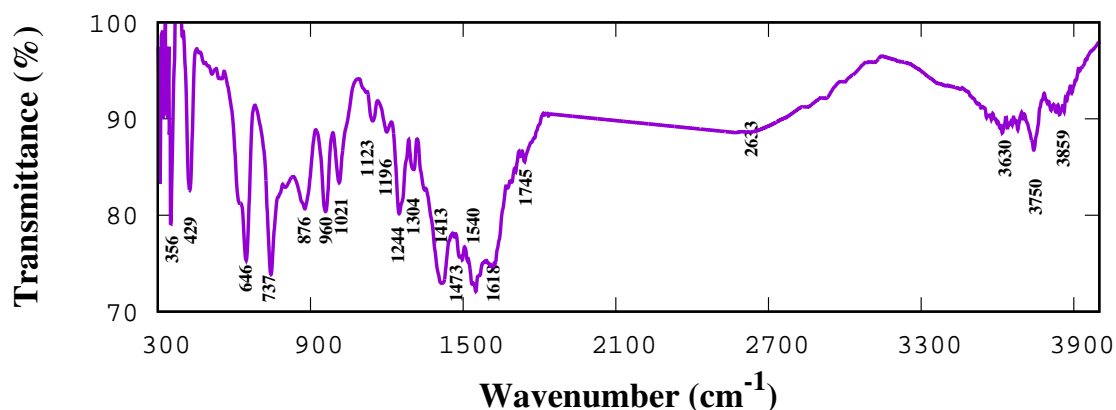
Fig. 4.9: FT-IR spectrum of Mn-BMZ complex

plex (Mn, I=5/2) with smaller zero field splitting energy [104, 105]. Signal at g=2.4 is due to the transition from S=2 manifold, corresponding to $\Delta M_S = \pm 2$ transitions and signal at g=1.89 is due to the free Mn(II) ion. The signals from g=3.3 and 1.4 are due to two $\Delta M_S = \pm 1$ transitions arose from S=2 manifold. Low field signal observed at g=6.2 corresponds to S=1 manifold and they are only weakly allowed. The partially resolved structures at g=6.2 and g=3.3 can be attributed to the interaction between manganese and nitrogen which confirms the coordination of metal ion with benzimidazole ligand [104]. From the spectral and compositional analyses, the structure of Mn-BMZ complex was predicted as diaceto bis-benzimidazole Mn(II) and it is shown in Fig. 4.11.

In order to confirm the same, the vibrational spectrum of the predicted complex was simulated using PM6 algorithm embedded in MOPAC2012 program. The calculated values were scaled and fitted (Fig. 4.12) using the method reported elsewhere [106]. The calculated values are in good agreement with the observed frequencies and the percentage of error is approximated about less than 2%.
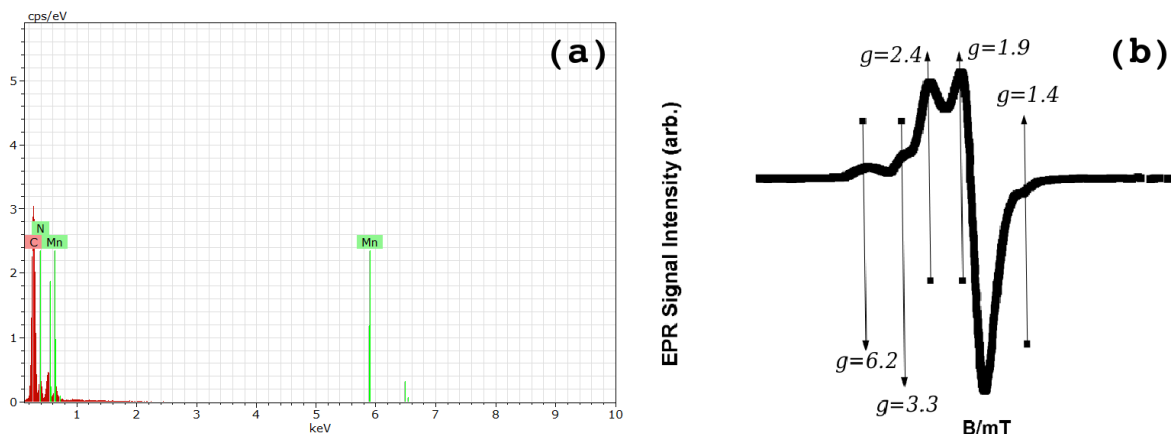
Fig. 4.10: (a) EDS and (b) EPR spectrum of Mn-BMZ complex
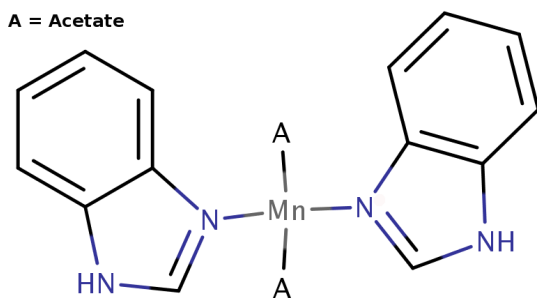
Fig. 4.11: Predicted structure of the Mn-BMZ complex
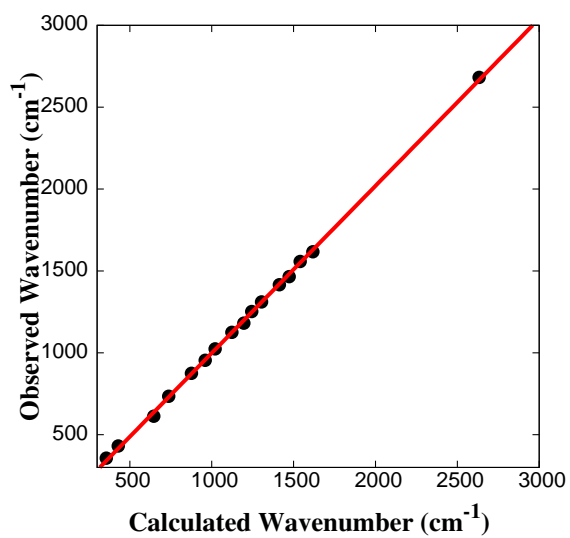
Fig. 4.12: Fitted values of observed and calculated frequencies

4.4.2   Surface analysis

Surface morphology of the thin films plays a vital role in the linear and nonlinear optical properties. The atomic force microscopy images of the as prepared and annealed Mn-BMZ samples are shown in Fig. 4.13 and the corresponding grain size, root mean square roughness (R_q), skewness ($R_s k$) and kurtosis ($R_k u$) values are given in Table 4.3. It is a well known fact that the diffusion coefficient exponentially increases with temperature. Thus the increase in surface homogeneity of the films with increasing annealing temperature can be interpreted to surface diffusion [107]. This can be further evidenced from the R_q values given in Table 4.3. The decrease in R_q values, for the films annealed at 100 °C and 150 °C corresponds to the increase in homogeneity of the film surface. Also the decrement in $R_s k$ values of these films reveals the surface with more planar and predominant by the valleys. Further $R_k u$ values showed that the platykurtic nature increases for the films annealed at 100 °C and 150°C. But the dramatic change in the surface parameters observed for the films annealed at 200 °C is due to the surface distortion of the films.

Table 4.3: Calculated surface parameters of Mn-BMZ thin films

Sample	Grain Size (nm^2)	RMS Roughness (R_q) (nm)	Skewness (R_sk) (arb.)	Kurtosis (R_ku) (arb.)
ASP	40.96	10.77	2.34	8.2
100	29.07	5.69	-0.03	2.5
150	28.03	5.56	0.22	0.64
200	80.64	11.8	3.43	28.1

The molecular distortion at surface may either due to the evaporation of the molecules from the surface or due to the decomposition of the molecules. This can be investigated by analyzing the molecular composition of Mn-BMZ by EDS and Raman studies. At higher temperatures, even though there is a reduction in the overall weight percentage of the molecules, the composition of the samples remains almost invari-
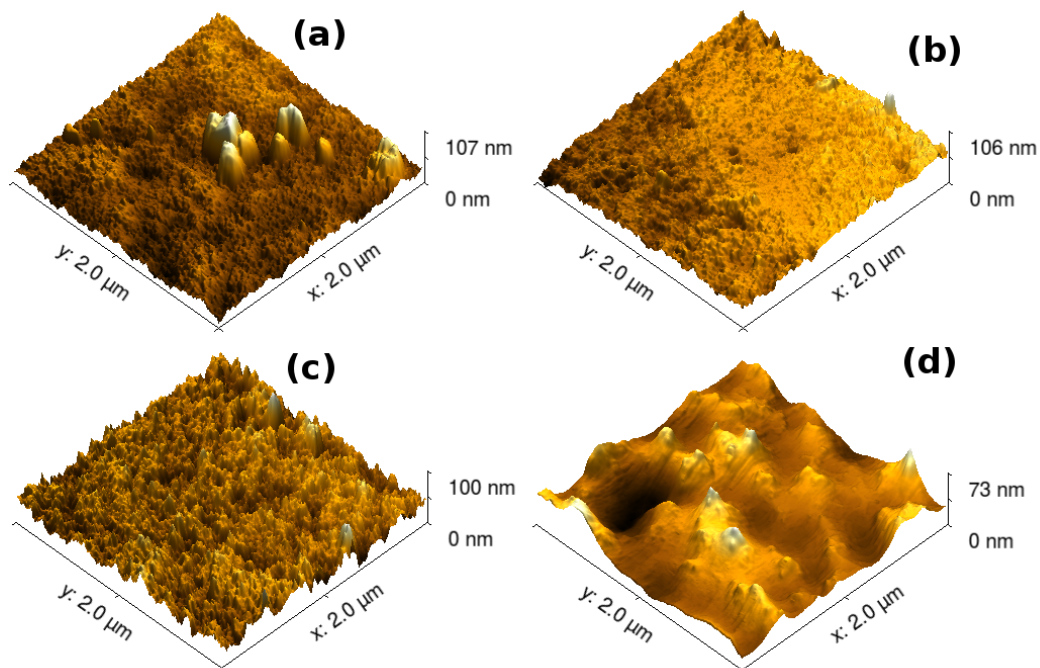
Fig. 4.13: Surface morphology of Mn-BMZ thin films: (a) As prepared, and annealed at (b) 100 °C (c) 150 ° C (d) 200 ° C
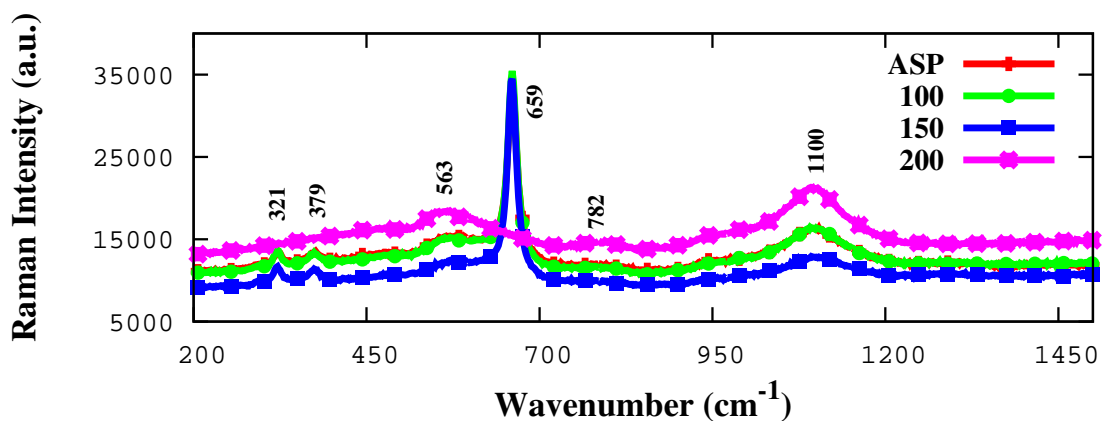
Fig. 4.14: Raman spectrum of Mn-BMZ thin films

able. This shows that there is no molecular decomposition of the material at higher temperatures. Fig. 4.14 shows the Raman spectrum of as prepared and the samples annealed at 100 °C, 150 °C and 200 °C. From the Raman spectrum, peaks at 321, 379 cm^{-1} (correspond to the C-H solid state bonding) and 659 cm^{-1} (corresponds to out plane modes of C-H bond of BMZ) are missing in the samples annealed at 200 ° C. This
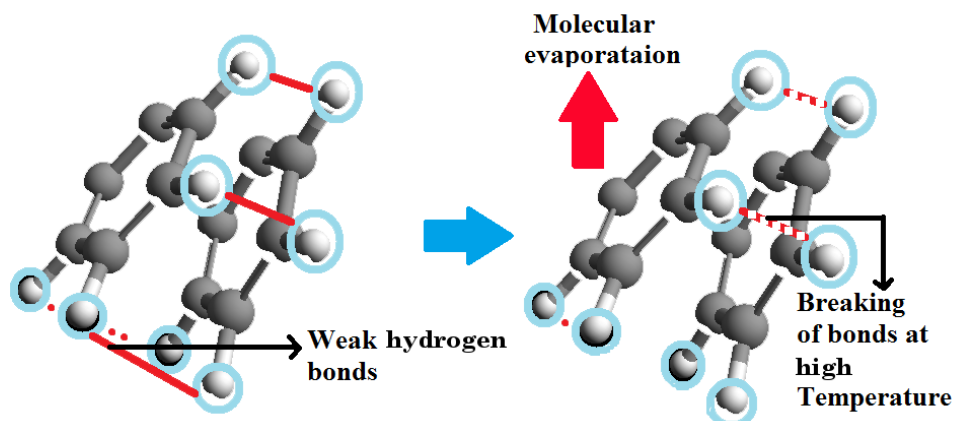
Fig. 4.15: H-bond breaking in the benzene ring of solid BMZ molecule

can be explained by the fact that the organic materials solidify by forming weak hydrogen bonds between the molecules. BMZ is also form such a weak bond by means of four C-H bonds. Due to the breaking of these bonds (Fig. 4.15) distortion of film surface was observed [99].

4.5   Diaceto bis benzimidazole Co(II) and Cu(II) Films

4.5.1   Structural Analysis
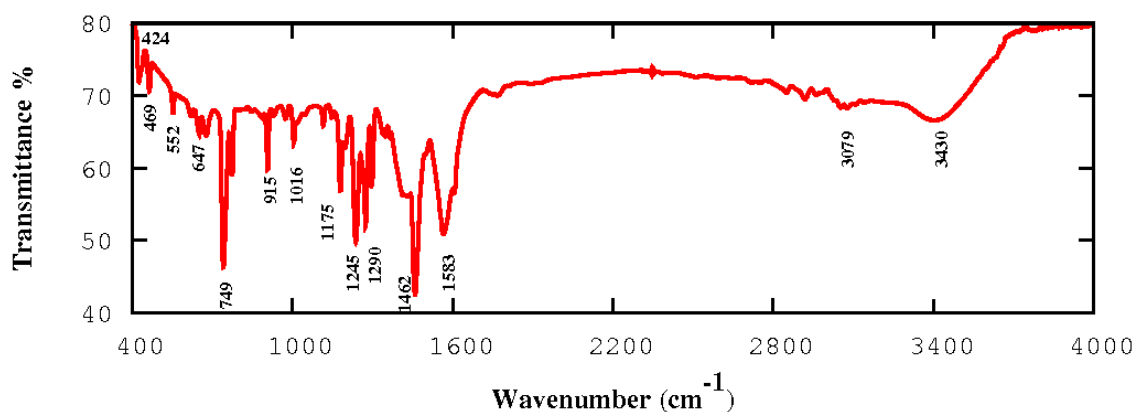
Fig. 4.16: FT-IR spectrum of the Co-BMZ-OAc complex
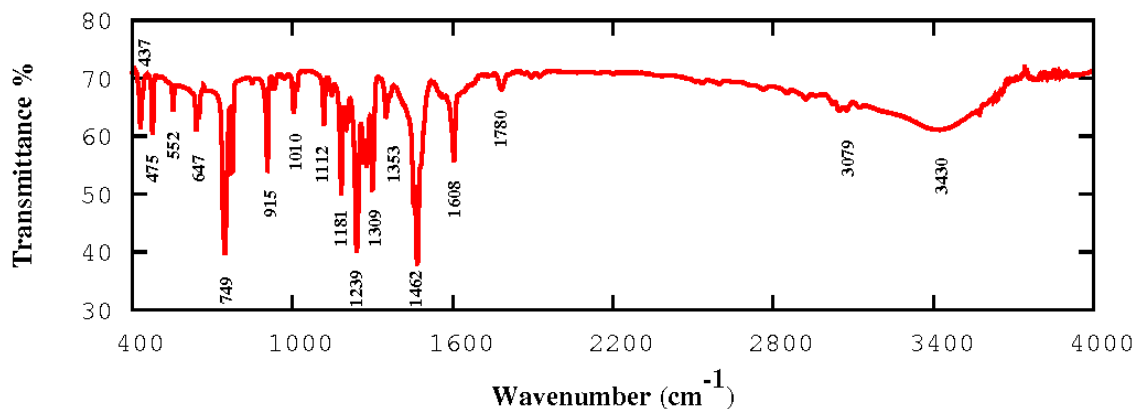
Fig. 4.17: FT-IR spectrum of the Cu-BMZ-OAc complex

Initially Co-BMZ-OAc and Cu-BMZ-OAc materials were synthesized as powders. The molecular structure of the complexes were confirmed prior to their incorporation in PMMA matrices. Figs. 4.16 and 4.17 show the recorded FTIR spectrum of diaceto bis benzimidazole cobalt(II) (Co-BMZ) and diaceto bis benzimidazole copper(II) (Cu-BMZ) complexes, respectively. The peaks observed at 424 cm^{-1} and 437 cm^{-1} in both the spectra corresponds to the metal-ligand vibration in the molecules [100]. Major changes observed in the ring modes of Co-BMZ-OAc and Cu-BMZ-OAc molecules with respect to their parent BMZ ligand could be attributed to the metal-nitrogen interaction. Presence of N-H vibrations at 1016 and 647 cm^{-1} in Co-BMZ, and 1112 and 647 cm^{-1} in Cu-BMZ indicates that the N-H bond of the imidazolate remains unaffected and the metal was coordinated through the molecule by second N atom [90]. Absorption peaks observed in the region 3600 - 2800 cm^{-1} of both the spectra are due to the strong intermolecular hydrogen bonding between BMZ molecules in solid state.

4.5.2   Theoretical Approach

Polymeric systems often consist of hundreds of atoms, and modeling their properties with theories like DFT require considerable computational time. On the other hand,

polymeric systems can be modeled with the help of less accurate classical treatments [108]. With advent of new semiempirical methods such as PM6 and PM7, the feasibility of semiempirical calculations are drastically increased. These modern methods provide better geometries and interaction energies for almost all the elements in the periodic table [109, 110]. Even though, it is possible to perform solid state calculations using semiempirical methods, only a very few attempts were made in that area. In this work, PM6 algorithm in MOPAC2012 package was used to model the solid state interactions between the benzimidazole metal complex and PMMA polymer matrix. Initially the structure of PMMA was drawn using Marvin Sketch package [111] and it was pre-optimized using universal force field (UFF) algorithm available in Avogadro package [112]. Then the molecule was optimized using PM6 method in the MOPAC2012 package [113]. For solid state calculations, MAKPOL program provided with MOPAC2012 was used to construct the polymer chain with 90 monomers. Similarly the Co-BMZ-OAc and Cu-BMZ-OAc metal complexes were pre-optimized using UFF, and the molecular geometry was further optimized using PM6. The obtained structure was embedded into the polymer system in the ratio of 90:1 (PMMA:Metal Organic Complex (MBMZ)) and it was used for simulations. For the energy gap calculation of metal complexes, the auxiliary file of the optimized geometries was loaded in Gabedit program and the highest occupied molecular orbital (HOMO) and the lowest unoccupied molecular orbital (LUMO) were estimated.

4.5.2.1 Interaction Energy Analysis

The objective of the computational analysis is to investigate the interaction between the guest (MBMZ) and host (PMMA) and the corresponding variation in the NLO properties of the entire system. The location of MBMZ molecules in PMMA was visualized using Molden program [114] and the acetate ion in the molecule was taken as the reference point to measure the distance between PMMA monomer and the MBMZ. The

smallest approachable distance between PMMA monomers and the MBMZ is about 34 nm, which is slightly differ from the previous molecular mechanics calculations [108]. This distance does not vary with respect to different MBMZs, since it is an intrinsic property of the polymer system. For interaction energy calculations, the entire system was optimized in two different conditions. One without any separation distance and the second is with a separation distance of about 100 nm, between MBMZ and PMMA matrix. The interaction energy (ΔHf_{IE}) can be calculated using the relation [115],

$$\Delta Hf_{IE} = \Delta Hf_{Complex} - \Delta Hf_{Separate} \qquad (4.2)$$

where, $\Delta Hf_{Complex}$ is the heat of formation of the system without any separation distance and $\Delta Hf_{Separate}$ is the heat of formation of MBMZ and PMMA matrix separated with a distance of 100 nm. The calculated interaction energy between the MBMZ and PMMA matrix using Eqn. 4.2 is given in Table 4.4. It can be seen that the interaction energy increases with respect to the metal ions, and copper complex has more ΔHf_{IE} values than that of the cobalt complex. It is well known that lower the interaction energy higher would be the mobility of the MBMZ inside the polymer matrix when it interacts with an applied field [116]. So, the values given in Table 4.4 can be interpreted as Co-BMZ-OAc is more polarizable or easily polarizable than the Cu-BMZ-OAc complex.

Table 4.4: Interaction energy (Kcal/mol) of MBMZ embedded PMMA samples

Molecule	$\Delta Hf_{Separate}$	$\Delta Hf_{Complex}$	ΔHf_{IE}
Co-BMZ	-247.25	-268.67	21.41
Cu-BMZ	-299.45	-334.50	35.04

4.5.3   Thermo-optical Analysis

Figure 4.18 shows the schematic of experimental setup used to determine the refractive index of PMMA and MBMZ embedded PMMA films at different temperatures (Pristine PMMA (PR), 1,3,5 % Co-BMZ-OAc embedded PMMA (1a, 3a, 5a) and 1,3,5 % Cu-BMZ-OAc embedded PMMA (1b, 3b, 5b)). The polymer film was placed on a silver paste coated substrate and it was mounted on a hot plate. The temperature of the hot plate was adjusted by a temperature controller. The light beam from a diode laser of power 3 mW was passed through a polarizer to the interface between the prism and the glass substrate. The reflected light was detected using a photodiode. The entire setup was placed on a 360° rotating base with a vernier scale and it can be adjusted to the desired angle. It is well known that when a polarized light wave
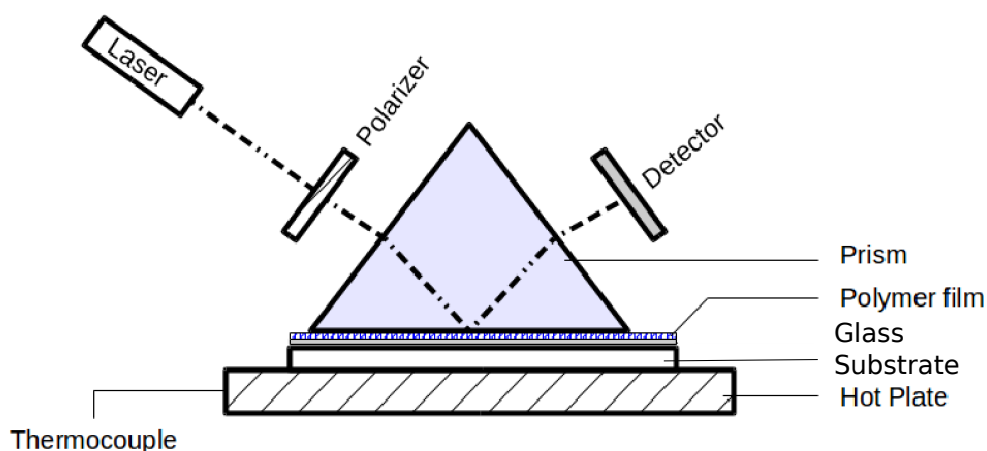
Fig. 4.18: Schematic of experimental arrangement used to measure refractive index of the samples at different temperatures

incident on the interface between two transparent media, the reflected wave would entirely disappears at a particular angle of incidence known as the Brewster angle (θ_B) and the incident wave is totally transmitted into the second medium. By properly adjusting the rotating table, θ_B value can be determined and from that value refractive

index of the polymer sample can be calculated. By measuring the refractive index at different temperatures, the thermo-optic coefficient of the sample can be calculated.

The thermo-optical experiment was performed using a transverse mode polarized laser and the measurements were carried out in the cooling cycle, i.e., from 70 °C to 30 °C at a 5 °C interval for each measurement, inorder to eliminate the possibility of moisture absorption in the samples. Since, the glass transition temperature of PMMA is about 105 °C, a temperature range lesser than that was chosen for the experiment. An additional advantage of opting this temperature range is, that it is the working temperature range for most of the polymeric thermo-optic devices. The thermo-optic coefficient (TOC) of materials in terms of refractive index can be calculated using Prod'homme's theory as [117],

$$\frac{dn}{dT} = \frac{(n^2-1)(n^2+2)}{6n}(\phi - \beta_T) \tag{4.3}$$

where dn/dT is the TOC, n is the refractive index, ϕ is the temperature coefficient of the electronic polarizability and β_T is the thermal expansion coefficient. In the case of polymeric materials ϕ values are much lower than β_T values and TOC entirely depends on β_T. So, the Eqn. 4.3 can be deduced as,

$$\frac{dn}{dT} = -\eta\beta_T \tag{4.4}$$

where,

$$\eta = \frac{(n^2-1)(n^2+2)}{6n} \tag{4.5}$$

According to Lorentz-Lorentz relation for the case of optical polymers, the function $\frac{(n^2-1)}{(n^2+2)}$ is proportional to the specific volume and appears as linear for different temperatures. From which, the thermal expansion coefficient β_T can be directly obtained

as $\beta_T = a/b$ from the phenomenological expression [118],

$$f_{LL} = \frac{n^2 + 2}{n^2 - 1} = aT + b \tag{4.6}$$

where f_{LL} is a function corresponding to the variation of Lorentz-Lorentz relation with respect to temperature and, a and b are the slope and intercept of the linear fit. By substituting the refractive index values measured for different temperatures (Figure 4.19) in the above equation and the corresponding f_{LL} values were calculated and plotted (Figure 4.20). The a and b values were derived from the linear fit of the data in Figure 4.20 and from which the thermal expansion coefficient of the samples was calculated. Further, TOC was calculated by substituting the β_T in Eqn. 4.4 and the calculated values are given in Table 4.5. The TOC values obtained for pristine PMMA sample are in agreement with the previous reports and this ensures the reliability of the experiment [118]. It can be seen that the TOC and β_T values of Co-BMZ-OAc em-
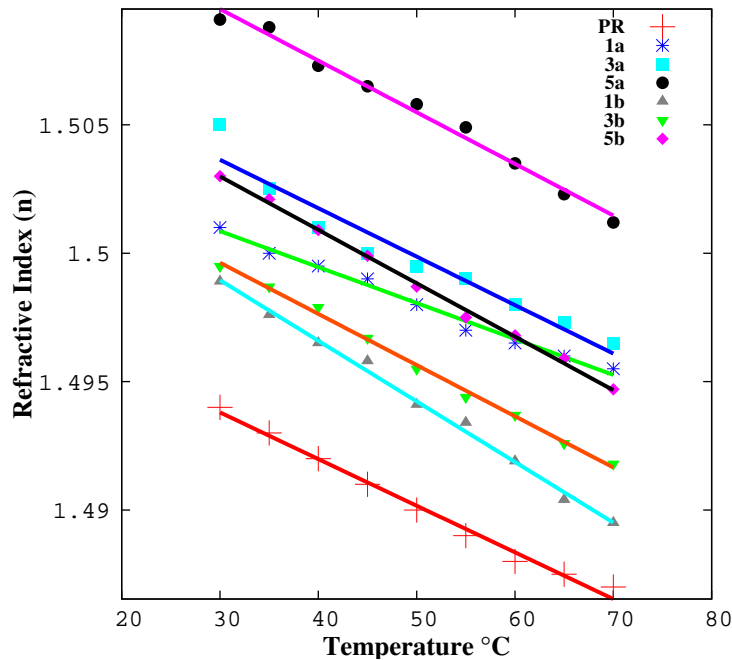
Fig. 4.19: Variation of refractive index of the samples with respect to temperature

bedded PMMA samples increased with increase in Co-BMZ-OAc concentration and in
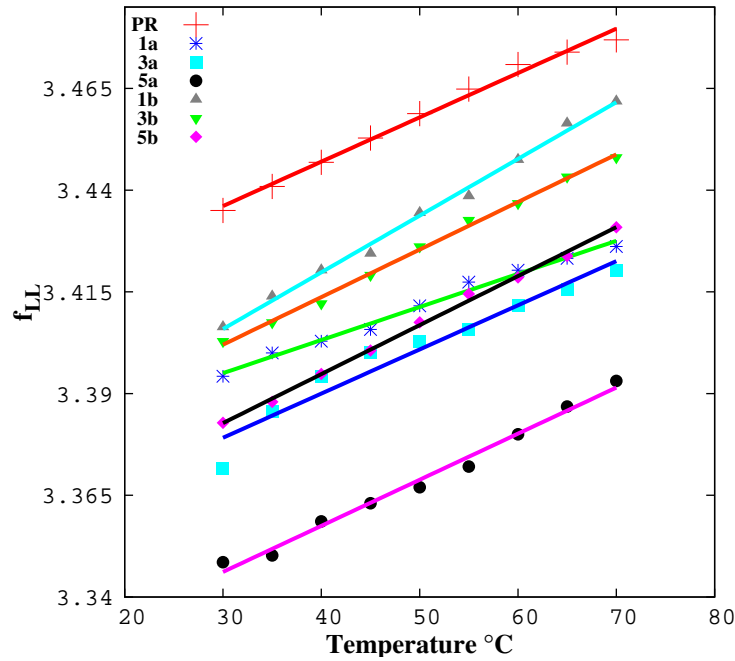
Fig. 4.20: Calculated f_{LL} values with respect to temperature

the case of Cu-BMZ-OAc embedded PMMA samples, the values decreased and then increased. The thermo-optical property of the polymers is influenced by the sum of plasticization and thermal isomerization effects. Depending on the strength of a particular effect, the values of TOC and β_T can vary [118]. In the case of Co-BMZ-OAc embedded samples, due to plasticization effect the thermal expansion coefficient of the samples is increased and a corresponding increase in TOC is observed. Since, the Co-BMZ-OAc s favours the plasticization effect in the host, the β_T values increase with increase in Co-BMZ-OAc concentration. On the other hand, initially, Cu-BMZ-OAc favours thermal isomerization process and it restricts the thermal expansion of the samples. But further increment in concentration enhances the plasticization effect and a corresponding variation is observed. An in-depth investigation is required to analyse the role of different dopants on the plasticization and thermal isomerization effect in polymers.

Table 4.5: Thermo-optical parameters of pristine and MBMZ embedded PMMA samples

Sample	$\beta_T \times (10^{-4})/°C$	η	$\frac{dn}{dT} \times (10^{-4})°C$	f_{LL} of TM
PMMA (PR)	2.411	0.5816	-1.400	T(8.1268×10^{-4}) + 3.4034
1 wt% Co-BMZ-OAc (1a)	3.201	0.5917	-1.816	T(10.8516×10^{-4}) + 3.7065
3 wt% Co-BMZ-OAc (3a)	3.242	0.5974	-1.886	T(10.8951×10^{-4}) + 3.3465
5 wt% Co-BMZ-OAc (5a)	3.419	0.6034	-2.010	T(11.3274×10^{-4}) + 3.3121
1 wt% Cu-BMZ-OAc (1b)	4.140	0.5886	-1.993	T(11.6906×10^{-4}) + 3.3669
3 wt% Cu-BMZ-OAc (3b)	3.472	0.5895	-2.080	T(12.0367×10^{-4}) + 3.3694
5 wt% Cu-BMZ-OAc (5b)	3.596	0.5946	-2.360	T(13.9290×10^{-4}) + 3.3640

4.6 Dichloro bis benzimidazole Co(II) and Cu(II) Nanoparticles

The nanoparticles possess same molecular structure as that of Co-BMZ and Cu-BMZ samples. The DLS measurements were performed to estimate the hydrodynamic size (d(H)) of the colloids. The measured d(H) of both Co-BMZ and Cu-BMZ is shown in Figure 4.21.

It can be seen that the Cu-BMZ particles distributed within the range of 150 nm whereas in the case of Co-BMZ samples, d(H) values are distributed between 100 and 700 nm, as identified from the double peak formation in the region. The double peaks may arise due to either the formation of intermediate products or due to the agglomeration of the particles [119]. In the present case, there is no possibility for the formation of intermediate products, due to the evaporation of alcohols at high temperature and the very less interaction between benzimidazole based metal complexes and water. On the other hand, if there is agglomeration of particles in the solution, with increasing time the dominant peak should move towards the higher particles size area. But, almost same d(H) values were obtained from the repeated DLS measurements over different time periods. So, presence of different size nanoparticles in the case of Co-BMZ may due to the different nucleation process during the spray of precursor solution. An in-depth analysis is required to identify such a process.
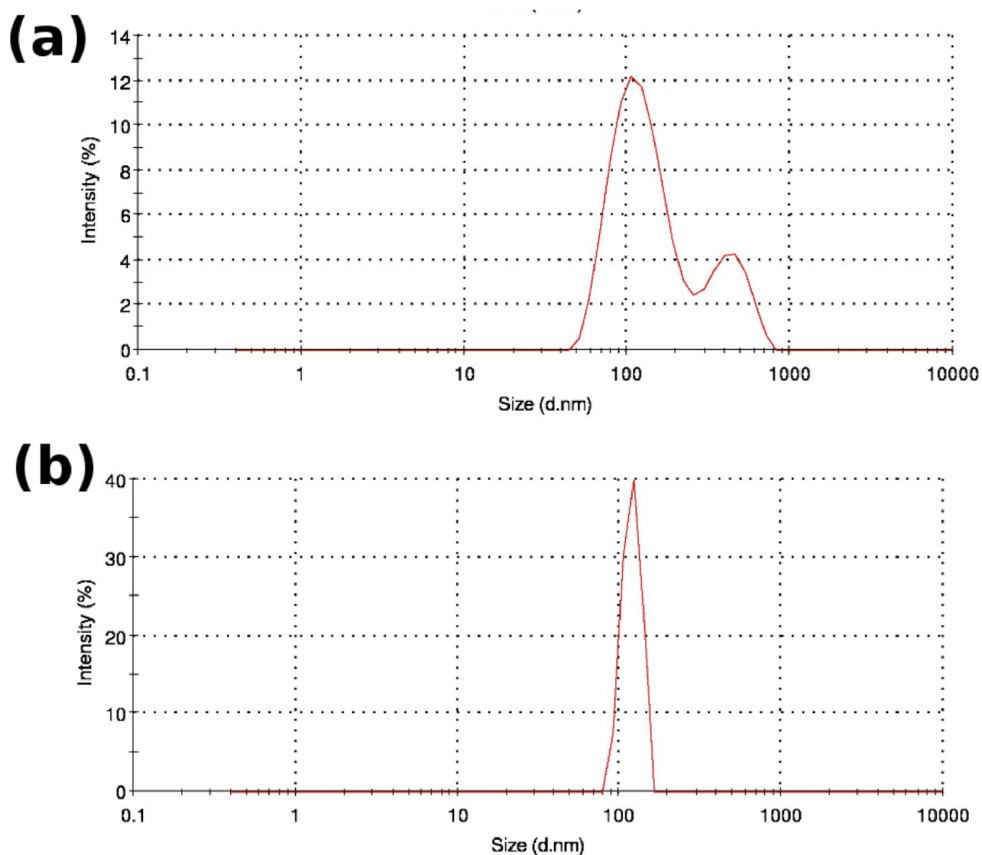
Fig. 4.21: Recorded hydrodynamic size of (a) Co-BMZ and (b) Cu-BMZ nanoparticles

In order to analyse the stability of prepared samples the zeta potential curves were recorded and are shown in Figure 4.22. If zeta potential values are greater than 30 mV or lesser than -30 mV, the samples can be considered as stable [120]. In this work, the obtained zeta potential value of 45 mV for Co-BMZ and 47.7 mV for Cu-BMZ ensures the stability of the prepared nanoparticles in the water medium.

The size and topology of the samples were studied using TEM and the obtained images are shown in Figure 4.23. It is observed that the particle size of Co-BMZ is in the range between 100 and 400 nm, and for Cu-BMZ is in the range of 100 nm. The Cu-BMZ sample seems to be agglomerated and some patches are also visible (Figure 4.23(b)). The Co-BMZ nanoparticles are in cubic shape whereas most of the Cu-BMZ particles are in spheroid shape. If we ignore the hydration shell effect, the
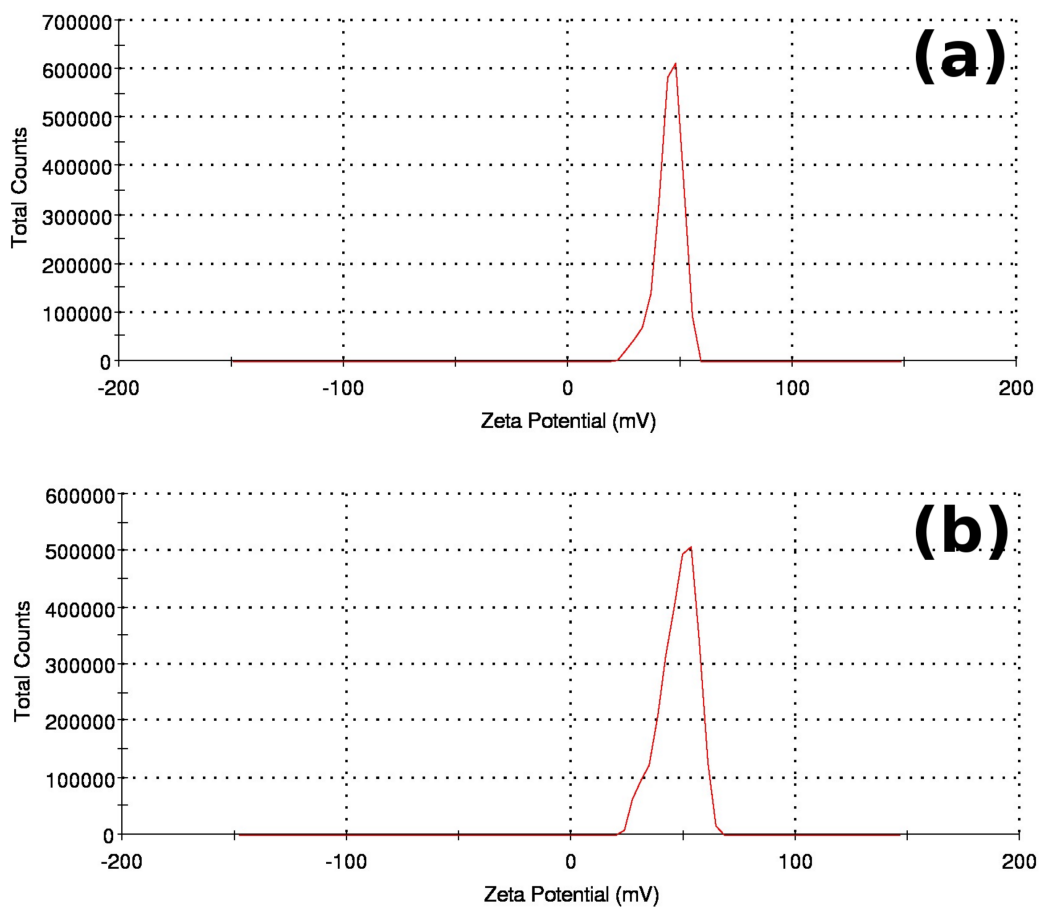
Fig. 4.22: The recorded zeta potential of (a) Co-BMZ and (b) Cu-BMZ nanoparticles
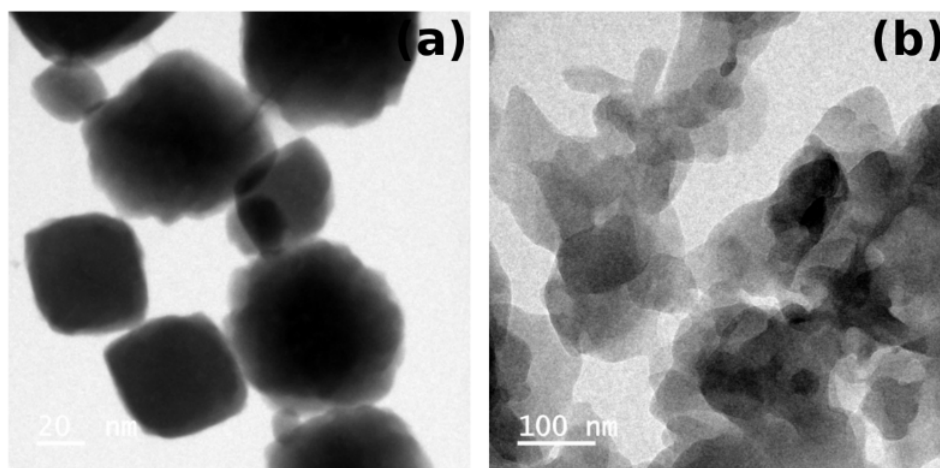
Fig. 4.23: TEM images of (a) Co-BMZ and (b) Cu-BMZ nanoparticles

obtained particle sizes from the TEM images agree well with the DLS measurements.

4.7   Conclusion

Different characterization studies were employed to analyse the structural and surface morphology of the prepared samples. Considering crystallanity all samples exhibit amorphous nature except BMZ thin films. Molecular structure of Co-BMZ, Cu-BMZ, Co-BMZ-OAc, Cu-BMZ-OAc and Mn-BMZ-OAc were studied by FT-IR analysis. Further, EDS, EPR and theoretical simulations were used to confirm the molecular structure of Mn-BMZ sample. Thin film samples were annealed at different temperatures and it is found that the surface topography varies with respect to the annealing temperature. The DLS and TEM analyses reveal the high stability of the nanoparticles with cubic and spheroid morphology.

Linear Optical Properties

5.1 Introduction

The linear optical properties of the samples were studied in two ways. First, the po-larizability, energy gap and dipole moment values of the metal complexes were calcu-lated through computational analysis. Further, the linear absorption properties of the samples were studied using UV-Vis spectroscopy (Perkin Elmer lambda UV-Vis. spec-trometer) in the wavelength range between 300 and 800 nm.

5.2 Dichloro bis benzimidazole Co(II) and Cu(II) Thin films

5.2.1 Computational analysis

From the computational analysis, it is found that the metal complexes possess bet-ter polarizability and hyperpolarizability values than that of the parent BMZ molecule.

The calculated polarizability (α), first order hyperpolarizability (β_{SHG}) and second order hyperpolarizability (γ) values of BMZ and its metal complexes are tabulated in Table 5.1. The results indicate that, even though both the metal ions (Co and Cu) can improve the NLO properties of an organic medium, copper performs better than that of cobalt and shows higher nonlinear effect [121]. The calculated values of HOMO, LUMO and HOMO-LUMO energy gap (E_g) for Co-BMZ and Cu-BMZ molecules are given in Table 5.2. Figure. 5.1 shows the direct participation of metal ion in both the complexes which also confirms the contribution of charge transfer excitations in improving the first and second order hyperpolarizabilities in metalated BMZ when compared with that of BMZ.

Table 5.1: Calculated Polarizability and Hyperpolarizability values of BMZ, Co-BMZ and Cu-BMZ

Material	α (a.u.)	β_{SHG} (esu)	γ (esu)
BMZ	94.67	0.23×10^{-30}	0.3603×10^{-35}
Co-BMZ	368.75	0.44×10^{-24}	22.74×10^{-30}
Cu-BMZ	269.02	8.93×10^{-24}	2168.76×10^{-30}

Table 5.2: Calculated HOMO, LUMO and E_g values in atomic units

Type	Co-BMZ	Cu-BMZ
HOMO	-0.3182	-0.3599
LUMO	-0.0526	-0.0385
E_g [HOMO-LUMO]	0.2655	0.3214

5.2.2   Linear Optical Properties

The linear optical properties of the deposited thin films were analysed by UV-Vis. transmission spectrum (Fig. 5.2 (a) and 5.2 (b)), especially, to study their fundamental transitions and optical homogeneity. The as deposited and annealed Co-BMZ films show a broad absorption band in the region of 550-690 nm. This can be assigned to $^4A_2 \rightarrow\, ^4T_1$ (P) electronic transition [122]. The band observed in this region is the characteristic of
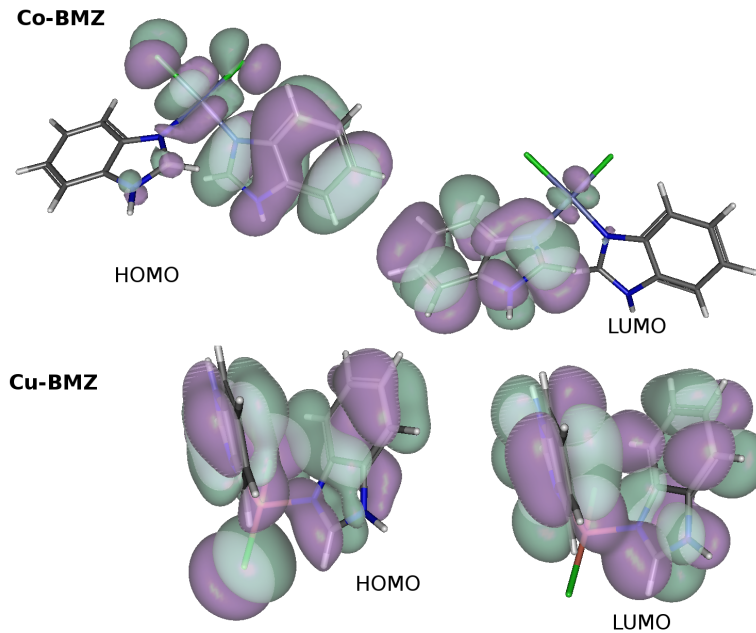
Fig. 5.1: Frontier orbitals of Co-BMZ and Cu-BMZ molecules

tetrahedral structure and arises due to spin-orbit coupling of the T state. Whereas for Cu-BMZ films, small absorption peaks appeared at about 700 nm can be assigned to the $^2B \rightarrow ^2E_-$ transition [123]. Both the complexes exhibit strong absorption between 300 and 400 nm corresponding to intra-ligand transitions. The molar extinction co-efficient (K) values of Co-BMZ and Cu-BMZ films were calculated using the relation $K = \alpha\lambda/4\pi$, and the calculated K values lie between 220 and 350 for all the samples which support the tetrahedral structure of the complexes [124]. Optical scattering loss often reduces the transmittance and the quality of NLO devices. In the present case, the high transparency of both Co-BMZ and Cu-BMZ thin film complexes ensures its optical homogeneity over a broad spectrum and expected to yield better NLO re-sults. The variation in optical transmittance of the samples with respect to annealing temperature can be understood with the help of grain size of the corresponding sam-ples. In the Co-BMZ thin films, the sudden shift in absorption edge may be due to the agglomeration of nano-sized grains to form micro patches. For Cu-BMZ samples an-
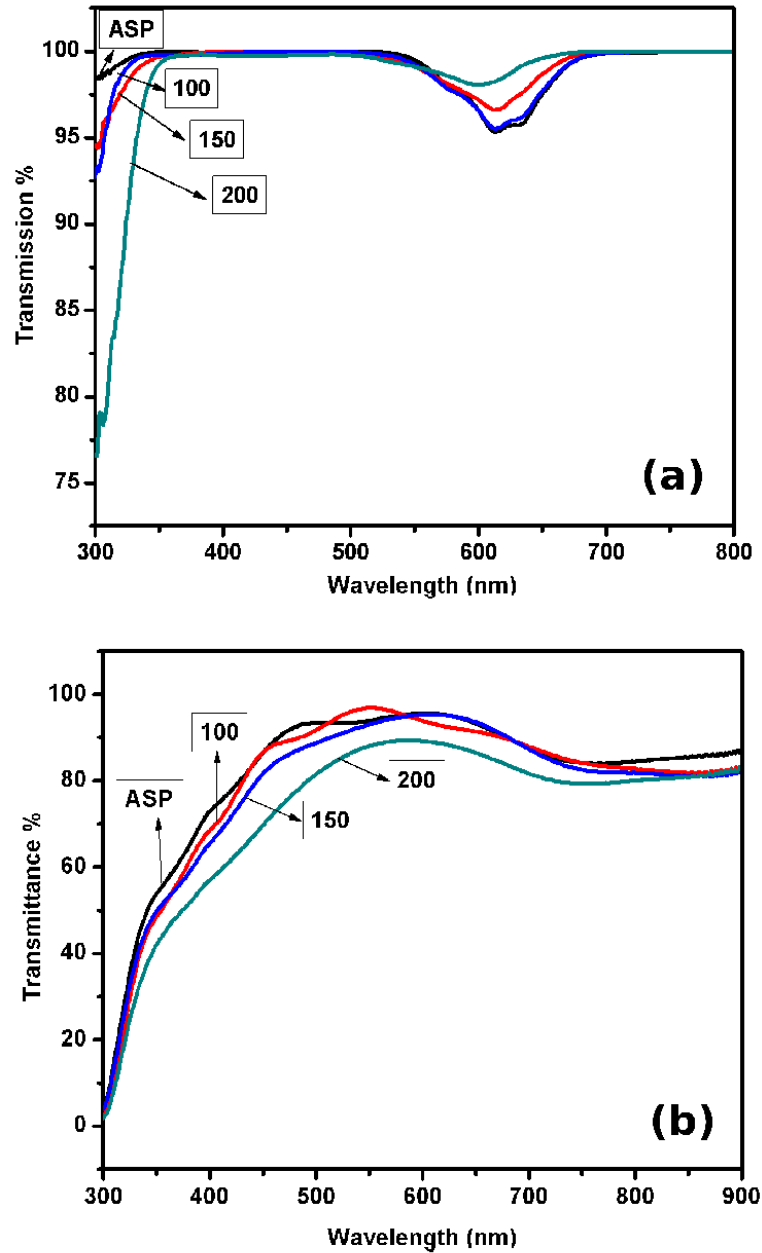
Fig. 5.2: Transmission spectrum of as prepared (a) Co-BMZ and (b) Cu-BMZ samples and annealed at 100 °C, 150 °C and 200 °C

nealed at 200 °C, the grain size rapidly increases which inturn decreases the optical transmittance of the film [125].

5.3   Diaceto bis benzimidazole Mn(II) Thin films

Transmittance spectrum of Mn-BMZ complex thin films was studied by UV-Vis. spectrum analysis and is shown in Fig. 5.3.
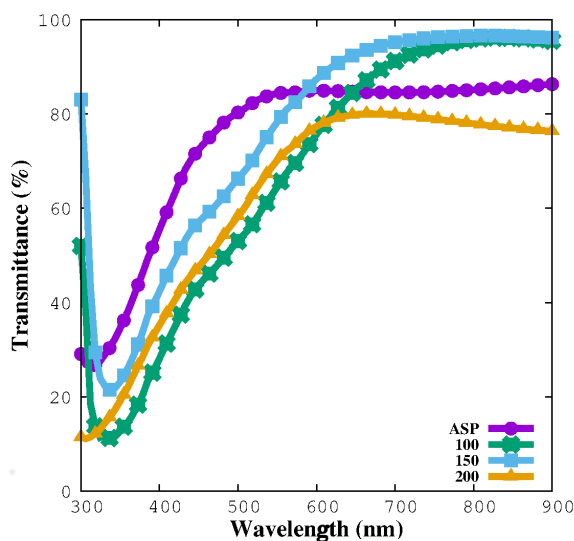
Fig. 5.3: Transmission spectrum of as prepared Mn-BMZ samples and annealed at 100 °C, 150 °C and 200 °C

A broad absorption peak is observed in the region between 300 nm and 500 nm for all the films. At higher wavelength region, the films show high optical transmission about 80% and this ensures the optical homogeneity of the deposited films. The absorption maxima centered around 320-350 nm can be assigned to π-π^* inter-ligand transmissions and the secondary peak observed around 500 nm can be inferred to the metal to ligand charge transfer d$\pi_{(Mn)}$-$\pi^*_{(ligand)}$ transition [102]. The enhancement in transmission percentage of annealed films with respect to their annealing temperature can be interpreted to the variation in grain size. It is well known fact that the transmission percentage of thin films increases with decrease in grain size [126]. A similar phenomena is observed in the case of Mn-BMZ films too. Increase in grain size at 200 °C of annealing temperature results lower transmission in the sample. The red shift in the absorption maxima indicates the possibility of electronic transition in lower

energy region with respect to the decrement in grain size.

5.4   Diaceto bis benzimidazole Co(II) and Cu(II) Films

5.4.1   Computational Analysis

5.4.1.1   Energy Gap Analysis

The frontier orbitals, HOMO and LUMO (Figure. 5.4) are used to calculate the energy gap (E_g) of the molecules and the calculated values are given in Table 5.3. It can be seen that the Co-BMZ complex possess lower energy gap values than Cu-BMZ complex which ensures the reliability of interaction energy calculations.
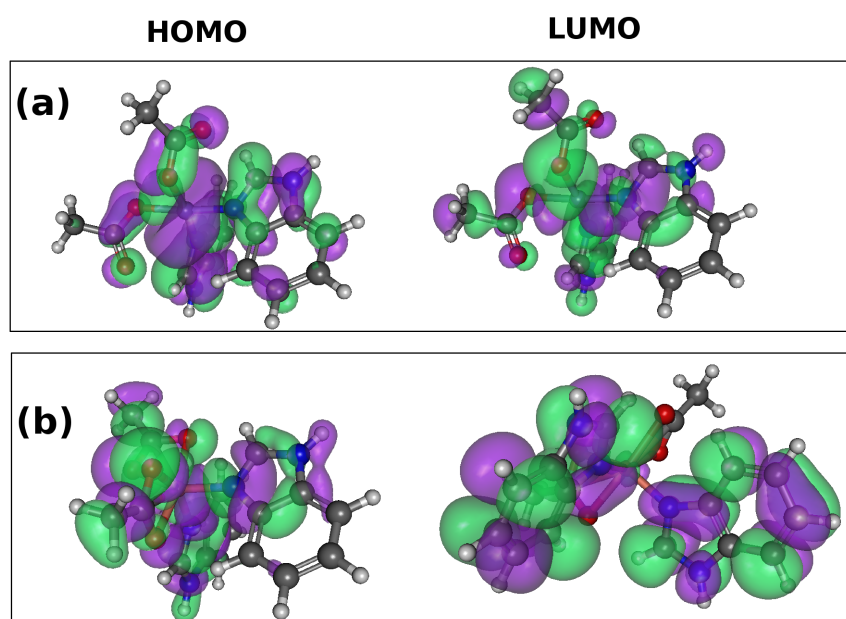
HOMO   **LUMO**

Fig. 5.4: Frontier orbitals of (a) Co-BMZ and (b) Cu-BMZ molecules

Table 5.3: Calculated HOMO, LUMO and E_g values in atomic units

Molecule	HOMO	LUMO	E_g
Co-BMZ	-0.2717	-0.07	0.2016
Cu-BMZ	-0.3037	-0.0155	0.2882

5.4.1.2   Dipole Moments Analysis

Necessity of dipole moments calculations is two fold. First it can be used to estimate the polarizability of a system. Secondly measuring dipole moments with and without the host can be useful to understand the co-operative moments in the system. Considering co-operative moments, when embedding a MBMZ in a polymer matrix of zero optical response, it is expected that the entire observed optical response from the system is the sum of the response from individual 'N' number of MBMZs. So, the dipole moment of the system can be expressed as μ_{total} = Nμ [127]. But at certain instances there is a possibility of co-operative interactions between the MBMZs and monomers, which may enhance the total optical response of the system. In such a scenario, the dipole moment of the system entirely depends on the number of bonded monomer units, and the enhancement in optical response can be attributed to the additional dipole moments arised from the monomers. So in the present work, the average dipole moment of the system was calculated from the MOPAC self-consistent field (SCF) calculation and the calculated values for systems with and without PMMA are given in Table 5.4. Higher dipole moments of Co-BMZ embedded PMMA matrix indicate the potentiality of the system towards optical applications. Further, the variation in dipole moments with and without PMMA suggests that the monomers around the metal complexes are also tend to orient in the direction of applied field and this add up to the dipole moments of the entire system.

Table 5.4: Dipole moments of MBMZ embedded PMMA samples in Kcal/mol

Molecule	X	Y	Z	Sum
Co-BMZ	0.33	7.74	0.44	7.76
Co-BMZ/PMMA	0.95	9.77	0.75	9.85
Cu-BMZ	1.01	3.81	0.19	3.95
Cu-BMZ/PMMA	1.43	5.06	-0.08	5.26

5.4.1.3   Polarizability and Hyperpolarizability Analysis

The efficiency of MBMZ embedded PMMA matrices on the NLO properties was studied by calculating the polarizability (α), first hyperpolarizability (β) and second hyperpolarizability (γ) values. For this purpose, the COSMO (conductor like screening model) calculation was employed, and the electrostatic potential value for PMMA was taken as 2.7 (at 1 MHz). The calculations were carried out for static, 0.25 and 0.5 eV energies and the calculated α, β and γ values are given in Table 5.5. It can be seen that the polarizability and hyperpolarizability values significantly increase with increase in the input energy. This is obvious that more number of molecules tend to align in the applied field direction with increasing field strength. Co-BMZ embedded PMMA system shows better polarizability and hyperpolarizability values than the Cu-BMZ embedded system and the higher values of Co-BMZ embedded PMMA can be interpreted as the contribution of unfilled d-shells in Co-BMZ complex.

Table 5.5: Polarizability and hyperpolarizability values of MBMZ:PMMA system in atomic units

Applied Field	α		β		$\gamma \times 10^3$	
(eV)	Co-BMZ	Cu-BMZ	Co-BMZ	Cu-BMZ	Co-BMZ	Cu-BMZ
0.0	307.71	267.88	1651.03	677.61	2686.95	44.66
0.25	308.22	268.15	1670.98	702.27	4494.56	47.85
0.5	309.77	268.96	1790.39	787.78	4668.25	61.32

5.4.2   Linear Absorption Properties

Figure 5.5 shows the absorption spectrum of the PMMA and MBMZ embedded PMMA samples. Both the complexes exhibit strong absorption between 300 and 400 nm corresponding to intra-ligand transitions [128]. Optical scattering loss in the sample might induce absorption other than molecular absorption. But the very low absorption other than their characteristic molecular absorption in the visible window ensures

the high transparent nature and optical homogeneity of the samples. Minimum absorption at 650 nm is advantageous for nonlinear optical studies, if the operation wavelength of the laser source is in that wavelength. So, one can expect higher order transitions rather than the linear electronic transitions. The variation in optical absorbance of the samples with respect to MBMZ concentration indicates the direct influence of MBMZ in optical properties of the samples. Co-BMZ complex has higher linear absorption than the Cu-BMZ complex. Presence of spin-orbit coupling due to the unfilled d-shells of Co-BMZ (i.e., Cu-BMZ is more planar than the Co-BMZ) complex results more distortion in its tetrahedral geometry and it leads to the higher absorption [129].
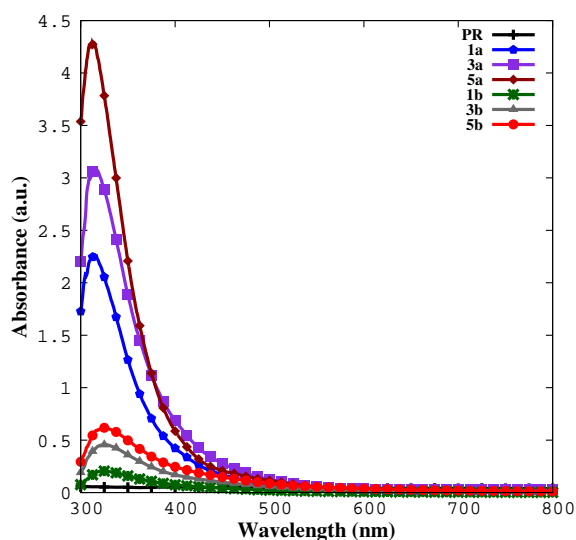
Fig. 5.5: Absorption spectrum of PMMA (PR) and 1 wt % (1a), 3 wt % (3a) and 5 wt % (5a) Co-BMZ and 1 wt % (1b), 3 wt % (3b) and 5 wt % (5b) Cu-BMZ embedded PMMA matrices

5.5   Dichloro bis benzimidazole Co(II) and Cu(II) Nanoparticles

The recorded absorption spectra of the samples are shown in Figure 5.6. Both the samples show good absorption in the region of 650 nm, which is advantageous for

thermo-optical studies performed using a source of same wavelength.
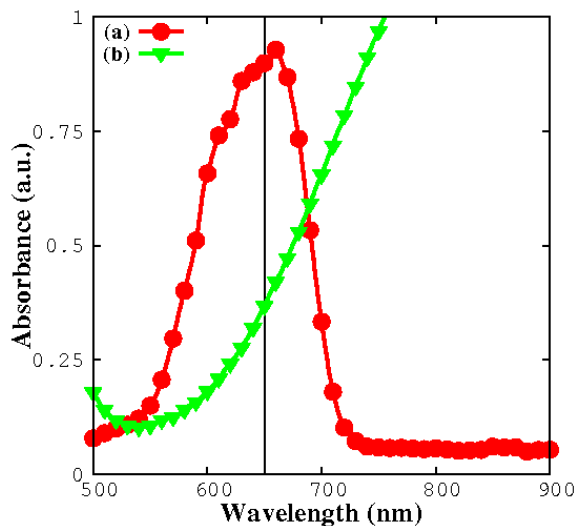
Fig. 5.6: Absorption spectra of (a) Co-BMZ and (b) Cu-BMZ nanoparticles

5.6   Conclusion

The fabricated samples were subjected computational and linear absorption studies. All the samples show good absorption in UV-Vis. region corresponding to $\pi \rightarrow \pi^*$ transitions. Both the linear optical property and computational simulation indicates the potentiality of the complexes towards nonlinear optical applications.

Nonlinear Optical Properties

6.1 Introduction

Thin films of as prepared and annealed at different temperatures were subjected to second harmonic efficiency measurements. Further, all the samples were subjected to study the third order nonlinear optical properties using Z-scan setup. For benchmarking purpose, BMZ films of similar thickness have been used for the measurements.

6.2 Second Harmonic Generation Efficiency

Second harmonic generation (SHG) efficiency of the M-BMZ thin films was measured using a modified Kurtz-Perry method [130] and the schematic of the experimental setup used to measure SHG efficiency is shown in Fig. 6.1. SHG measurements were carried out using a Q-switched Nd:YAG laser (Quanta-Ray DCR-11 Model) of wavelength 1064 nm with operating power of 190 mJ and pulse width of 10 ns. The amplitude of SHG in the films was measured by placing the films normal to the probe
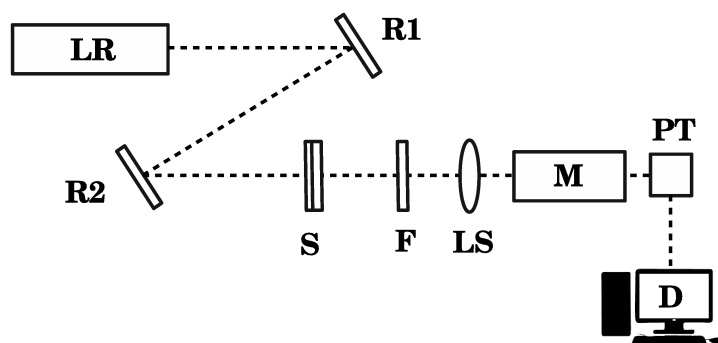
Fig. 6.1: Experimental setup used to measure SHG in M-BMZ samples, LR - Q-switched Nd:YAG laser, R1 and R2 - IR reflectors, S - sample, F - IR filter, LS - focusing lens, M - monochromator, PT - photomultiplier and D - data acquisition system

beam and the second harmonic generation in the samples was confirmed by the observation of green radiation. The output amplitude usually increases with increase in the input energy and it may diminish if some damage occurs to the sample. For most of the cases, upto 25 mJ the output increases with respect to input energy and then it begins to decreases. So, we have chosen 25 mJ as operating laser power for all the SHG measurements. Initially, the beam was allowed to pass between two IR reflectors and then on to the sample. The output from the sample was filtered by using an IR filter and focused on to the monochromator using a focusing lens. Then the output from the monochromator was collected by using a photomultiplier and the data was collected using a computer. Then, the relative SHG efficiency, ratio between BMZ and M-BMZ samples, was calculated using the collected data.

6.2.1   Co-BMZ and Cu-BMZ Films

The relative SHG efficiency calculated for the complexes is given in Table 6.1. Co-BMZ and Cu-BMZ films show respectively 1.3 times and 2.5 times higher SHG efficiency than that of the BMZ films. Annealing upto 150 °C plays a significant role in the improving SHG efficiency of both the metal complex thin films. Further, Cu-BMZ films

show higher relative SHG efficiency than that of Co-BMZ films and the values agree well with the computational results. Optical scattering loss due to surface distortion reduces the SHG efficiency in both the metal complex films annealed at 200 °C.

Table 6.1: Calculated SHG efficiency of Co-BMZ and Cu-BMZ samples

	SHG Efficiency		
Sample	Co-BMZ	Cu-BMZ	Mn-BMZ
ASP	1.31	2.56	2.37
100	1.43	2.72	2.54
150	1.54	2.91	2.67
200	1.32	2.41	2.51

6.2.2   Mn-BMZ Films

The relative SHG efficiency of the Mn-BMZ films was calculated by the ratio between the intensity counts of Mn-BMZ and BMZ thin films of similar thickness and the calculated values are provided in Table 6.1. The variation in SHG efficiency of the Mn-BMZ samples with respect to annealing temperature can be attributed to the variation in surface homogeneity (See Section 4.4.2, Chapter 4). During the deposition of Mn-BMZ thin films, due to the dipolar forces the molecules tend to align in the antiparallel fashion [131]. Upon annealing, molecular orientation aligned and this improves the SHG efficiency in the films. In the case of organic/metal organic materials, major contribution is expected to arise from the molecules rather than their molecular arrangement. This is the reason for only slight reduction in SHG efficieny of the sample annealed at 200 °C with strong surface distortion.

6.3   Third Order Nonlinear Optical Properties

6.3.1   Z-scan Measurements

The third order nonlinear optical properties of the deposited thin films were studied by Z-scan technique at room temperature in open aperture (OA) and closed aperture (CA) configurations [132, 133]. The absorptive and refractive coefficients were used to calculate the magnitude and sign of real and imaginary part of third order nonlinear susceptibility. In the present work, a 20 mW continuous wave (CW) diode laser of wavelength 650 nm was used as the source. A lens of focal length 15 cm was used to focus the beam on the sample and a digital power meter was used to record the variation in output intensity with respect to the sample position (Z). An aperture with linear transmittance of 40% was placed in front of the detector to record the CA scans and it was replaced by a convex lens to record the OA scans. The theoretical relation for transmittance as a function of distance for CA scans can be expressed as [134],

$$T(Z) = 1 - \frac{4.x}{(x^2+9)(x^2+1)}\Delta\Phi_0 - \frac{2(x^3+3)}{(x^2+9)(x^2+1)}\Delta\Psi_0 \qquad (6.1)$$

where $x = Z/Z_0$, $\Delta\Phi_0$ and $\Delta\Psi_0$ is the laser induced phase shift near the focus due to nonlinear refraction and absorption, respectively and the Φ_0 is related to the nonlinear refractive index (n_2) by the equation

$$\Phi_0 = kn_2 I_0 L_{eff} \qquad (6.2)$$

where, $k = (2\pi/\lambda)$, I_0 is the intensity of the laser beam at focus ($z = 0$), L_{eff} is the effective thickness of the sample and it can be calculated using the relation $L_{eff} = \frac{(1-e^{-\alpha_z L})}{\alpha_z}$, here L is the thickness of the films and α_z is the linear absorption coefficient of thin films. Eqn. 6.1 is fitted to the experimental data in order to calculate n_2 values. In

open aperture Z-scan, the absorption coefficient of the films can be related to transmittance using the relation [134],

$$T(Z) = \sum_{m=0}^{\infty} \frac{[-q_0(Z)]^m}{(m+1)^{3/2}} \tag{6.3}$$

where $q_0 = \beta_z I_0 L_{eff}/(1+(Z^2/Z_0^2))$, β_z is the nonlinear absorption (NLA) coefficient, Z_0 is the Rayleigh radius, which could be obtained from the relation $Z_0 = \pi \omega_0^2/\lambda$, where ω_0 is the beam waist and λ is the wavelength of source. The value of q_0 is obtained by fitting the Eqn. 6.3 to the experimental data. The real ($Re\chi^{(3)}$) part and imaginary ($Im\chi^{(3)}$) part of the third order nonlinear susceptibility ($\chi^{(3)}$) was calculated using the relation,

$$Re\chi^{(3)} = 2n^2 \epsilon_0 c n_2 \tag{6.4}$$

and

$$Im\chi^{(3)} = \frac{n^2 \epsilon_0 c \lambda \beta_z}{2\pi} \tag{6.5}$$

where n is the linear refractive index, c is the speed of light in vacuum and ϵ_0 is the permittivity of free space. Further, the absolute value of $\chi^{(3)}$ was calculated from $[(Im\chi^{(3)})^2 + (Re\chi^{(3)})^2]^{1/2}$.

6.3.2   Electronic Transition Mechanism in Z-scan Studies

In metal-organic materials the nonlinear optical process can be explained using a five level model diagram [134]. Fig. 6.2 shows two sets of energy levels S_n and T_n (n=1,2,3...) of a molecule corresponding to the singlet and triplet states respectively. When the sample was irradiated with a laser source, molecules in the ground state (S_0) get excited to the first electronic excited state (S_1), further they can make a transition to the first triplet state (T_1) by intersystem crossing (ISC) and usually the time scale for ISC is about 1 ns. Upon continuous laser irradiation, molecules in S_1 and T_1 can further
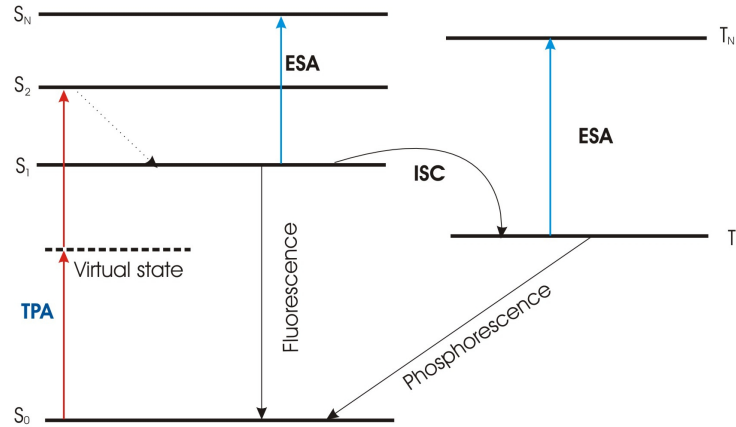
Fig. 6.2: Five level energy model diagram

get excited to S_2 and T_2 respectively. This type of transitions is referred as the excited state absorption (ESA). In low thresholds the transitions will be on nanosecond scale and the triplet-triplet ($T_1 \rightarrow T_2$) transition plays a dominant role in ESA process and ($S_1 \rightarrow S_2$) transition dominates at higher energies with picosecond time scale limits. Also, if ESA has greater excited state absorption cross section (σ_{ex}) than that of the ground state absorption cross section (σ_0) RSA takes place. On the other hand, if σ_0 is greater than σ_{ex}, saturable absorption (SA) will be observed. Depending upon the type of nonlinear absorption either a peak or valley corresponding to SA and RSA can be observed in OA Z-scan curves. There might be a possibility of two photon absorption (TPA) present in the samples, its contribution would further decrease the optical transition. Considering nonlinear refraction, the physical origin of the effect could be electronic, molecular, electrostatic or thermal in nature. But, excluding thermal effects, other three are highly intensity dependent and it is very less likely to be observed in the CW regime.

6.3.3   Co-BMZ and Cu-BMZ Thin films

In the third order nonlinear optical studies, the effective length (L_{eff}) of the samples varies between 3.39x10^{-7} and 6.32x10^{-7} m. Laser beam waist was calculated as 2.5 μm and the corresponding nonlinear absorption coefficient of Co-BMZ and Cu-BMZ films is in the order of 5.1 - 5.6x10^{-2} m/W and 8.5 - 9.2x10^{-2} m/W, respectively. The nonlinear absorptive and refractive coefficient values calculated from the experimental data are given in Table 6.2. In open aperture scan, the transmittance falls to a minimum at focus (z=0) for both the metalated BMZ complexes (Fig. 6.3 (a) and 6.3 (b)), thus indicating the nonlinear behaviour is due to reverse saturable absorption (RSA). Even though, the two photon absorption (TPA) can cause similar decrement in transmission at focus, there is only very lesser chance for TPA in a CW regime and the large Z-scan signal indicates the contribution of thermal effects in the samples. Observation of RSA in Co-BMZ and Cu-BMZ films suggests that the ESA has greater excited state absorption cross section than that of the ground state absorption cross section and $T_1 \rightarrow T_2$ transition might dominate the RSA process due to the participation of metal ions in the electronic transition. Further, the nonlinear absorption of the samples varies with grain size of the samples. For Co-BMZ samples the nonlinear absorption increases with decreasing grain size whereas for Cu-BMZ films, it increases with increasing grain size. The reason for continuous increment of β_z in Cu-BMZ films may be due to the optical scattering losses, which reduces the intensity of the output beam. Since there is no way to elucidate the amount of the light scattered by a particular sample, the corresponding change in the intensity is considered as nonlinear absorption effect.

The closed aperture plots of both the complexes imitate the open aperture Z-scan. To extract the nonlinear refractive effects, closed aperture data was divided by open aperture data and the corresponding graphs are shown in Fig. 6.4 (a) and 6.4 (b) res-
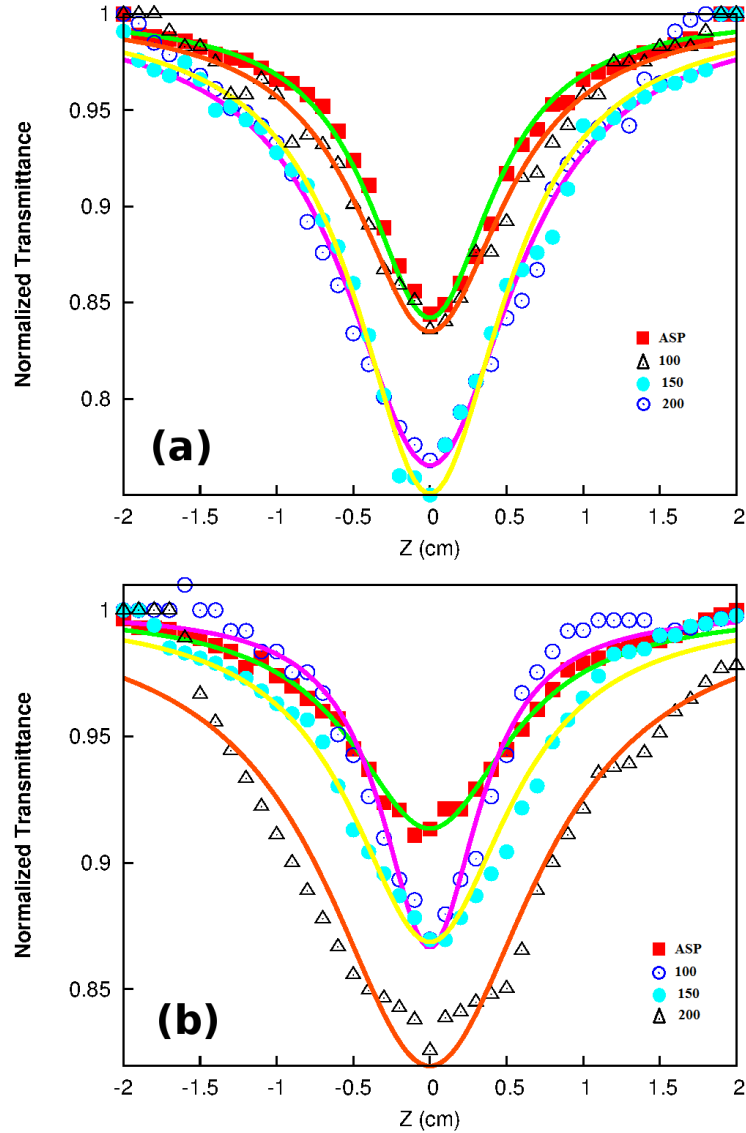
Fig. 6.3: Open aperture Z-scan curves of (a) Co-BMZ and (b) Cu-BMZ thin films

Table 6.2: Calculated nonlinear absorptive and nonlinear refractive coefficients of Co-BMZ and Cu-BMZ thin films from Z-Scan

Sample	$\beta_z(10^{-2}$ m/W)		n_2 (10^{-7} m^2/W)	
	Co-BMZ	Cu-BMZ	Co-BMZ	Cu-BMZ
ASP	5.1	8.5	3.76	-3.00
100	5.2	8.8	11.98	-3.74
150	5.4	9.1	12.59	-3.21
200	5.6	9.2	9.81	-14.78

pectively. It can be seen that the Co-BMZ films show a valley-peak (V-P) type curve and Cu-BMZ films show a peak-valley (P-V) type curve. This corresponds to the self defocussing and focusing nature of the thin films, respectively. Results of the present work given in Table 6.2 reveal that the refractive nonlinear effect is comparatively weaker than the absorptive effects. The nonlinear refractive index of the Cu-BMZ films is found to be negative and hence they can be considered as thin negative lens. On the other hand self focusing effect is observed in Co-BMZ films. In CW regime, thermal effect dominates over other phenomena and variation in nonlinear refractive index of both the complexes can be attributed to thermal nonlinearity. In the case of Cu-BMZ films, laser heating in absorbing medium, induces a spatial distribution of temperature over the region and this inturn alters the laser beam passing through it. Thus the variation of refractive index is observed due to the strong phase distortion of the propagating beam. Whereas, in Co-BMZ films the observed change in the sign of nonlinear refractive index is due to the variation in excited state population which causes a change in hyperpolarizability of the molecule. High excited state population in the case of Co-BMZ can be attributed to charge-transfer band around 600 nm (see section 5.2.2, in chapter 5) [135]. Also, the variation in nonlinear refractive index of the samples with respect to annealing temperature can be attributed to the variation in surface homogeneity and grain size of the samples. The nonlinear refractive index of the Co-BMZ films increases with decrease in grain size. Due to the lower grain size values, the optical scattering loss in the medium is reduced and hence the film annealed at 200 °C shows high nonlinear refractive index than that of the ASP sample. In Cu-BMZ film, higher grain size yields high negative nonlinearity. But the variation in n_2 for the samples annealed at 100 °C and 150 °C may be due to the surface homogeneity and it can be understood from the kurtosis value of the corresponding samples. The third order nonlinear susceptibility of the complex films (given in Table 6.3) is in

the order of 10^{-6} esu. Since the films possess different thickness due to annealing, figure of merit (FOM) for all the samples was calculated by dividing $\chi^{(3)}$ value by their corresponding linear absorption coefficient (α_z) [133]. From Table 6.3, it is observed that the Cu-BMZ film possesses high nonlinear optical susceptibility than that of the Co-BMZ films.
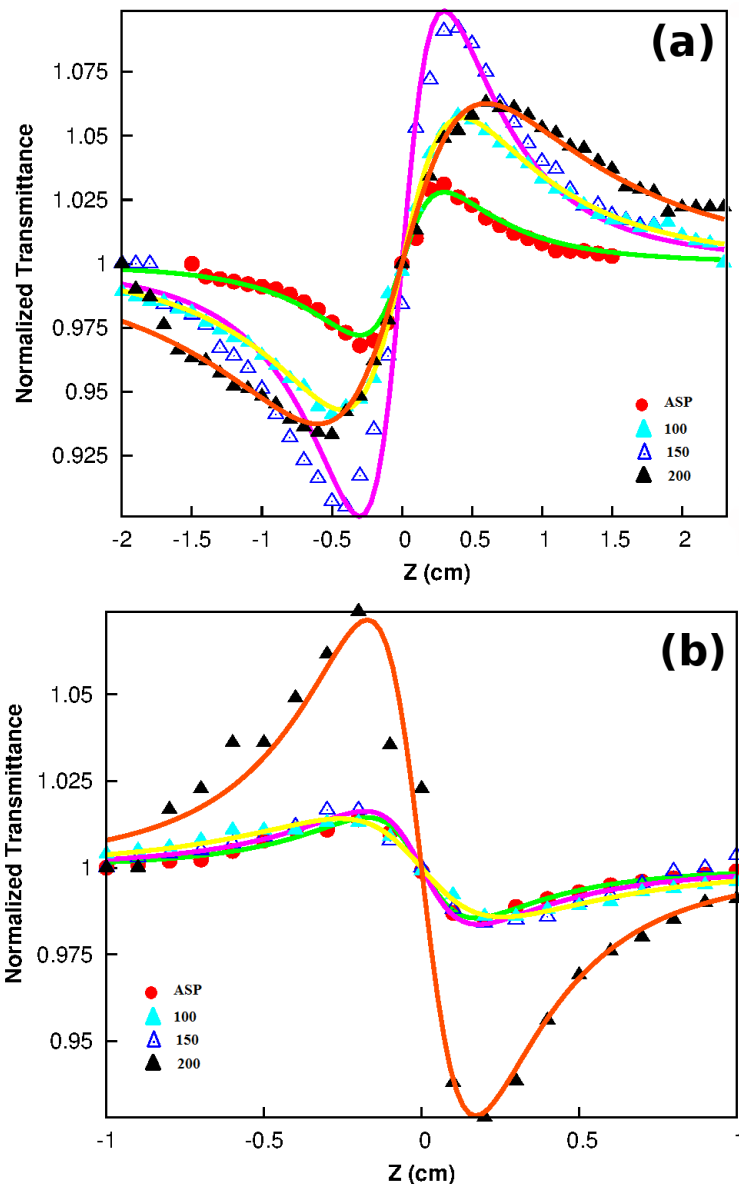
Fig. 6.4: Closed aperture Z-scan curves of (a) Co-BMZ and (b) Cu-BMZ thin films

Table 6.3: Calculated third order nonlinear optical parameters of Co-BMZ and Cu-BMZ thin films from Z-Scan measurements

Sample	$\text{Im}\chi^{(3)}$ (10^{-6} esu)		$Re\chi^{(3)}$ (10^{-7} esu)		$\chi^{(3)}$ (10^{-6}) esu		FOM (10^{-13} esu)	
	Co-BMZ	Cu-BMZ	Co-BMZ	Cu-BMZ	Co-BMZ	Cu-BMZ	Co-BMZ	Cu-BMZ
ASP	0.46	9.09	2.23	-5.70	0.68	9.66	0.48	16.15
100	0.49	9.29	6.48	-6.90	1.13	9.98	0.31	21.92
150	0.52	9.32	7.73	-6.07	1.29	9.92	0.94	21.72
200	0.59	9.63	4.19	-7.61	1.00	10.39	0.62	9.94

6.3.4   Mn-BMZ Films

The nonlinear absorptive effects of the Mn-BMZ samples were studied using open aperture Z-scan curves (Fig. 6.5). All the films, show saturable absorption (SA) behaviour whereas the film annealed 200 °C shows reverse saturable absorption (RSA) character-istics. The observation of SA in Mn-BMZ films suggests that the ESA has lower excited state absorption cross section than that of the ground state absorption cross section and $S_1 \rightarrow S_2$ transition process might dominate in the electronic transitions. The CA curves imitate the OA curves and CA curves were divided by OA data in order to get pure nonlinear refractive effects. Since the CW laser is used as the source, origin of nonlinear refractivity can be attributed to thermal effects [136]. The calculated values of third order nonlinear optical properties of Mn-BMZ films are given in Table 6.4.

Table 6.4: Third order nonlinear optical properties of Mn-BMZ films

Sample	β_z (m/W)	$n_2 \times 10^{-7}$ (m^2/W)	$\chi^{(3)} \times 10^{-9}$ esu	FOM $\times 10^{-14}$ esu
ASP	-0.41	-1.57	2.77	1.10
100	-0.52	-1.60	3.00	1.17
150	-1.95	-2.16	3.93	1.47
200	1.22	5.40	1.64	0.30

The origin of observed third order nonlinearities is due to thermal effects. When the CW laser beam traversed through the sample, it has been absorbed by the sam-ple by linear absorption. Often, absorption of high energy beam creates a heating
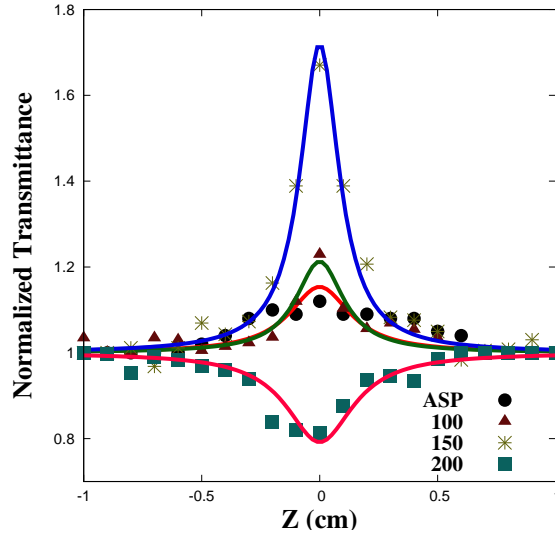
Fig. 6.5: OA Z-scan curves of Mn-BMZ films
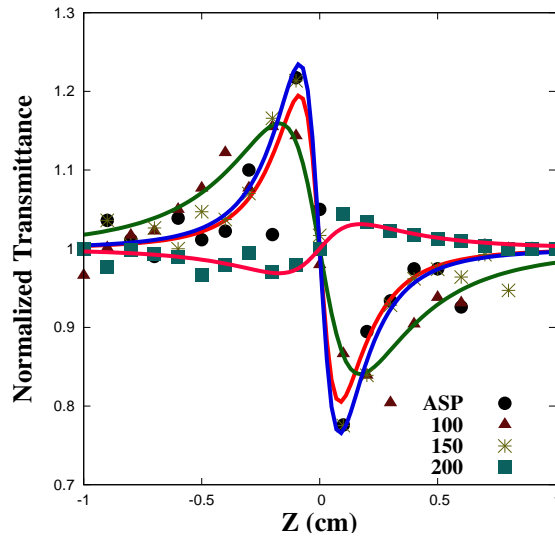
Fig. 6.6: CA Z-scan curves of Mn-BMZ films

effect in the medium, which induces a local thermal gradient. Induction of thermal gradient alters the refractivity of the medium, which acts as lens, known as thermal lens. Further propagation of the beam through this lens alter the phase of the propagating beam and thus induces the nonlinear effects. In Z-scan analysis, it is well established that the peak-valley separation in CA scan about 1.7 times of Rayleigh range indicates Kerr-type nonlinearity. More than that could be attributed to the thermal

effects [137]. Since, the peak-valley separation in our case is around 2.8 times of Z_0, supports the discussion above. In order to estimate the potentiality of the different Mn-BMZ samples, figure of merit (FOM) was calculated using the relation χ^3/α [133]. Higher the FOM, higher would be the sample's third order optical nonlinearity. With better linear transmittance and higher nonlinear absorption coefficient, sample annealed at 150 °C shows higher FOM (Table 6.4).

6.3.4.1   Role of Surface Morphology on Optical Properties

The variation in optical properties with respect to the surface morphology (especially the sample annealed at 200 °C) can be explained in terms of molecular deformation process. In any metal organic thin films, the molecular packing in a layer can be expressed in terms of rotation (θ) and bending (ϕ) angles of a molecule in that particular plane. Upon annealing, due to thermal diffusion, the molecules tend to reorient themselves (i.e., θ and ϕ values changes). During such a process, two phenomenon will take place. The dislocation densities of the sample will be reduced and depending upon the molecular weight, deformation of molecules with respect to annealing temperature will takes place [138]. These variations can significantly affects the physical properties, in particular, the optical properties [139]. In the case of Mn-BMZ films, the strong molecular deformations at 200 °C of annealing temperature can cause the unfilled d-valence orbital, formed due to the interaction between π electrons of the ligand and d-shell electrons of the metal ion, to split into several levels. This in turn will increase the optical absorption in the samples. It is worth to note that higher the grain size, lower would be the coherence between the molecular networks [140]. This explains the variation of optical properties of the sample, annealed at 200 °C, with respect to its (increased) grain size. On the other hand, since the SHG efficiency of the samples entirely depends on the d-shell of the Mn ion in the molecular structure, only slight variation in SHG efficiency with respect to surface scattering has been observed,

similar to the effects observed in porphyrine and phthalocyanine molecules [141]. But, in order to precisely explore the surface dynamics, combined experimental and theoretical studies such as scanning tunneling microscope analysis and density functional theory/molecular dynamics simulations are required and may be performed in future.

The observed switch over phenomena from SA to RSA and self defocussing to self focusing in the sample annealed at 200 °C can be accounted to the variation in input intensity with respect to the reflectivity of the samples. Switch over phenomena are often observed with pulsed laser sources and two or three photon absorption could be the possible mechanism for such a behavior. It is rare to observe a switch over phenomena with a CW pump since it is not possible to produce an intensity of about 10^8 W/cm^2 using a CW laser, which is the minimum requirement to observe the above mentioned effects. Even the available reports on switch over behavior in a CW regime, mainly studied in a solution form or doped in polymers and the effect is attributed to the aggregation particles in the solution/polymer, with respect to their concentration [142]. But, in our case the variation in the input intensity with respect to the surface morphology can be attributed to the observed effect. Because, in nonlinear optical materials, switch over from one phenomenon to other phenomenon can arise if the input intensity crosses the threshold value, say I$_c$. So, by varying the input intensity on the sample one could vary the nonlinear optical phenomena. In the Z-scan experiment, the intensity of the light traversed through the sample can varies by means two factors: (i) depending on the position of the sample with respect to the focusing lens and (ii) by the amount of surface reflections on the sample. Higher the reflectivity of the sample, lower would be the light traversed through the sample. In the case of high reflectance samples like Mn-BMZ, variation in surface morphology would alters the reflectivity of the sample. Decrease in reflectance (Figure. 6.7) for the samples annealed at 200 ° C, should increase the input intensity which crosses above I$_c$,
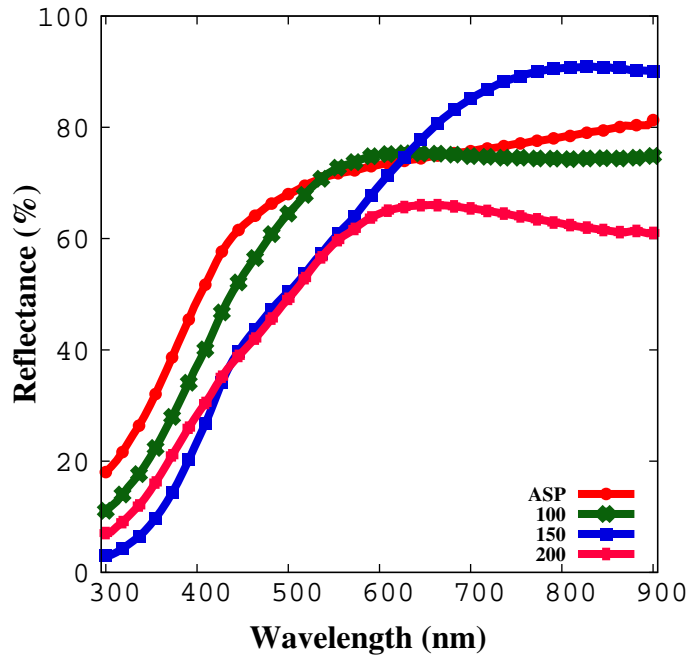
Fig. 6.7: Reflectance spectrum of Mn-BMZ samples

results the observed switch over phenomena, similar to the report by Chen Dai-Jian et al [143]. This is possible in the case of organometallics and polymers even in the CW regime since the saturation intensities are very low for these systems (about 10^4 W/cm^2) [142].

6.3.5 Co-BMZ-OAc and Cu-BMZ-OAc Films

Figures 6.8 and 6.9 show the open and closed aperture Z-scan curves obtained for free standing PMMA films, respectively. All the films were found to exhibit a valley-peak configuration corresponding to positive nonlinearity (i.e. self-focusing) in closed aperture scans. Reverse saturable absorption (RSA) behaviour of the films was observed from the open aperture (OA) scans.

For MBMZ embedded PMMA films, the major contribution were arise due to thermal effects. i.e. the energy of the focused light beam on the sample would induce a heating in the medium and creates a thermal gradient. This thermal gradient would
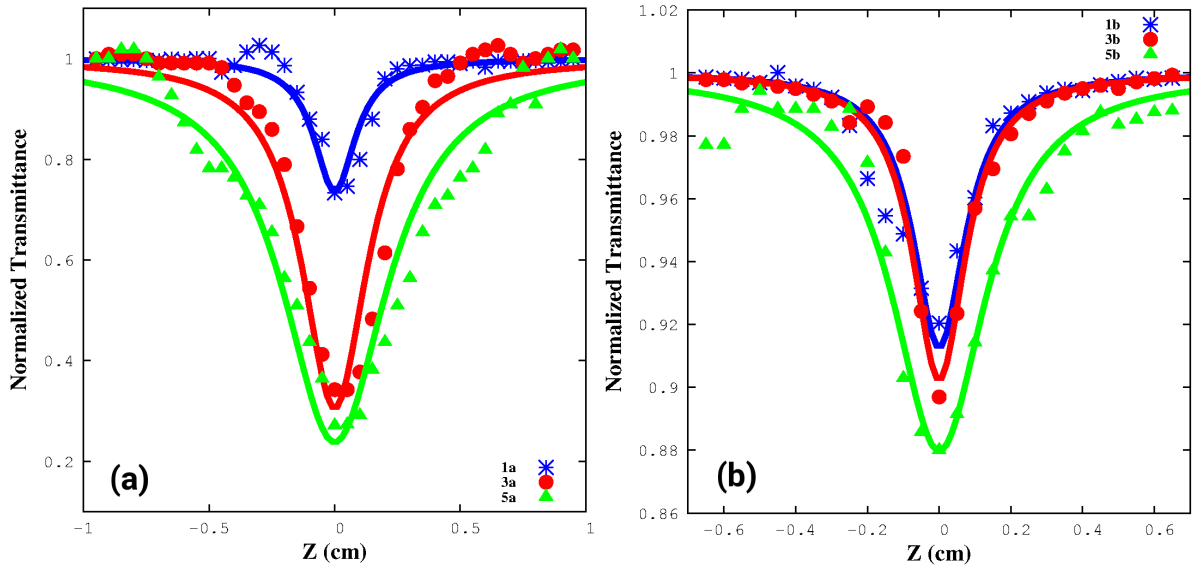
Fig. 6.8: Open aperture Z-scan curves of (a) Co-BMZ-OAc and (b) Cu-BMZ-OAc embedded PMMA free standing films
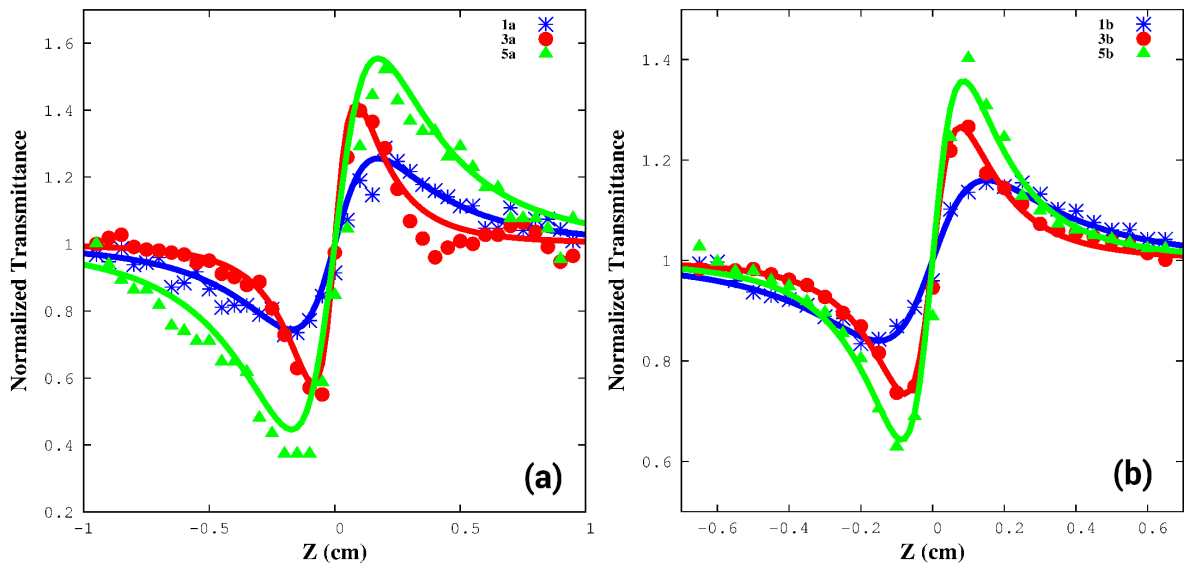
Fig. 6.9: Closed aperture Z-scan curves of Co-BMZ-OAc and Cu-BMZ-OAc embedded PMMA samples

induce refractive index change in the sample that acts as a thermal lens and it distorts the phase of the propagating beam through it [135]. This is one of the common phenomena observed in CW Z-scan studies.The calculated nonlinear optical parameters are listed in Table 6.5. The order of magnitude of $\chi^{(3)}$ is about 10^{-5} esu. Also, the imaginary part of $\chi^{(3)}$ is significantly larger than the real part, means that the nonlin-

Table 6.5: Third order nonlinear optical parameters of MBMZ embedded PMMA samples

Sample	β_z (m/W)	$n_2 \times 10^{-7}$ (m^2/W)	$\chi^{(3)}$ $\times 10^{-5}$ (esu)	FOM
1a	1.20	3.42	14.96	7.65
3a	3.19	4.59	26.34	7.93
5a	3.55	2.14	23.54	8.25
1b	0.39	1.31	5.56	3.24
3b	0.45	2.23	9.01	3.61
5b	0.54	2.94	11.81	3.83

ear absorption is the dominant mechanism in the samples. The β_z, n_2 and $\chi^{(3)}$ values are increased with increase in MBMZ concentration. This can be interpreted as the direct influence of MBMZs in third order nonlinear optical properties of the MBMZ embedded PMMA samples. The figure of merit for polymeric systems can be calculated using the relation $W = \Delta.n/\alpha_z\lambda$ and for a device quality sample it is essential to achieve $|W| >> 1$ [134]. For MBMZ embedded PMMA films, the FOM values (Table 6.5) satisfy the above condition and ensures the versatility of the samples towards optical applications.

6.3.6   Co-BMZ and Cu-BMZ Nanoparticles

Laser induced nonlinear absorptive behaviour of the samples were studied using Z-scan method. To study the effect of different incident intensities on the nonlinear absorption of the samples, different laser intensities such as 1, 3 and 5 mW were used. The obtained curves are shown in Fig. 6.10.

It can be seen that all samples exhibit a saturable absorption and the absorption intensity increases with increase in the input intensity. Interaction of CW laser with matter often induces thermal effect, that can affect the optical property of the medium. Such a phenomenon is called thermo-optical nonlinearity. In the present case, optical nonlinearity was used as a parameter to estimate thermal effects in the medium. i.e.,
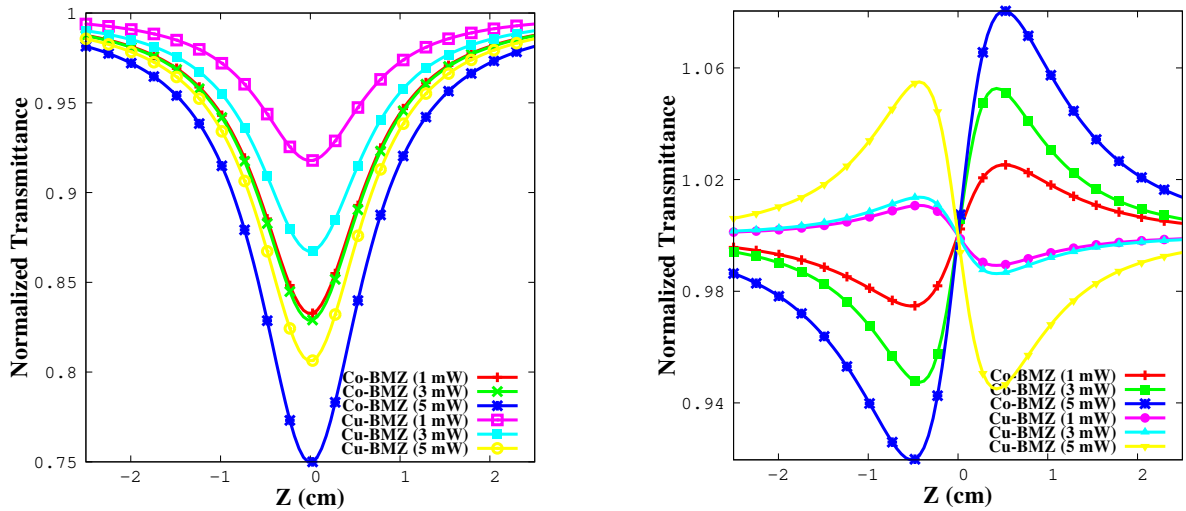
Fig. 6.10: Open aperture (left) and Closed aperture (right) Z-scan of Co-BMZ and Cu-BMZ nanoparticles

higher the thermo-optical effect, higher would be the photothermal effect [144, 145]. So, laser induced thermo-optical behavior of the samples were studied using Z-scan method. In OA scans (Fig. 6.10), the transmittance falls to minimum at focal point (Z=0) indicates the presence of reverse saturable absorption (RSA) in the samples. Presence of RSA curves in both the cases, can be taken as the evidence that the samples possess higher excited state absorption cross section than the ground state absorption cross section. It is advantageous in the sense that unlike SA (in which material absorption tends to bleach at higher intensities), absorption in RSA materials increases with increase in laser intensity and induces a higher thermo-optical nonlinearity [146].

In CA scans, the Co-BMZ samples exhibit self-defocussing whereas the Cu-BMZ samples exhibit self-focusing phenomena. In CW regime thermal effects dominate over other mechanisms and the observed curves can be attributed to thermo-optical nonlinearity. In the present case, locally induced thermal gradient alters the refractive index of the Cu-BMZ samples, but the reversal of CA curves was observed in Co-BMZ samples, due to the high excited state population. The nonlinear absorptive and refractive coefficients extracted by fitting the experimental data were used to calculate the third order nonlinear susceptibility of the samples and is given in Table 6.6.

Table 6.6: Nonlinear optical parameters of Co-BMZ and Cu-BMZ nanoparticles

Sample	Input intensity	β_z (m/W)	$n_2 \times 10^{-6}$ (m^2/W)	$\chi^{(3)} \times 10^{-6}$ (esu)
Co-BMZ	1 mW	1.00	2.74	7.61
	3 mW	1.03	5.71	1.00
	5 mW	1.50	8.72	1.51
Cu-BMZ	1 mW	0.49	-1.16	3.63
	3 mW	0.79	-1.48	5.67
	5 mW	1.16	-5.96	1.09

It can be seen that the calculated susceptibility value increases with increase in input intensity, indicates that the thermo-optical behavior increases with increase in input intensity. Also, the higher values of nonlinear absorption coefficients reveal that the major nonlinear optical phenomena occur due to nonlinear absorption rather than nonlinear refraction.

6.4   Conclusion

The fabricated nanostructures were studied for SHG efficiency and third order susceptibility which are crucial from the applications point of view. The relative SHG efficiency of the prepared Co-BMZ and Cu-BMZ complex films is higher than that of parent BMZ ligand. The result on Z-scan measurements reveals that the nonlinear absorption coefficients of the Co-BMZ films is increased from 0.051 to 0.056 m/W and Cu-BMZ from 0.085 to 0.092 m/W due to the surface defects. Low n_2 values suggest that the domination of nonlinear absorptive effects in the samples at 650 nm of CW laser regime. Third order nonlinear susceptibility of both (Co-BMZ and Cu-BMZ) the samples are in the range of 10^{-6} esu and the films annealed at 150 °C acquire better FOM than the other as prepared and annealed samples. The third order nonlinear studies of Mn-BMZ thin films of ASP sample and the samples annealed at 100 °C and 150 °C show a self-defocussing effect (CA curves) and saturable absorption (OA curves) in

the Z-Scan analysis. But the film annealed at 200 °C shows an switch over phenomena from SA to RSA in OA curves and defocussing to focusing in CA curves due to the variation in input intensity with respect to the surface defects. The calculated third order nonlinear susceptibility of the Mn-BMZ samples was ~ 1.64 to 3.93 $\times 10^{-9}$ esu and the films annealed at 150 °C showed better FOM than the as prepared and other annealed samples. The MBMZ embedded PMMA free standing films showed thermal induced self-focusing and reverse saturable effect in the third order nonlinear optical studies. The third order susceptibility of the free standing films were in the order of 10^{-5} esu. The high figure of merit of the samples ensures the potentiality of the Co-BMZ-OAc and Cu-BMZ-OAc embedded PMMA films for optical limiting applications. In the case of nanoparticles nonlinear absorptive studies indicate that the particles have good saturable absorption at 650 nm region. The SA value increases with increase in laser power corresponds to the higher thermal effects.

Applications

7.1 Introduction

All the fabricated samples are demonstrated to have some nonlinear optical applications. Samples with high RSA behaviour (Co-BMZ, Cu-BMZ, Co-BMZ-OAc and Cu-BMZ-OAc films) are shown to have good optical limiting property. Further, Mn-BMZ films are demonstrated to have optical switching ability. The thermo-optic nature of the samples are utilized for photodynamic therapy to treat cancerous cells.

7.2 Optical Limiting Studies

Materials with good third order nonlinear optical susceptibility can be used as optical limiters. Optical limiters (OL) are the devices, which are transparent for the weak intense light, but get opaque for high intense light. Optical limiting can be achieved by nonlinear optical process, either by nonlinear refraction or by nonlinear absorption. The experimental arrangement used to carry out the optical limiting studies is similar

to the Z-scan setup except a slight modification, such that a polarizer is placed in front of the sample in order to chop the input intensity on the sample [147].

7.2.1 Co-BMZ and Cu-BMZ Thin Films

The Co-BMZ and Cu-BMZ thin films possess strong RSA phenomenon over the nonlinear refraction and they could be investigated for passive OL device applications [148]. The obtained OL results are shown in Fig. 7.1 (a) and 7.1 (b). It can be seen that the output intensity decreases with increase in input intensity. The OL studies show that the films annealed at 200 °C exhibit better limiting behaviour than the other samples due to optical scattering loss. As we discussed in the previous chapter, the output intensity is nothing but remaining light energy that escaped from RSA and optical scattering losses while traversing through the sample. So, sample with higher optical scattering loss would show lower output intensity than the other samples. This is the reason why materials annealed at 200 °C show higher OL effect.

7.2.2 Co-BMZ-OAc and Cu-BMZ-OAc Films

Figure 7.2 shows the optical limiting behaviour of the MBMZ embedded PMMA films. At low input powers, the output intensity increases linearly with it. But at higher irradiance the nonlinear medium starts to limit the output intensity and it clamps at certain power. The limiting ability of the sample increases with increasing M-BMZ concentration. Of the two MBMZ complexes Co-BMZ-OAc embedded PMMA samples show better limiting behaviour than the Cu-BMZ-OAc embedded samples. This can be interpreted with the help of OA Z-scan curves. Due to the high nonlinear absorption in the samples a better OL is achieved.
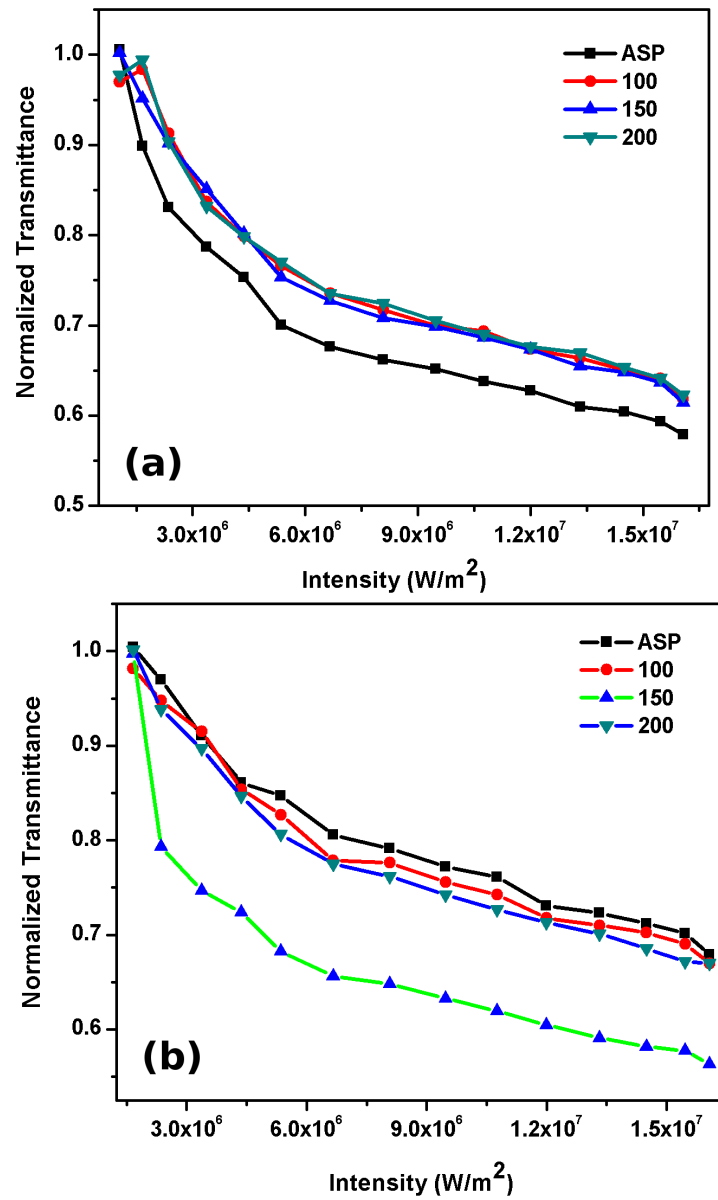
Fig. 7.1: Optical limiting behaviour of (a) Co-BMZ and (b)Cu-BMZ samples
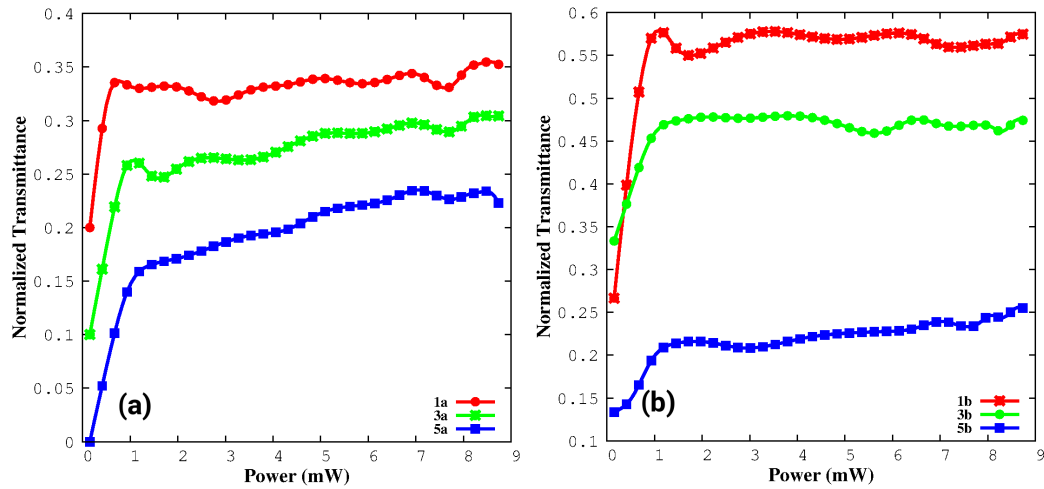
Fig. 7.2: OL studies of 1,3,5 - wt% MBMZ embedded PMMA samples (a) Co-BMZ-OAc and (b) Cu-BMZ-OAc

7.3   Optical Switching

The thermal assisted nonlinear phenomena can be effectively utilized for optical switching applications. The inverted switching (NOT gate) behavior of Mn-BMZ films annealed at 150 °C was studied. The principle is that the population dynamics of the sample
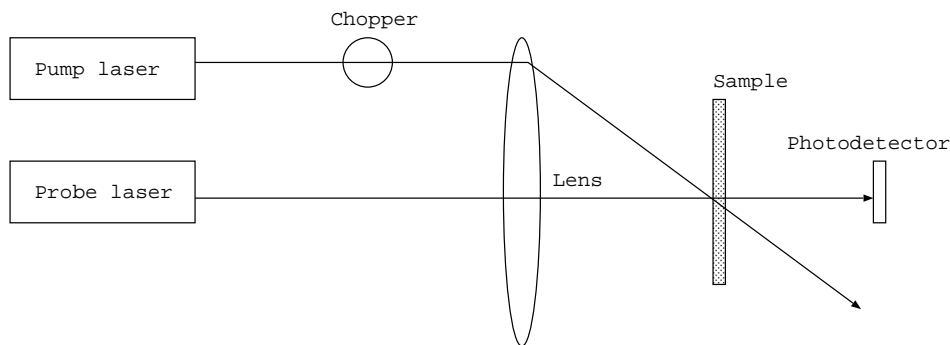
Fig. 7.3: Schematic of an optical switching setup

vary with respect to the intensity of the incident laser, i.e., a high power laser can produce a strong heating effect in a nonlinear medium than a low power laser and the corresponding variation in the excitation dynamics can alter the nonlinear effects [149]. Figure 7.3 shows the schematic of an optical switching experimental setup. A CW diode laser of power 20 mW was used as the pump (writing) beam and a weak

laser of power 1 mW was used as the probe (reading) beam. Both the lasers were operated at the wavelength of 650 nm. Since the sample possesses very low absorption in the 650 nm region, any observed variation can be attributed to the effect of thermal nonlinearity. The pump beam was passed through a mechanical chopper in order to obtain a square wave pattern (ON/OFF state). A lens of focal length 6 cm was used to focus the beams on the sample and the variation in probe beam with respect to the pump beam was measured using an oscilloscope. The obtained traces are shown in Fig. 7.4. By properly adjusting the revolutions per minute (RPM) of the mechanical chopper, a frequency variation upto 1 kHz can be achieved. When the pump beam is in OFF state, the low power probe beam does not induce much effect in the nonlinear medium and it transmits through the sample as it is. But when the pump beam is in ON state, the intensity of the beam induces the thermal assisted nonlinear effects in the medium which leads to the saturation of population in the excited state and correspondingly a low state was obtained as output. This corresponds to the inverted switching behavior of NOT gate, analogous to electronics.
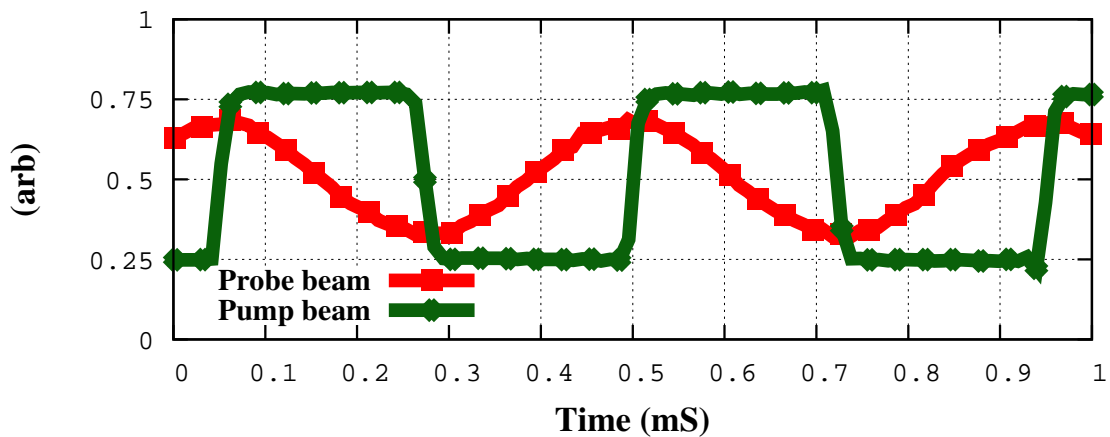
Fig. 7.4: Demonstration of optical inverter switching behaviour of Mn-BMZ film annealed at 150 °C

7.4   Photodynamic Therapy

7.4.1   Materials and Methods

7.4.1.1   Cell Culture

The human lung cancer cell line (A549) and mouse embryonic fibroblast cell lines (NIH-3T3) were obtained from the National Center for Cell Science (NCCS), Pune, India. The cells were cultured in DMEM high glucose medium (Sigma-Aldrich, USA) supplemented with 10% fetal bovine serum (Gibco), and 20 ml of penicillin/streptomycin as antibiotics (Gibco), in a culture flask at 37 °C in a humidified atmosphere of 5% CO_2 in a CO_2 incubator (Thermo scientific, USA). All the culture experiments were performed in cells from passage 15 or less.

7.4.1.2   Cell Viability Assay

To study the cytotoxic effect of Cu-BMZ and Co-BMZ complexes against both cell types, the nanoparticles were dissolved in 100% dimethyl sulfoxide (DMSO) and diluted to obtain a final concentration of 0.02%. In order to study the phototoxic effect of laser (against the cells) the cells were treated with different laser powers, between 1 and 5 mW for 4 mins and the corresponding cell death was analysed using MTT assay. A 96 well plate with 5×10^3 cells per well was used for the experiment. DMSO was used as the solvent control. After the addition of nanoparticles to the plate, the cells were irradiated with laser light (Power=5 mW) at 25 °C for 4 mins and then the plates were incubated for 24 hrs at 37°C. The same procedure was followed without light irradiation to determine the effect of laser induced cell death. After 24 hrs of incubation, 20 μl of MTT solution (5mg/mL in PBS) was added and the plates were wrapped with aluminum foil and incubated for 4 hrs at 37 °C. The produced purple formazan product was dissolved by addition of 100 μL of DMSO and the absorbance was recorded

at 570 nm (measurement) and 630 nm (reference) using a 96-well plate reader (Bio-Rad, iMark, USA). Data collected from the three replicates were used to calculate the respective mean, and the percentage of cell viability was calculated using the formula [150]:

$$\frac{\text{Mean of absorbance of untreated cells (Control)} - \text{Mean of absorbance of treated cells}}{\text{Mean of absorbance of untreated cells (Control)}} \times 100$$

$$(7.1)$$

7.4.2   Morphological Observations

Light Microscopic Study and acridine orange (AO) and ethidium bromide (EB) staining: Induction of apoptosis by metal organic nanoparticles was investigated by AO/EB double staining method as described by Spector et al. with some modifications [151]. Briefly, sub-confluent monolayer culture of A549 and NIH-3T3 cells was trypsinized and 5×10^5 cells/ml were seeded into 6 well plate containing cover slip. The cells were treated with IC_{50} concentration of nanoparticles irradiated for 4 mins and incubated for 24 hrs. After the incubation period, 25 μL of AO/EB solution (3.8 μM of AO and 2.5 μM of EB in PBS) was added on to the cover slip and examined immediately under fluorescent microscope (Carl Zeiss, Axioscope2plus) with UV filter (450–490 nm). The cells treated with nanoparticles were also subjected directly under the light microscopy (Carl Zeiss, Axioscope2plus) for cytological changes.

7.4.3   Docking Methods

Autodock version 4.2.5.1 and Auto Dock Tools (ADT) version 1.5.6 were used for the docking calculations. The ALK protein was obtained from RSC's protein data bank (ID: 2XP2) and the co-crystallized ligand (criztinib) was removed prior to the input file preparation. Polar hydrogens and Gasteiger charges were added and the incomplete side chains were removed using ADT. Then the structure was saved in PDBQT

format in order to use it as autodock input. The ligands were drawn using MarvinSketch and saved in MOL format. The structure was further optimized using UFF algorithm in Avogadro package and saved as MOP format for geometry optimization using MOPAC2012 package. The optimized structure was evaluated by vibrational analysis and the obtained all-positive vibrational peaks ensure the stability of the structure. This was then converted into PDB file using Avogadro and then to PDBQT using ADT for autodock analysis. The grid box for calculations was constructed using the grid size of about $40 \times 40 \times 40$ A^3 with 0.375 spacing. The box was centered at 29.47, 47.99 and 8.86, which is around the binding site of crizotinb in ALK receptor. For docking genetic algorithm was used with default set of parameters and 50 docked conformations were generated for each ligand.

7.4.4 Results and Discussion

7.4.4.1 Cytotoxicity Analysis

The effect of laser power on the cancerous (A549) and normal (NIH-3T3) cells was studied by irradiation of different laser powers, from 1 to 5 mW, for 4 mins and the corresponding cell death was analysed using MTT assay. NIH/3T3 cells show minimal effect for all the three laser powers (1,3 and 5 mW), on the other hand A549 percentage of cell death increases with increase in input laser power and is shown in Figure 7.5. It is a well known fact that the physical stability of the cancerous cells are much lower than the normal cells. On the other hand, a 5 mW CW laser profile contains lower energy which often create lower destruction to the normal cells [152]. So, the destruction of cancer cells alone by laser irradiation is advantageous for targeted therapy.

In order to study the cytotoxic effect of nanoparticles against the cancerous and non-cancerous cells, both the cell lines were treated with nanoparticles. Further, the cell lines were exposed to laser of power 5 mW for 4 mins to evaluate the effect of
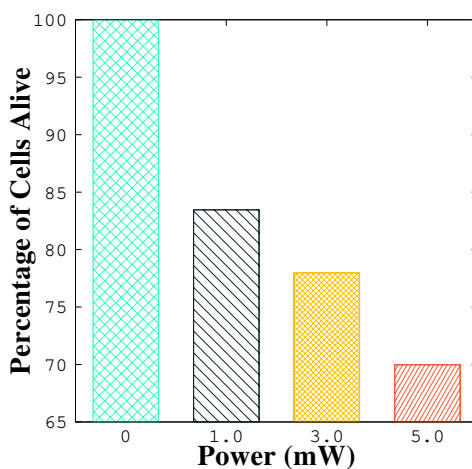
Fig. 7.5: Laser power vs the percentage of cells (A549) alive after irradiation

Table 7.1: In vitro cytotoxicity assays for the complex against human lung cancer cell line (A549) and mouse embryonic fibroblast cell line (NIH/3T3)

Compound	IC_{50} values (μg/ml)	
	A549	NIH/3T3
Co-BMZ	109 ± 0.05	147 ± 0.05
Co-BMZ (laser treated)	86 ± 0.05	132 ± 0.05
Cu-BMZ	95 ± 0.05	178 ± 0.05
Cu-BMZ (laser treated)	60 ± 0.05	165 ± 0.05
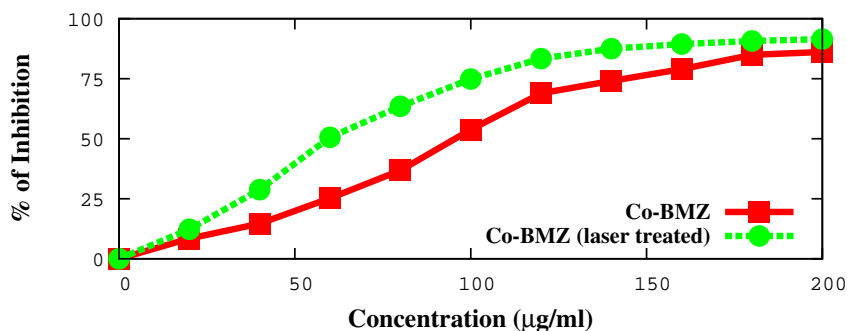
Fig. 7.6: In Vitro cytotoxicity assays for Co-BMZ complex against human lung cancer cell line A549

laser treatment. From which the IC_{50} values are extracted and given in Table 7.1. Also, in vitro cytotoxic assays of the cell lines A549 and NIH/3T3 are shown in Figures 7.6–7.9 and they clearly depict that the cells irradiated with laser light exhibit higher toxicity than the non-irradiated cells. The IC_{50} values revealed that the cancerous cells
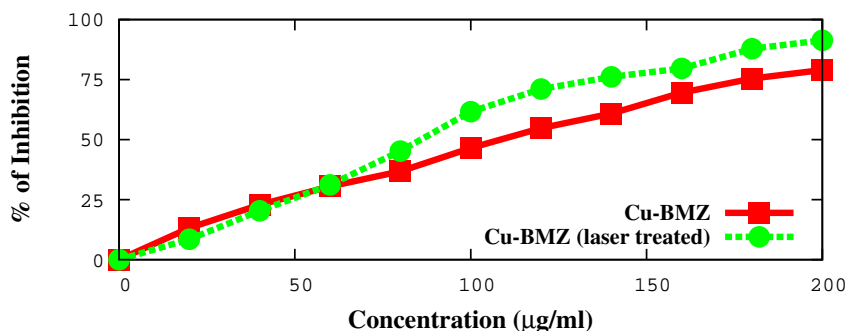
Fig. 7.7: In Vitro cytotoxicity assays for Cu-BMZ complex against human lung cancer cell line A549
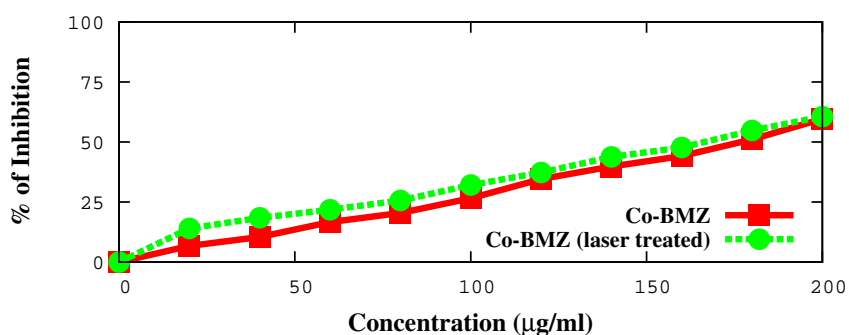
Fig. 7.8: In Vitro cytotoxicity assays for Co-BMZ complex against mouse embryonic fibroblast cell lines NIH-3T3
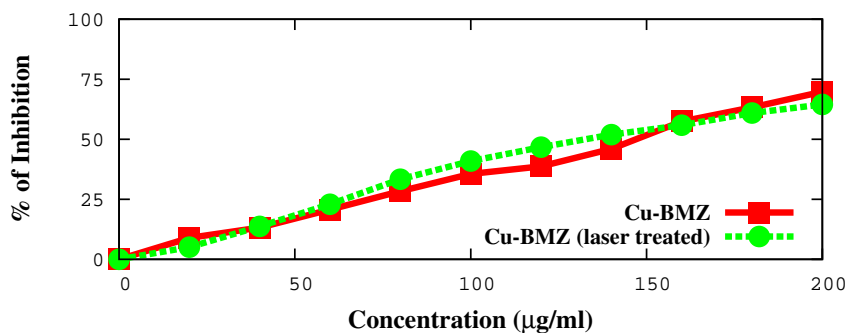
Fig. 7.9: In Vitro cytotoxicity assays for Cu-BMZ complex against mouse embryonic fibroblast cell lines NIH-3T3

were destructed much than the normal cells in the same treatment conditions. Further, the obtained IC_{50} values of A549 cell lines indicates that Cu-BMZ nanoparticles show better anticancer/PDT activity than the Co-BMZ-OAc nanoparticles due to their smaller particle size.

7.4.4.2 Morphological Analysis

Fluorescent microscopic study (Fig. 7.10) of AO/EB double-stained A549 human lung cancer cell line treated with Co-BMZ and Cu-BMZ nanoparticles for 24 hrs shows that the laser treatment induces majority of cell death through apoptosis and very fewer by necrosis. In the case of apoptosis, the cells underwent both early as well as late apoptosis. The most important characteristic of apoptosis are the occurrence of morphological changes during the cell death. The viable cells exhibit green fluorescence
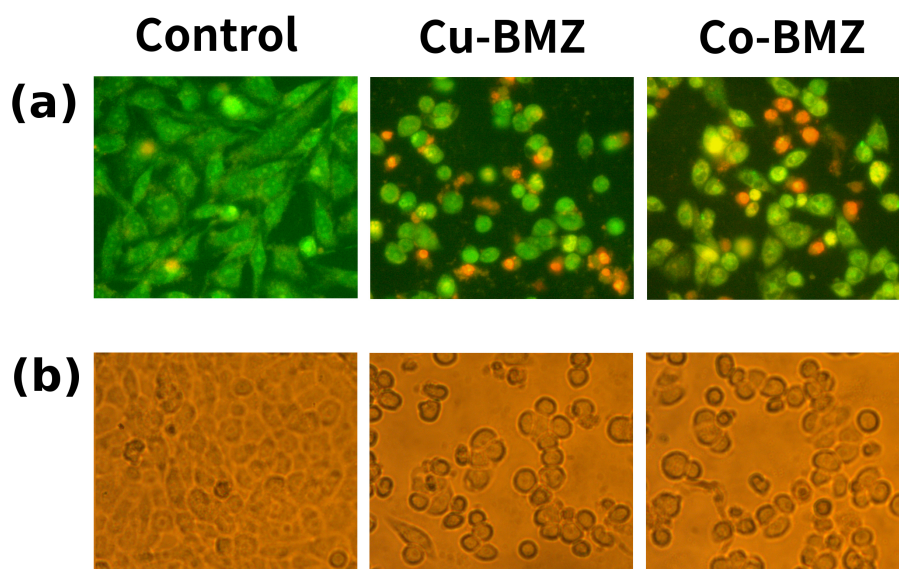
Fig. 7.10: (a) AO/EB: Control and, Cu-BMZ and Co-BMZ treated A549 cells irradiated with laser. Green colour cells are live cells and Red colour cells showing apoptotic morphology, (b) Light microscopic observation of Control, Cu-BMZ and Co-BMZ treated A549 cells irradiated with laser

with normal cell features like uniform chromatin with intact cell membrane, whereas, the early apoptotic cells exhibit bright green region with yellowish green nuclear fragmentation, membrane bubbling formation of apoptotic bodies outside and the late apoptosis cells exhibited orange-yellow or red nuclei with condensed or fragmented chromatin. The cell destruction can be attributed to the reactive oxygen species (ROS) as well as to the laser-induced ROS [153]. Often the anticancer activity of the metal complexes arose due to ROS and it can be attributed to the redox potentials of the

metal complexes [154]. The metal ions in the complexes tend to reduce the intercellular thiols like glutathione. Further reaction of reduced metal ions with molecular oxygen would generate the reactive superoxide radicals ($O_2^{\cdot-}$) which lead to the cell destruction [154, 155]. So, in the present case, proton reduction of metal ions (Co and Cu) in the complexes induces ROS assisted destruction in the A549 cell lines. Further, smaller particle size favours more material to enter into the cell. Due to this, Cu-BMZ nanoparticles (with much smaller size) induced more destruction in the cell line. But during the laser irradiation chances are high for microbubble formation, due to the heat stress generated by local thermal effects, than the laser-induced ROS [156]. So, in the present case, increment in cell destruction upon laser radiation can be attributed to the local thermal effects which was further contributed by the thermo-optical behavior of metal complexes in the operating wavelength.

7.4.4.3 Docking Analysis

In order to evaluate the binding mode of the synthesized ligands, docking analysis were performed using Autodock 4.2 [157]. Anaplastic Lymphoma Kinase (ALK) protein is chosen as the receptor for docking studies due to its potential anomaly in signaling cancer [158]. The simulations are validated by means of one-ligand run calculation using the original bound ligand 'crizotinib', which was extracted from the receptor. Since, the calculated root mean square deviation (RMSD) of scoring conformation falls under 1.6 , the method could be considered for the analysis of other compounds too. So, Co-BMZ and Cu-BMZ molecules were docked with ALK receptor using the same protocol used in the validation study. Docking studies for each molecule was performed for 2.5×10^6 energy evaluations and the docked conformations were analysed by means of bonding, energy and interaction between the ligand and ALK receptor. The poses are visualized by using PyMol and Chimera programs and the final coordinates of the ligand and receptor was saved in PDB format (Figure 7.11). The

Table 7.2: Docking scores and IC$_{50}$ values of Co-BMZ and Cu-BMZ complexes

	Co-BMZ	Cu-BMZ
Dock Score	-6.80	-7.24
IC$_{50}$ value	95	109

docking scores were used to calculate the free binding energy and are given in Table 7.2. The docking results can be correlated with the anticancer analysis. Cu-BMZ complex shows better binding energy with ALK receptor, than Co-BMZ complex. The results are in agreement with the observed experimental results and indicate that the Cu-BMZ molecule fit well with the binding site of ALK receptor. The Cu-BMZ interacts with amino acids of ALK receptor, namely: GLY1269, ASP1270, LEU1256, LEU1198, LEU1122, LEU1196, GLU1197, ALA1148, LYS1150, MET1199, ARG1253 and ASN1254. Whereas, the Co-BMZ complex interacts with amino acids of LEU1122, EU1196, ALA1148, LEU1196, MET1199, LEU1256, ARG1253, ASP1270 and ASN1254.
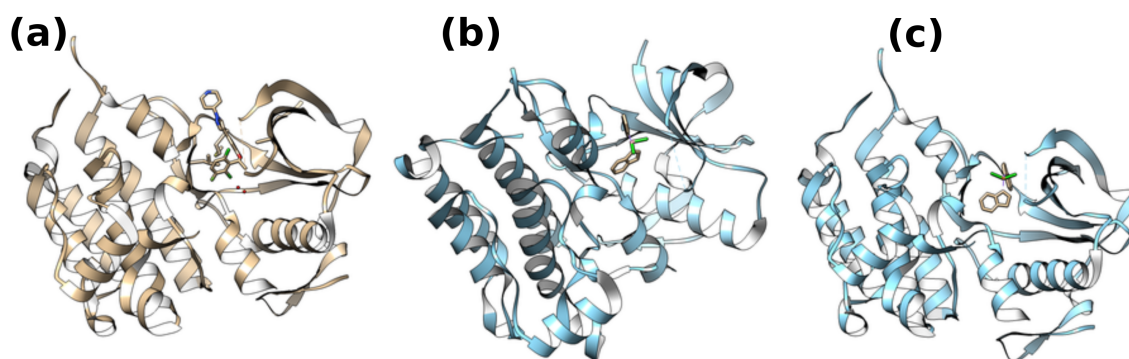
Fig. 7.11: Docking positions of (a) crizotinib (b) Co-BMZ and (c) Cu-BMZ molecules with ALK receptor

7.5   Conclusion

The prepared Co-BMZ and Cu-BMZ complex thin films and Co-BMZ-OAc and Cu-BMZ-OAc embedded PMMA free standing films are demonstrated to have optical limiting property. Further,inverted switching behavior is demonstrated in one of the fabri-

cated Mn-BMZ film and thermal assisted nonlinearity can be attributed to the switching effect in samples. The major advantage of this type of switches are their low linear absorption in the operation wavelength and low pumping power requirement. This ensures the compactness and cost effective in device fabrication. In the case of nanoparticles, PDT and docking studies reveal that the Cu-BMZ samples possess better anti-cancer activity than the Co-BMZ particles. The size and interaction energy of the Cu-BMZ particles can be accounted for their potential activity. Further, the irradiated cells exhibit higher toxicity than the treated cells, corresponding to the thermal effects due to the laser irradiation.

Summary and Future Directions

Nonlinear optical materials possesses potential applications in the area of photonics based devices. Both organic and inorganic materials are widely investigated to develop a potential NLO device. Comparing to inorganic materials, organic complexes posses better nonlinear optical susceptibilities. But their usage is limited due to their lower physical and chemical stability. It is suggested to develop combination of organic and inorganic materials to overcome the limitations of organic materials. So, metal-organic materials gain much interest in the recent past towards the development of potential NLO material. In this direction, the computational design, synthesis / thin film deposition and characterization of benzimidazole based metal organic complex for nonlinear optical applications are discussed in this thesis.

For the analysis, simple bis form of benzimidazole with first row transition metals have been used. The polarizability and hyperpolarizability values of benzimidazole metal complexes with and without substituents have been analysed using PM6 algorithm and TDHF formalism. From the ground state molecular properties such as energy gap value and heat of formation, ability of the molecule towards polarization by

an external field and its stability was studied. Different molecular descriptors were calculated using the semiempirical quantum chemical calculations. They were correlated by means of principle component analysis and the first principal component shows strong correlation between molecular energy (E) and linear poalrizability (ALP) and decreases with bond angle (BA), global hardness value (ETA) and heat of formation (HOF) values. Whereas, the second principal component dominated by only three parameters, in which bond length (BL) and intensity (INT) decreases whereas, molecular energy increases. These components provide a strong base to evaluate the nonlinear optical properties of the first row transition metal complexes. From the results of hyperpolarizability calculations, it is found that Co, Cu and Mn ions shows better values. Since they have better HOF values, they were chosen as candidates for the experimental analysis. In terms of HOF, Cl and OAc substituents shows a negative value, indicating that the complexes with those substituents are easy to synthesize. Experimentally it is hard to synthesize materials without substituents and hence, Cl and OAc based metal salts were used for the experimental analysis.

In the experimental analysis, modified liquid phase growth apparatus was used to deposit the benzimidazole and its metal complex thin films. The role of different deposition temperature on the thickness of benzimidazole thin films have been analysed. Further, physisorption process in the deposition of metal complex films also have been studied. Some metal acetate complexes of benzimidazole precipitate immediately. Therefore they are embedded into a PMMA matrix to cast as a polymeric free standing films. The thickness of all the samples was estimated using air wedge technique. For biological studies two of the complexes, Co and Cu based dichloride bis benzimidazole, were synthesized by using repreciptation technique.

Different characterization studies were employed to analyse the structural and surface morphology of the prepared samples. Considering crystallanity all the sam-

ples exhibit amorphous nature except BMZ thin films. Molecular structure of Co-BMZ, Cu-BMZ, Co-BMZ-OAc, Cu-BMZ-OAc and Mn-BMZ-OAc were studied by FT-IR analysis. Further, EDS, EPR and theoretical simulations were used to confirm the molecular structure of Mn-BMZ sample. Thin film samples were annealed at different temperatures and it is found that the surface topography varies with respect to the annealing temperature. The DLS and TEM analyses reveal the high stability of the nanoparticles with cubic and spheroid morphology.

The fabricated samples were subjected computational and linear absorption studies. All the samples show good absorption in UV-Vis. region corresponding to $\pi \to \pi^*$ transitions. Both the linear optical property and computational simulation indicates the potentiality of the complexes towards nonlinear optical applications.

The fabricated nanostructures were studied for SHG efficiency and third order susceptibility which are crucial from the applications point of view. The relative SHG efficiency of the prepared Co-BMZ and Cu-BMZ complex films is higher than that of parent BMZ ligand. Third order nonlinear susceptibility of both (Co-BMZ and Cu-BMZ) the samples are in the range of 10^{-6} esu and the films annealed at 150 °C acquire better FOM than the other as prepared and annealed samples. The third order nonlinear studies of Mn-BMZ thin films of ASP sample and the samples annealed at 100 °C and 150 °C show a self-defocussing effect (CA curves) and saturable absorption (OA curves) in the Z-Scan analysis. But the film annealed at 200 °C shows an switch over phenomena from SA to RSA in OA curves and defocussing to focusing in CA curves due to the variation in input intensity with respect to the surface defects. The calculated third order nonlinear susceptibility of the Mn-BMZ samples was ~ 1.64 to 3.93 $\times 10^{-9}$ esu and the films annealed at 150 °C showed better FOM than the as prepared and other annealed samples. The MBMZ embedded PMMA free standing films showed thermally induced self-focusing and reverse saturable effect in the third order nonlin-

ear optical studies of the samples. The third order susceptibility of the free standing films was in the order of 10^{-5} esu. The high figure of merit of the samples ensures the potentiality of the Co-BMZ-OAc and Cu-BMZ-OAc embedded PMMA films for optical limiting applications. In the case of nanoparticles nonlinear absorptive studies indicate that the particles have good saturable absorption at 650 nm region. The SA value increases with increase in laser power corresponds to the higher thermal effects.

Finally, the prepared Co-BMZ and Cu-BMZ complex thin films and Co-BMZ-OAc and Cu-BMZ-OAc embedded PMMA free standing films are demonstrated to have optical limiting property. Further, inverted switching behavior is demonstrated in one of the fabricated Mn-BMZ film and thermal assisted nonlinearity was attributed to the switching effect in samples. In the case of nanoparticles, PDT and docking studies reveal that the Cu-BMZ samples possess better anti-cancer activity than the Co-BMZ particles. The size and interaction energy of the Cu-BMZ particles can be accounted for their potential activity. Further, the irradiated cells exhibit higher toxicity than the treated cells, corresponding to the thermal effects due to the laser irradiation.

The possible future directions of the thesis is that the obtained semiempirical results can be revalidated using higher level theories. Further, by employing more sophisticated deposition strategies these complexes can be synthesized as metal organic frameworks, which is an emerging field with more potential applications. Also, considering third order nonlinear optical properties, thermo-optical assisted nonlinearity only discussed in the thesis. Further, the electronic polarizability of the samples can be studied using nano or femto second lasers. Also, the possibility of anticancer activity using benzimidazole metal complexes have been intimated in our studies. More computational and experimental strategies can be used to take it further.

Validation of PM6 & PM7 Semiempirical Methods

In the recent past many reports were tried to validate the prediction of molecular properties by semiempirical methods to other high level theories and the experimental results. This part describes the variation in accuracy of semiempirical polarizability calculations with respect to different molecular structures and solid clusters. All the calculations were carried out using MOPAC2012 package installed in a intel quad core processor system with Fedora 20 OS. Three types of molecules such as, small molecular systems, medium sized organic systems and simple nanoclusters were chosen for the investigation. In which, small systems such as CO, CO_2 and benzene are often considered as benchmarking systems and used to validate the computational results. Three medium sized organic fluorenyl molecular derivatives were studied to identify the structure dependent variation in the accuracy of results. Further, three solid ZnO nanoclusters of different point groups have also been studied to explore the point group dependent variation in the solid state semiempirical calculations. Structures of the molecules are either obtained as cif files or drawn using ChemDraw software. All the drawn molecular inputs were pre-optimized using Universal Force Filed (UFF) al-

gorithm embedded in Avogadro package and the cif files are directly converted into input files and used without pre-optimization process. Further the molecules were optimized using corresponding PM6 and PM7 methods with GNORM values about 0.01, 0.25 and 0.1 for small molecular systems, organic molecules and nanoclusters respectively. FORCE (vibrational analysis) calculations were carried out to validate the geometry and if any negative frequencies were obtained in the calculation, geometrical parameters have been changed and the molecule was re-optimized. For all the systems static polarizability and hyperpolarizability values were calculated at TDHF level. In the case of small molecular systems, the polarizability values of benzene obtained from PM6 and PM7 methods are slightly higher than that of the experimental values. In the case of second order hyperpolarizability calculations, the calculated semiempirical values were slightly lesser than that of the experimental values. In both the cases, the accuracy of PM6 and PM7 calculations are equal to the high level ab initio methods. The obtained results are given in the Tables. A.1 − A.3. The results of CO and CO_2 molecules are compared with the results of standard methods. i.e., for CO, CC3 results and for CO_2, MP2 results have been taken from the literature. In this case also semiempirical methods provide accurate results with that of the ab initio methods.

Table A.1: Polarizability and second hyperpolarizability values of benzene molecule in a.u.

Method	α	γ
MP2 CPHF	63.14	15868
MP2 TDHF	65.35	53290
MP2 FF	63.93	22967
B3LYP	66.53	21989
PM6	68.56	14614
PM7	68.83	15756
Exp	66.80	177550

In the case of organic molecular systems, three fluorenyl derivatives, 7-Nitro-9H-fluoren-2-ylamine (7N9HF2Y), 1-(7-Nitro-9H-fluoren-2-yl)-pyrrolidine (1-7N9HF-2YA) and [2-(7-Nitro-9H-fluoren-2-yl)-vinyl]-1-1'-dipyrrolidine (2-7N9HF-2YP) molecules (Figure. A.1)

Table A.2: Polarizability and second hyperpolarizability values of CO molecule in a.u.

Method	α	β
HF	12.53	8.58
CCSD	13.35	16.93
CC3	13.35	16.13
B3LYP	13.52	18.37
PM6	10.21	20.25
PM7	10.11	19.47

Table A.3: Polarizability and second hyperpolarizability values of CO_2 molecule in a.u.

Method	α	β
MP2	15.81	0.0045
CIS	18.11	–
TD-DFT	14.48	–
ZINDO-CI	12.12	–
PM6	18.54	0.0021
PM7	19.36	0.0045

have been considered for analysis. For the sake of comparison with reported values, only second order nonlinear susceptibility values of the fluorenyl derivatives were calculated. It is observed that the accuracy of the results increases with increase in asymmetry of the molecular structures. The obtained results are shown in Table A.4. In
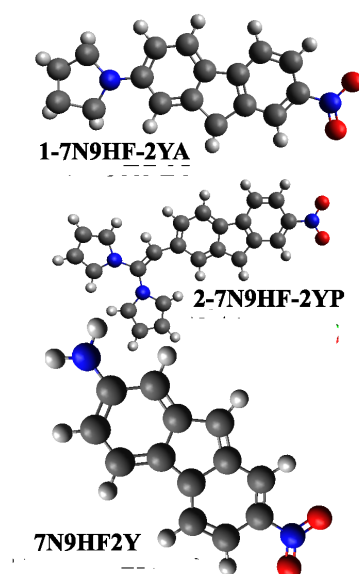
Fig. A.1: Molecular structure of fluorenyl derivatives

Table A.4: First hyperpolarizability values of fluorenyl derivatives

$\beta \times 10^{-34}$ (esu)	HF	PM6	PM7
7N9HF2Y	30.20	26.30	31.31
1-7N9HF-2YA	42.67	32.37	45.66
2-7N9HF-2YP	83.13	71.26	81.39

order to study the effect of point groups and molecular energies, three solid clusters ZnO with point groups D_{2h}, C_s, C_{2V} (Figure. A.2) with energies 0.00, 0.82 and 1.5 have been considered for the calculations, respectively. The calculated results are compared with B3LYP level reports. It is clear from the results that the point group of the systems greatly influences the accuracy of the results, i.e., more asymmetric the molecule, more accurate the results. The obtained results are given in Table A.5.

$(D_{2h}, 0.00)$ $(C_s, 0.82)$
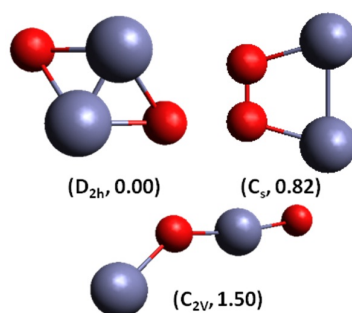
$(C_{2V}, 1.50)$

Fig. A.2: Molecular structures of ZnO nanoclusters

Table A.5: Polarizability and hyperpolarizability calculations of ZnO nanoclusters of different point groups in a.u.

Method	ZnO (D_2h,0.00)			ZnO (C_s, 0.82)			ZnO (C_{2v}, 1.50)		
	α	β	γ	α	β	γ	α	β	γ
B3LYP	62.67	0.1	2420	167.27	637	5660	85.6	608	4750
PM6	36.78	0.09	519.2	44.76	1091	4273	49.16	1161	7323
PM7	42.21	0.91	808.6	40.22	937	4332	41.35	823	9633

In summary, the calculations confirm the potentiality of PM6 and PM7 algorithms towards polarizability calculations and the results show the variation in accuracy with respect to symmetry.

Bibliography

[1] P. Franken, A. Hill, C. e. Peters, and G. Weinreich, "Generation of optical harmonics," *Physical Review Letters*, vol. 7, no. 4, p. 118, 1961.

[2] A. Liu, R. Jones, L. Liao, D. Samara-Rubio, D. Rubin, O. Cohen, R. Nicolaescu, and M. Paniccia, "A high-speed silicon optical modulator based on a metal–oxide–semiconductor capacitor," *Nature*, vol. 427, no. 6975, pp. 615–618, 2004.

[3] H. Nakamura, Y. Sugimoto, K. Kanamoto, N. Ikeda, Y. Tanaka, Y. Nakamura, S. Ohkouchi, Y. Watanabe, K. Inoue, H. Ishikawa, *et al.*, "Ultra-fast photonic crystal/quantum dot all-optical switch for future photonic networks," *Optics express*, vol. 12, no. 26, pp. 6606–6614, 2004.

[4] A. Van de Nes, J. Braat, and S. Pereira, "High-density optical data storage," *Reports on Progress in Physics*, vol. 69, no. 8, p. 2323, 2006.

[5] H. Pakarzadeh and S. Rezaei, "Modeling of dispersion and nonlinear characteristics of tapered photonic crystal fibers for applications in nonlinear optics," *Journal of Modern Optics*, vol. 63, no. 2, pp. 151–158, 2016.

[6] D. S. Chemla, *Nonlinear optical properties of organic molecules and crystals*, vol. 1. Elsevier, 2012.

[7] P. Norman and K. Ruud, "Microscopic theory of nonlinear optics," in *Non-Linear Optical Properties of Matter*, pp. 1–49, Springer, 2006.

[8] G. Zumofen, N. Mojarad, V. Sandoghdar, and M. Agio, "Perfect reflection of light by an oscillating dipole," *Physical Review Letters*, vol. 101, no. 18, p. 180404, 2008.

[9] R. W. Boyd, *Nonlinear optics*. Academic press, 2003.

[10] J. L. Bredas, C. Adant, P. Tackx, A. Persoons, and B. Pierce, "Third-order nonlinear optical response in organic materials: theoretical and experimental aspects," *Chemical Reviews*, vol. 94, no. 1, pp. 243–278, 1994.

[11] S. R. Marder, J. E. Sohn, and G. D. Stucky, "Materials for nonlinear optics chemical perspectives," tech. rep., DTIC Document, 1991.

[12] H. S. Nalwa, "Organic materials for third-order nonlinear optics," *Advanced Materials*, vol. 5, no. 5, pp. 341–358, 1993.

[13] S.-n. Zhu, Y.-y. Zhu, and N.-b. Ming, "Quasi-phase-matched third-harmonic generation in a quasi-periodic optical superlattice," *Science*, vol. 278, no. 5339, pp. 843–846, 1997.

[14] G. Kirchmair, B. Vlastakis, Z. Leghtas, S. E. Nigg, H. Paik, E. Ginossar, M. Mirrahimi, L. Frunzio, S. M. Girvin, and R. J. Schoelkopf, "Observation of quantum state collapse and revival due to the single-photon Kerr effect," *Nature*, vol. 495, no. 7440, pp. 205–209, 2013.

[15] D. McMorrow, W. T. Lotshaw, and G. A. Kenney-Wallace, "Femtosecond optical Kerr studies on the origin of the nonlinear responses in simple liquids," *Quantum Electronics*, vol. 24, no. 2, pp. 443–454, 1988.

[16] K. Isobe, H. Kawano, A. Suda, A. Kumagai, A. Miyawaki, and K. Midorikawa, "Simultaneous two-photon absorption and stimulated Raman scattering imaging by spatial overlap modulation microscopy," in *Lasers and Electro-Optics Europe (CLEO EUROPE/IQEC), 2013 Conference on and International Quantum Electronics Conference*, pp. 1–1, IEEE, 2013.

[17] R. Scott, A. W. Achtstein, A. Prudnikau, A. Antanovich, S. Christodoulou, I. Moreels, M. Artemyev, and U. Woggon, "Two photon absorption in II–VI semiconductors: The influence of dimensionality and size," *Nano Letters*, vol. 15, no. 8, pp. 4985–4992, 2015.

[18] Y. Gao, X. Zhang, Y. Li, H. Liu, Y. Wang, Q. Chang, W. Jiao, and Y. Song, "Saturable absorption and reverse saturable absorption in platinum nanoparticles," *Optics communications*, vol. 251, no. 4, pp. 429–433, 2005.

[19] W. Miniscalco, J. Pellegrino, and W. Yen, "Measurements of excited-state absorption in Ce3+: YAG," *Journal of Applied Physics*, vol. 49, no. 12, pp. 6109–6111, 1978.

[20] H. J. Kuhn and J. Robillard, *Nonlinear optical materials*. CRC press, 1991.

[21] R. G. Smith, "Theory of intracavity optical second-harmonic generation," *Quantum Electronics*, vol. 6, no. 4, pp. 215–223, 1970.

[22] M. Yamada and K. Kishima, "Fabrication of periodically reversed domain structure for SHG in LiNbO3, by direct electron beam lithography at room temperature," *Electronics Letters*, vol. 27, no. 10, pp. 828–829, 1991.

[23] J. D. Bierlein and H. Vanherzeele, "Potassium titanyl phosphate: properties and new applications," *Journal of Optical Society of America B*, vol. 6, no. 4, pp. 622–633, 1989.

[24] G. G. Gurzadyan, V. G. Dmitriev, and D. N. Nikogosyan, *Handbook of nonlinear optical crystals*. Springer-Verlag, 1991.

[25] G. Decher and J. B. Schlenoff, *Multilayer thin films: sequential assembly of nanocomposite materials*. John Wiley & Sons, 2006.

[26] P. Blanchard and G. Mitchell, "A comparison of photoinduced poling and thermal poling of azo-dye-doped polymer films for second order nonlinear optical applications," *Applied Physics Letters*, vol. 63, no. 15, pp. 2038–2040, 1993.

[27] D. Hall, M. A. Newhouse, N. F. Borrelli, W. H. Dumbaugh, and D. Weidman, "Nonlinear optical susceptibilities of high-index glasses," *Applied Physics Letters*, vol. 54, no. 14, pp. 1293–1295, 1989.

[28] S.-H. Kim, T. Yoko, and S. Sakka, "Linear and nonlinear optical properties of TeO2 glass," *Journal of the American Ceramic Society*, vol. 76, no. 10, pp. 2486–2490, 1993.

[29] S. S. Jha and N. Bloembergen, "Nonlinear optical susceptibilities in group-IV and III-V semiconductors," *Physical Review B*, vol. 171, no. 3, p. 891, 1968.

[30] H. Liao, R. Xiao, H. Wang, K. Wong, and G. Wong, "Large third-order optical nonlinearity in Au: TiO2 composite films measured on a femtosecond time scale," *Applied Physics Letters*, vol. 72, p. 1817, 1998.

[31] T. Verbiest, S. Houbrechts, M. Kauranen, K. Clays, and A. Persoons, "Second-order nonlinear optical materials: recent advances in chromophore design," *Journal of Materials Chemistry*, vol. 7, no. 11, pp. 2175–2189, 1997.

[32] O. R. Evans and W. Lin, "Crystal engineering of NLO materials based on metal-organic coordination networks," *Accounts of Chemical Research*, vol. 35, no. 7, pp. 511–522, 2002.

[33] G. De La Torre, P. Vazquez, F. Agullo-Lopez, and T. Torres, "Phthalocyanines and related compounds: organic targets for nonlinear optical applications," *Journal of Materials Chemistry*, vol. 8, no. 8, pp. 1671–1683, 1998.

[34] A. H. El-Masry, H. Fahmy, and S. Ali Abdelwahed, "Synthesis and antimicrobial activity of some new benzimidazole derivatives," *Molecules*, vol. 5, no. 12, pp. 1429–1438, 2000.

[35] R. Paramashivappa, P. P. Kumar, P. S. Rao, and A. S. Rao, "Design, synthesis and biological evaluation of benzimidazole/benzothiazole and benzoxazole derivatives as cyclooxygenase inhibitors," *Bioorganic & Medicinal Chemistry Letters*, vol. 13, no. 4, pp. 657–660, 2003.

[36] H. Barker, R. Smyth, H. Weissbach, J. Toohey, J. Ladd, and B. Volcani, "Isolation and properties of crystalline cobamide coenzymes containing benzimidazole or 5, 6-dimethylbenzimidazole," *Journal of Biological Chemistry*, vol. 235, no. 2, pp. 480–488, 1960.

[37] L. C. Davidse, "Benzimidazole fungicides: mechanism of action and biological impact," *Annual review of Phytopathology*, vol. 24, no. 1, pp. 43–65, 1986.

[38] F. Wang, W. B. Tan, Y. Zhang, X. Fan, and M. Wang, "Luminescent nanomaterials for biological labelling," *Nanotechnology*, vol. 17, no. 1, p. R1, 2005.

[39] K. Fylaktakidou, D. Hadjipavlou-Litina, K. Litinas, E. Varella, and D. Nicolaides, "Recent developments in the chemistry and in the biological applications of ami-doximes," *Current Pharmaceutical Design*, vol. 14, no. 10, pp. 1001–1047, 2008.

[40] A. W. White, R. Almassy, A. H. Calvert, N. J. Curtin, R. J. Griffin, Z. Hostomsky, K. Maegley, D. R. Newell, S. Srinivasan, and B. T. Golding, "Resistance-modifying agents: Synthesis and biological properties of benzimidazole inhibitors of the DNA repair enzyme Poly (ADP-ribose) Polymerase," *Journal of Medicinal Chemistry*, vol. 43, no. 22, pp. 4084–4097, 2000.

[41] R. M. Batista, S. P. Costa, M. Belsley, C. Lodeiro, and M. M. M. Raposo, "Synthesis and characterization of novel (oligo) thienyl-imidazo-phenanthrolines as versatile π-conjugated systems for several optical applications," *Tetrahedron*, vol. 64, no. 39, pp. 9230–9238, 2008.

[42] M.-Y. Lai, C.-H. Chen, W.-S. Huang, J. T. Lin, T.-H. Ke, L.-Y. Chen, M.-H. Tsai, and C.-C. Wu, "Benzimidazole/amine-based compounds capable of ambipolar transport for application in single-layer blue-emitting OLEDs and as hosts for phosphorescent emitters," *Angewandte Chemie*, vol. 47, no. 3, pp. 581–585, 2008.

[43] Y. Wei, Y. Yu, R. Sa, Q. Li, and K. Wu, "Two cobalt (II) coordination polymers [Co$_2$ (H$_2$ O)$_4$ (Hbidc)$_2$] n and [Co (Hbidc)] n (Hbidc= 1 H-benzimidazole-5, 6-dicarboxylate): syntheses, crystal structures, and magnetic properties," *CrystEngComm*, vol. 11, no. 6, pp. 1054–1060, 2009.

[44] J.-H. Yum, D. P. Hagberg, S.-J. Moon, K. M. Karlsson, T. Marinado, L. Sun, A. Hagfeldt, M. K. Nazeeruddin, and M. Grätzel, "A light-resistant organic sensitizer for solar-cell applications," *Angewandte Chemie*, vol. 121, no. 9, pp. 1604–1608, 2009.

[45] N. Vijayan, R. Ramesh Babu, R. Gopalakrishnan, P. Ramasamy, and W. Harrison, "Growth and characterization of benzimidazole single crystals: a nonlinear optical material," *Journal of Crystal Growth*, vol. 262, no. 1, pp. 490–498, 2004.

[46] N. Vijayan, G. Bhagavannarayana, T. Kanagasekaran, R. R. Babu, R. Gopalakrishnan, and P. Ramasamy, "Crystallization of benzimidazole by solution growth method and its characterization," *Crystal Research and Technology*, vol. 41, no. 8, pp. 784–789, 2006.

[47] N. A. Mazlan, T. B. S. Ravoof, E. R. Tiekink, M. I. M. Tahir, A. Veerakumarasivam, and K. A. Crouse, "Mixed-ligand metal complexes containing an ONS Schiff base and imidazole/benzimidazole ligands: synthesis, characterization, crystallography and biological activity," *Transition Metal Chemistry*, vol. 39, no. 6, pp. 633–639, 2014.

[48] D. Peng, W. Zhang, G. Tang, J. Zhou, J. Hu, Q. Xie, and C. Zhong, "Novel dye sensitizers of main chain polymeric metal complexes based on complexes of 2-(2□-pyridyl) benzimidazole derivative with Zn (II), Co (II): synthesis, characterization, and photovoltaic performance for dye-sensitized solar cells," *Journal of the Iranian Chemical Society*, vol. 12, no. 3, pp. 397–404, 2015.

[49] R. Visbal and M. C. Gimeno, "N-heterocyclic carbene metal complexes: photoluminescence and applications," *Chemical Society Reviews*, vol. 43, no. 10, pp. 3551–3574, 2014.

[50] G. S. Yellol, A. Donaire, J. G. Yellol, V. Vasylyeva, C. Janiak, and J. Ruiz, "On the antitumor properties of novel cyclometalated benzimidazole Ru (II), Ir (III) and Rh (III) complexes," *Chemical Communications*, vol. 49, no. 98, pp. 11533–11535, 2013.

[51] J. Stewart, "MOPAC 2012, Colorado springs, CO: Stewart Computational Chemistry, USA," 2014.

[52] K. Todoroki, T. Nakano, H. Watanabe, J. Z. Min, K. Inoue, Y. Ishikawa, and T. TOYO'OKA, "Computational prediction of diastereomeric separation behavior of fluorescent o-phthalaldehyde derivatives of amino acids," *Analytical Sciences*, vol. 30, no. 9, pp. 865–870, 2014.

[53] E. F. Durán-Lara, X. A. López-Cortés, R. I. Castro, F. Avila-Salas, F. D. González-Nilo, V. F. Laurie, and L. S. Santos, "Experimental and theoretical binding affinity between polyvinylpolypyrrolidone and selected phenolic compounds from food matrices," *Food chemistry*, vol. 168, pp. 464–470, 2015.

[54] R. Visbal and M. C. Gimeno, "N-heterocyclic carbene metal complexes: photoluminescence and applications," *Chemical Society Reviews*, vol. 43, no. 10, pp. 3551–3574, 2014.

[55] E. Baranoff, "First-row transition metal complexes for the conversion of light into electricity and electricity into light," in *Organometallics and Related Molecules for Energy Conversion*, pp. 61–90, Springer, 2015.

[56] M. U. Rehman, M. Arif, M. Imran, and M. Farooq, "Synthesis, characterization and antimicrobial properties of mannich base cyclization derivatives of benzimidazole and their metal complexes," *American Journal of Chemistry*, vol. 4, no. 1, pp. 10–21, 2014.

[57] M. Goodgame and F. Cotton, "Preparation and magnetic and spectral studies of some cobalt (II) complexes of benzimidazole," *Journal of the American Chemical Society*, vol. 84, no. 9, pp. 1543–1548, 1962.

[58] G. S. Yellol, J. G. Yellol, V. B. Kenche, X. M. Liu, K. J. Barnham, A. Donaire, C. Janiak, and J. Ruiz, "Synthesis of 2-pyridyl-benzimidazole Iridium (III), Ruthenium (II), and Platinum (II) complexes. Study of the activity as inhibitors of amyloid-β aggregation and neurotoxicity evaluation," *Inorganic chemistry*, vol. 54, no. 2, pp. 470–475, 2014.

[59] A. Chaturvedi, Y. Mishra, and V. Rajawat, "Synthesis of pyrimidine 2-ol/thiol derivatives of benzimidazole as a ligand and their Bi (III) metal complexes by conventional as well as microwave technique," *American Journal of Phytomedicine and Clinical Therapeutics*, vol. 3, no. 4, pp. 383–393, 2015.

[60] A.-R. Allouche, "Gabedit – A graphical user interface for computational chemistry softwares," *Journal of Computational Chemistry*, vol. 32, no. 1, pp. 174–182, 2011.

[61] G. Schaftenaar and J. H. Noordik, "Molden: a pre-and post-processing program for molecular and electronic structures," *Journal of Computer-Aided Molecular Design*, vol. 14, no. 2, pp. 123–134, 2000.

[62] E. Eliav, S. Fritzsche, and U. Kaldor, "Electronic structure theory of the super-heavy elements," *Nuclear Physics A*, 2015.

[63] H. A. Bent, "An appraisal of valence-bond structures and hybridization in compounds of the first-row elements.," *Chemical Reviews*, vol. 61, no. 3, pp. 275–311, 1961.

[64] J.-L. Brédas, "Relationship between band gap and bond length alternation in organic conjugated polymers," *The Journal of Chemical Physics*, vol. 82, no. 8, pp. 3808–3811, 1985.

[65] L. M. Rodriguez-Valdez, A. Martínez-Villafañe, and D. Glossman-Mitnik, "Computational simulation of the molecular structure and properties of heterocyclic organic compounds with possible corrosion inhibition properties," *Journal of Molecular Structure: Theoretical Chemistry*, vol. 713, no. 1, pp. 65–70, 2005.

[66] M. Rumi and G. Zerbi, "Conformational dependence of vibrational and molecular nonlinear optical properties in substituted benzenes: the role of π-electron conjugation and back-donation," *Journal of Molecular Structure*, vol. 509, no. 1, pp. 11–28, 1999.

[67] S. Choi and T. G. Spiro, "Out-of-plane deformation modes in the resonance Raman spectra of metalloporphyrins and heme proteins," *Journal of the American Chemical Society*, vol. 105, no. 11, pp. 3683–3692, 1983.

[68] R. Bro and A. K. Smilde, "Principal component analysis," *Analytical Methods*, vol. 6, no. 9, pp. 2812–2831, 2014.

[69] I. Algül and D. Kara, "Determination and chemometric evaluation of total aflatoxin, aflatoxin B1, ochratoxin A and heavy metals content in corn flours from Turkey," *Food chemistry*, vol. 157, pp. 70–76, 2014.

[70] C. Chapman and E. M. Feit, "Reducing data complexity," in *R for Marketing Research and Analytics*, pp. 195–223, Springer, 2015.

[71] Ş. Yurdakul and M. Kurt, "Vibrational spectroscopic studies of metal (II) halide benzimidazole," *Journal of Molecular Structure*, vol. 650, no. 1, pp. 181–190, 2003.

[72] E. Şahin, S. Ide, M. Kurt, and Ş. Yurdakul, "Structural investigation of dibromobis (benzimidazole) Zn (II) complex," *Journal of Molecular Structure*, vol. 616, no. 1, pp. 259–264, 2002.

[73] E. Sahin, S. Ide, M. Kurt, and S. Yurdakul, "Structural investigation of dichlorobis (benzimidazole) Zn (II) complex," *Journal of Molecular Structure*, vol. 728, no. 6, pp. 762–764, 2003.

[74] H. Chang, M. Fu, X.-J. Zhao, and E.-C. Yang, "Four benzimidazole-based Zn (II)/Cd (II) polymers extended by aromatic polycarboxylate coligands: Synthesis, structure, and luminescence," *Journal of Coordination Chemistry*, vol. 63, no. 20, pp. 3551–3564, 2010.

[75] Y.-m. Yu, B.-b. Suo, H.-h. Feng, H. Fan, and W.-M. Liu, "Electric dipole and quadrupole properties of In and Sr using finite field calculation," *arXiv preprint arXiv:1501.04439*, 2015.

[76] J. Kobus, "Hartree-Fock limit values of multipole moments, polarizabilities, and hyperpolarizabilities for atoms and diatomic molecules," *Physical Review A*, vol. 91, no. 2, p. 022501, 2015.

[77] M. Thakur and S. Meyler, "Growth of large-area thin-film single crystals of poly (diacetylenes)," *Macromolecules*, vol. 18, no. 11, p. 2341, 1985.

[78] T. Yamao, T. Miki, H. Akagami, Y. Nishimoto, S. Ota, and S. Hotta, "Direct formation of thin single crystals of organic semiconductors onto a substrate," *Chemistry of Materials*, vol. 19, p. 3748, 2007.

[79] G. Shugar and J. Ballinger, *Chemical Technicians Ready Reference Handbook*. New York: McGraw Hill, 1996.

[80] K. L. Chopra, *Thin film phenomena*, vol. 137. McGraw-Hill New York, 1969.

[81] P. A. Praveen, R. Ramesh Babu, S. P. Prabhakaran, and K. Ramamurthi, "Linear and nonlinear optical properties of Mn doped benzimidazole thin films," *AIP Conference Proceedings*, vol. 1591, p. 991, 2014.

[82] F. Tyler, *A Laboratory Manual of Physics*. London: Edward Arnold Limited, 4th ed., 1974.

[83] M. Ohring, *Materials Science of Thin films*. Academic press, 2001.

[84] A. K. Gupta and M. Gupta, "Synthesis and surface engineering of iron oxide nanoparticles for biomedical applications," *Biomaterials*, vol. 26, no. 18, pp. 3995–4021, 2005.

[85] A. Mendez-Vilas and J. Diaz, eds., *Modern Research and Educational Topics in Microscopy*, vol. 2. FORMATEX, 2007.

[86] N. Vijayan, R. Ramesh Babu, R. Gopalakrishnan, P. Ramasamy, and W. Harrison, "Growth and characterization of benzimidazole single crystals: a nonlinear optical material," *Journal of Crystal Growth*, vol. 262, p. 490, 2004.

[87] N. Vijayan, G. Bhagavannarayana, G. Budakoti, B. Kumar, V. Upadhyaya, and S. Das, "Optical, dielectric and surface studies on solution grown benzimidazole single crystals," *Materials Letters*, vol. 62, p. 1252, 2008.

[88] K. S. Lokovic, R. B. Bergmann, and A. Bill, "The grain size distribution in crystallization processes with anisotropic growth rate," *Materials Research Socity Symposium Proceedings*, vol. 1245, pp. 1245–A16–07, 2010.

[89] P. F. Fewster, "X-ray analysis of thin films and multilayers," *Reports on Progress in Physics*, vol. 59, p. 1339, 1996.

[90] S. Yurdakul and M. Kurt, "Vibrational spectroscopic studies of metal (ii) halide benzimidazole," *Journal of Molecular Structure*, vol. 650, pp. 181–190, 2003.

[91] F.-J. Yoe-Reyes, S. Bernes, and N. Barba-Behrens, "Dichlorobis (1H-benzimidazole-κn3) cobalt (II)," *Acta Crystallographica Section E: Structure Reports Online*, vol. 61, no. 5, pp. m875–m877, 2005.

[92] W.-H. Sun, C. Shao, Y. Chen, H. Hu, R. A. Sheldon, H. Wang, X. Leng, and X. Jin, "Controllable supramolecular assembly by π-π interactions: Cobalt (II) and copper (II) complexes with benzimidazole derivatives," *Organometallics*, vol. 21, pp. 4350–4355, 2002.

[93] N. Sireci, U. Yilmaz, H. Kucukbay, M. Akkurt, Z. Baktir, S. Turktekin, and O. Buyukgungor *Journal of Coordination Chemistry*, vol. 64, pp. 1894–1902, 2011.

[94] H. Lopez-Sandoval, M. E. London-Lemos, R. Garza-Velasco, I. Poblano-Melendez, P. Granada-Macias, I. Gracia-Mora, and N. Barba-Behrens, "Synthesis, structure and biological activities of cobalt (II) and zinc (II) coordination compounds with 2-benzimidazole derivatives," *Journal of Inorganic Biochemistry*, vol. 102, pp. 1267–1276, 2008.

[95] J. R. Ferrer, P. M. Lahti, C. George, P. Oliete, M. Julier, and F. Palacio, "Role of hydrogen bonds in benzimidazole-based organic magnetic materials: Crystal scaffolding or exchange linkers?," *Chemistry of materials*, vol. 13, no. 7, pp. 2447–2454, 2001.

[96] D. H. Brown, R. N. Nuttall, and D. W. A. Sharp, "The thermal decomposition of metal complexes–II: The decomposition of some bisquinoline metal (II) halides," *Journal of Inorganic and Nuclear Chemistry*, vol. 26, pp. 1151–1156, 1964.

[97] H. Martinez, P. Azavant, and M. Loudet, "Interpretation of scanning tunneling microscopy and atomic force microscopy images of 1T-TiS2," *Surface Science*, vol. 400, pp. 247–257, 1998.

[98] D. Guo, S. Ikeda, and K. Saiki, "Effect of annealing on the mobility and morphology of thermally activated pentacene thin film transistors," *Journal of Applied Physics*, vol. 99, p. 094502, 2006.

[99] L. H. Dubois and R. G. Nuzzo, "Synthesis, structure, and properties of model organic surfaces," *Annual Review of Physical Chemistry*, vol. 43, pp. 437–463, 1992.

[100] E. Şahin, S. Ide, M. Kurt, and Ş. Yurdakul, "Structural investigation of dibromobis (benzimidazole) Zn (II) complex," *Journal of Molecular Structure*, vol. 616, no. 1, pp. 259–264, 2002.

[101] Ş. Yurdakul and M. Kurt, "Vibrational spectroscopic studies of metal (II) halide benzimidazole," *Journal of Molecular Structure*, vol. 650, no. 1, pp. 181–190, 2003.

[102] H. Chang, M. Fu, X.-J. Zhao, and E.-C. Yang, "Four benzimidazole-based Zn (II) / Cd (II) polymers extended by aromatic polycarboxylate coligands: synthesis, structure, and luminescence," *Journal of Coordination Chemistry*, vol. 63, no. 20, pp. 3551–3564, 2010.

[103] K. Singh, M. S. Barwa, and P. Tyagi, "Synthesis and characterization of cobalt (II), nickel (II), copper (II) and zinc (II) complexes with schiff base derived from 4-amino-3-mercapto-6-methyl-5-oxo-1, 2, 4-triazine," *European Journal of Medicinal Chemistry*, vol. 42, no. 3, pp. 394–402, 2007.

[104] U. P. Chaudhuri, R. Shakya, J. M. McClain, E. L. Klein, D. R. Powell, A. Grohmann, and R. P. Houser, "Copper (II), iron (II), and manganese (II) complexes of 2-methyl-2-(2-pyridinyl)-1, 3-propanediamine," *Polyhedron*, vol. 54, pp. 84–90, 2013.

[105] S. Belaid, A. Landreau, S. Djebbar, O. Benali-Baitich, G. Bouet, and J.-P. Bouchara, "Synthesis, characterization and antifungal activity of a series of manganese (II) and copper (II) complexes with ligands derived from reduced N, N⎕-O-phenylenebis (salicylideneimine)," *Journal of Inorganic Biochemistry.*, vol. 102, no. 1, pp. 63–69, 2008.

[106] Z. A. Fekete, E. A. Hoffmann, T. Körtvélyesi, and B. Penke, "Harmonic vibrational frequency scaling factors for the new NDDO Hamiltonians: RM1 and PM6," *Molecular Physics*, vol. 105, no. 19-22, pp. 2597–2605, 2007.

[107] M. C. Goh, D. Juhue, O. M. Leung, Y. Wang, and M. A. Winnik, "Annealing effects on the surface structure of latex films studied by atomic force microscopy," *Langmuir*, vol. 9, no. 5, pp. 1319–1322, 1993.

[108] M. Makowska-Janusik and J. Benard, "Determination of the macroscopic optical properties for composite materials," *Journal of Physics: Conference Series*, vol. 79, no. 1, p. 012030, 2007.

[109] P. A. Praveen, R. Ramesh Babu, and K. Ramamurthi, "Validation of PM6 & PM7 semiempirical methods on polarizability calculations," *AIP Conference Proceedings*, vol. 1665, no. 1, p. 090011, 2015.

[110] A. Kinal and S. Sayhan, "Accurate prediction of hydrogen storage capacity of small boron nitride nanocages by dispersion corrected semi-empirical PM6-DH2 method," *International Journal of Hydrogen Energy*, vol. 41, no. 1, pp. 392–400, 2016.

[111] P. Csizmadia, "MarvinSketch and MarvinView: molecule applets for the world wide web," *Proceedings of ECSOC-3, The Third International Electronic Conference on Synthetic Organic Chemistry*, vol. 1, pp. 367–369, 1999.

[112] M. D. Hanwell, D. E. Curtis, D. C. Lonie, T. Vandermeersch, E. Zurek, and G. R. Hutchison, "Avogadro: an advanced semantic chemical editor, visualization, and analysis platform," *Journal of Cheminformatics*, vol. 4, no. 1, p. 17, 2012.

[113] J. J. Stewart, "Optimization of parameters for semiempirical methods IV: extension of MNDO, AM1, and PM3 to more main group elements," *Journal of Molecular Modeling*, vol. 10, no. 2, pp. 155–164, 2004.

[114] G. Schaftenaar and J. H. Noordik, "Molden: a pre-and post-processing program for molecular and electronic structures," *Journal of Computer-Aided Molecular Design*, vol. 14, no. 2, pp. 123–134, 2000.

[115] H. S. Muddana and M. K. Gilson, "Calculation of host–guest binding affinities using a quantum-mechanical energy model," *Journal of Chemical Theory and Computation*, vol. 8, no. 6, pp. 2023–2033, 2012.

[116] L. S. Sidhu, A. Halder, and S. Rai, "Dopant induced modulation in the structure and electronic properties of $Au_{1}0$ cluster," *RSC Advances*, vol. 6, no. 90, pp. 87115–87123, 2016.

[117] E.-S. Kang, T.-H. Lee, and B.-S. Bae, "Measurement of the thermo-optic coefficients in sol-gel derived inorganic–organic hybrid material films," *Applied Physics Letters*, vol. 81, no. 8, pp. 1438–1440, 2002.

[118] X. Li, Z. Cao, Q. Shen, and Y. Yang, "Influence of dopant concentration on thermo-optic properties of PMMA composite," *Materials Letters*, vol. 60, no. 9, pp. 1238–1241, 2006.

[119] J. Lim, S. P. Yeap, H. X. Che, and S. C. Low, "Characterization of magnetic nanoparticle by dynamic light scattering," *Nanoscale Research Letters*, vol. 8, p. 381, 2013.

[120] D. Li, M. B. Müller, S. Gilje, R. B. Kaner, and G. G. Wallace, "Processable aqueous dispersions of graphene nanosheets," *Nature nanotechnology*, vol. 3, no. 2, pp. 101–105, 2008.

[121] G. de la Torre, P. Vazquez, F. Agullo-Lopez, and T. Torres, "Role of structural factors in the nonlinear optical properties of phthalocyanines and related compounds," *Chemical Reviews*, vol. 104, pp. 3723–3750, 2004.

[122] J. M. Zadrozny, J. Telser, and J. R. Long, "Slow magnetic relaxation in the tetrahedral cobalt (II) complexes [Co (EPh) 4] 2-(E O, S, Se)," *Polyhedron*, vol. 64, pp. 209–217, 2013.

[123] T. Rosu, E. Pahontu, C. Maxim, R. Georgescu, N. Stanica, and A. Gulea, "Some new Cu (II) complexes containing an ON donor schiff base: synthesis, characterization and antibacterial activity," *Polyhedron*, vol. 30, no. 1, pp. 154–162, 2011.

[124] A. Farag and I. Yahia, "Structural, absorption and optical dispersion characteristics of rhodamine B thin films prepared by drop casting technique," *Optics Communications*, vol. 283, no. 21, pp. 4310–4317, 2010.

[125] Y.-Q. Hou, D.-M. Zhuang, G. Zhang, M. Zhao, and M.-S. Wu, "Influence of annealing temperature on the properties of titanium oxide thin film," *Applied Surface Science*, vol. 218, no. 1-4, pp. 98–106, 2003.

[126] P. A. Praveen, S. Prabhakaran, R. Ramesh Babu, K. Sethuraman, and K. Rama-murthi, "Low power optical limiting studies on nanocrystalline benzimidazole thin films prepared by modified liquid phase growth technique," *Bulletin of Materials Science*, vol. 38, no. 3, pp. 645–651, 2015.

[127] V. I. Minkin, *Dipole moments in organic chemistry*. Springer Science & Business Media, 2012.

[128] J. M. Zadrozny, J. Telser, and J. R. Long, "Slow magnetic relaxation in the tetra-hedral cobalt (II) complexes [Co (EPh) 4] 2-(E O, S, Se)," *Polyhedron*, vol. 64, pp. 209–217, 2013.

[129] M. A. Hitchman, "Electronic structure of low-spin cobalt(II) Schiff base com-plexes," *Inorganic Chemistry*, vol. 16, no. 8, pp. 1985–1993, 1977.

[130] F. Chen, J. Goodfellow, S. Liu, I. Grinberg, M. C. Hoffmann, A. R. Damodaran, Y. Zhu, P. Zalden, X. Zhang, I. Takeuchi, *et al.*, "Ultrafast terahertz gating of the polarization and giant nonlinear optical response in BiFeO3 thin films," *Advanced Materials*, vol. 27, no. 41, pp. 6371–6375, 2015.

[131] P. C. Ray, "Size and shape dependent second order nonlinear optical proper-ties of nanomaterials and their application in biological and chemical sensing," *Chemical Reviews*, vol. 110, no. 9, pp. 5332–5365, 2010.

[132] H. Manaa, A. Al Mulla, S. Makhseed, M. Al-sawah, and J. Samuel, "Fluorescence and nonlinear optical properties of non-aggregating hexadeca-substituted ph-thalocyanine," *Optical Materials.*, vol. 32, no. 1, pp. 108–114, 2009.

[133] V. Krishnakumar, G. Shanmugam, and R. Nagalakshmi, "Large third-order optical nonlinearity of Mg-doped PbS/PVA freestanding nanocomposite films," *Journal of Physics D: Applied Physics*, vol. 45, p. 165102, 2012.

[134] S. Zafar, Z. H. Khan, and M. S. Khan, "Study of self-defocusing, reverse saturable absorption and photoluminescence in anthraquinone PMMA nanocomposite film," *Spectrochimica Acta Part A: Molecular and Biomolecular Spectroscopy*, vol. 118, pp. 852–856, 2014.

[135] T. Godin, R. Moncorgé, J.-L. Doualan, M. Fromager, K. Ait-Ameur, R. A. Cruz, and T. Catunda, "Optically pump-induced athermal and nonresonant refractive in-dex changes in the reference Cr-doped laser materials: Cr: GSGG and ruby," *Journal of the Optical Society of America B*, vol. 29, no. 5, pp. 1055–1064, 2012.

[136] P. A. Praveen, R. Ramesh Babu, K. Jothivenkatachalam, and K. Ramamurthi, "Spectral, morphological, linear and nonlinear optical properties of nanostruc-tured benzimidazole metal complex thin films," *Spectrochimica Acta Part A: Molecular and Biomolecular Spectroscopy.*, vol. 150, pp. 280–289, 2015.

[137] S. Mathews, S. C. Kumar, L. Giribabu, and S. V. Rao, "Nonlinear optical and op-tical limiting properties of phthalocyanines in solution and thin films of PMMA at 633 nm studied using a cw laser," *Materials Letters*, vol. 61, pp. 4426–4431, 2007.

[138] X. Tong, H. Zhang, and D. Li, "Effect of annealing treatment on mechanical properties of nanocrystalline α-iron: an atomistic study," *Scientific reports*, vol. 5, 2015.

[139] W. Auwärter, D. Écija, F. Klappenberger, and J. V. Barth, "Porphyrins at interfaces," *Nature Chemistry*, vol. 7, no. 2, pp. 105–120, 2015.

[140] A. Maxwell, A. Unwin, I. Ward, M. A. El Maaty, M. Shahin, R. Olley, and D. Bassett, "The effect of molecular weight on the deformation behaviour of pressure annealed polyethylene," *Journal of Materials Science*, vol. 32, no. 3, pp. 567–574, 1997.

[141] A. Zawadzka, P. Płóciennik, J. Strzelecki, A. Korcala, A. Arof, and B. Sahraoui, "Impact of annealing process on stacking orientations and second order nonlinear optical properties of metallophthalocyanine thin films and nanostructures," *Dyes and Pigments*, vol. 101, pp. 212 – 220, 2014.

[142] G. Sreekumar, P. G. L. Frobel, C. I. Muneera, K. Sathiyamoorthy, C. Vijayan, and C. Mukherjee, "Saturable and reverse saturable absorption and nonlinear refraction in nanoclustered amido black dye–polymer films under low power continuous wave He–Ne laser light excitation," *Journal of Optics A: Pure and Applied Optics*, vol. 11, no. 12, p. 125204, 2009.

[143] C. Dai-Jian, D. Sha, H. Jun-Bo, Z. Hui-Jun, X. Si, X. Gui-Guang, and W. Qu-Quan, "A sign alternation of nonlinear absorption in gold composite films in z-scan," *Chinese Physics Letters*, vol. 22, no. 9, p. 2286, 2005.

[144] T. H. Jamieson, "Thermal effects in optical systems," *Optical Engineering*, vol. 20, no. 2, pp. 156–160, 1981.

[145] C. Schmidt, A. Chipouline, T. Pertsch, A. Tünnermann, O. Egorov, F. Lederer, and L. Deych, "Nonlinear thermal effects in optical microspheres at different wavelength sweeping speeds," *Optical Express*, vol. 16, no. 9, pp. 6285–6301, 2008.

[146] S. Hirata, K. Totani, T. Yamashita, C. Adachi, and M. Vacha, "Large reverse saturable absorption under weak continuous incoherent light," *Nature materials*, vol. 13, no. 10, pp. 938–946, 2014.

[147] K. Sendhil, C. Vijayan, and M. Kothiyal, "Low-threshold optical power limiting of cw laser illumination based on nonlinear refraction in zinc tetraphenyl porphyrin," *Optics & Laser Technology*, vol. 38, no. 7, pp. 512–515, 2006.

[148] P. Innocenzi and B. Lebeau, "Organic–inorganic hybrid materials for non-linear optics," *Journal of Materials Chemistry*, vol. 15, p. 3821, 2005.

[149] P. Sharma and S. Roy, "Effect of probe beam intensity on all-optical switching based on excited-state absorption," *Optical Materials Express*, vol. 2, no. 5, pp. 548–565, 2012.

[150] T. Mosmann, "Rapid colorimetric assay for cellular growth and survival: application to proliferation and cytotoxicity assays," *Journal of immunological methods*, vol. 65, no. 1, pp. 55–63, 1983.

[151] D. Spector, R. Goldman, and L. Leinwand, *Culture and Biochemical Analysis of Cells. Vol. 1: A Laboratory Manual.* Cold Spring Harbor Laboratory Press, Cold Spring Harbor, NY, 1998.

[152] D. Wirtz, K. Konstantopoulos, and P. C. Searson, "The physics of cancer: the role of physical interactions and mechanical forces in metastasis," *Nature Reviews Cancer*, vol. 11, no. 7, pp. 512–522, 2011.

[153] J. Yoon, S.-w. Ryu, S. Lee, and C. Choi, "Cytosolic irradiation of femtosecond laser induces mitochondria-dependent apoptosis-like cell death via intrinsic reactive oxygen cascades," *Scientific reports*, vol. 5, p. 8231, 2015.

[154] A. Sirbu, O. Palamarciuc, M. V. Babak, and J. M. Lim, "Copper (II) thiosemicarbazone complexes induce marked ros accumulation and promote NRF2-mediated antioxidant response in highly resistant breast cancer cells," *Dalton Transactions*, vol. 46, no. 12, pp. 3833–3847, 2017.

[155] J. Wang, C. Li, Q. Zhou, W. Wang, Y. Hou, B. Zhang, and X. Wang, "A polypyridyl Co (II) complex-based water reduction catalyst with double H 2 evolution sites," *Catalysis Science & Technology*, vol. 6, no. 24, pp. 8482–8489, 2016.

[156] V. P. Pattani, J. Shah, A. Atalis, A. Sharma, and J. W. Tunnell, "Role of apoptosis and necrosis in cell death induced by nanoparticle-mediated photothermal therapy," *Journal of Nanoparticle Research*, vol. 17, no. 1, p. 20, 2015.

[157] "Autodock 4.2 - docking software." `http://autodock.scripps.edu/resources/references`. Accessed: 2017-03-07.

[158] T. H. Marsilje, W. Pei, B. Chen, W. Lu, and Uno, "Synthesis, structure–activity relationships, and in vivo efficacy of the novel potent and selective anaplastic lymphoma kinase (ALK) inhibitor 5-Chloro-N 2-(2-isopropoxy-5-methyl-4-(piperidin-4-yl) phenyl)-N 4-(2-(isopropylsulfonyl) phenyl) pyrimidine-2, 4-diamine (LDK378) currently in phase 1 and phase 2 clinical trials," *Journal of Medicinal Chemistry*, vol. 56, no. 14, pp. 5675–5690, 2013.